

# COMET Phase-I technical design report

## The COMET Collaboration

R. Abramishvili<sup>10</sup>, G. Adamov<sup>10,16</sup>, R. R. Akhmetshin<sup>3,29</sup>, A. Allin<sup>22</sup>, J. C. Angélique<sup>4</sup>, V. Anishchik<sup>1</sup>, M. Aoki<sup>30</sup>, D. Aznabayev<sup>14</sup>, I. Bagaturia<sup>10</sup>, G. Ban<sup>4</sup>, Y. Ban<sup>31</sup>, D. Bauer<sup>11</sup>, D. Baygarashev<sup>14</sup>, A. E. Bondar<sup>3,29</sup>, C. Cârloganu<sup>8</sup>, B. Carniol<sup>4</sup>, T. T. Chau<sup>30</sup>, J. K. Chen<sup>35</sup>, S. J. Chen<sup>27</sup>, Y. E. Cheung<sup>27</sup>, W. da Silva<sup>34</sup>, P. D. Dauncey<sup>11</sup>, C. Densham<sup>32</sup>, G. Devidze<sup>36</sup>, P. Dornan<sup>11,\*</sup>, A. Drutskoy<sup>22,25</sup>, V. Duginov<sup>16</sup>, Y. Eguchi<sup>30</sup>, L. B. Epshteyn<sup>3,29,28</sup>, P. Evtoukhovitch<sup>16,2</sup>, S. Fayer<sup>11</sup>, G. V. Fedotovich<sup>3,29</sup>, M. Finger Jr<sup>6</sup>, M. Finger<sup>6</sup>, Y. Fujii<sup>26</sup>, Y. Fukao<sup>18</sup>, J. L. Gabriel<sup>4</sup>, P. Gay<sup>8</sup>, E. Gillies<sup>11</sup>, D. N. Grigoriev<sup>3,29,28</sup>, K. Gritsay<sup>16</sup>, V. H. Hai<sup>40</sup>, E. Hamada<sup>18</sup>, I. H. Hashim<sup>24</sup>, S. Hashimoto<sup>20</sup>, O. Hayashi<sup>30</sup>, T. Hayashi<sup>30</sup>, T. Hiasa<sup>30</sup>, Z. A. Ibrahim<sup>24</sup>, Y. Igarashi<sup>18</sup>, F. V. Ignatov<sup>3,29</sup>, M. Iio<sup>18</sup>, K. Ishibashi<sup>20</sup>, A. Issadykov<sup>14</sup>, T. Itahashi<sup>30</sup>, A. Jansen<sup>38</sup>, X. S. Jiang<sup>13</sup>, P. Jonsson<sup>11</sup>, T. Kachelhoffer<sup>5</sup>, V. Kalinnikov<sup>16</sup>, E. Kaneva<sup>16</sup>, F. Kapusta<sup>34</sup>, H. Katayama<sup>30</sup>, K. Kawagoe<sup>20</sup>, R. Kawashima<sup>20</sup>, N. Kazak<sup>2</sup>, V. F. Kazanin<sup>3,29</sup>, O. Kemularia<sup>10</sup>, A. Khvedelidze<sup>16,10</sup>, M. Koike<sup>39</sup>, T. Kormoll<sup>38</sup>, G. A. Kozlov<sup>16</sup>, A. N. Kozyrev<sup>3,29</sup>, M. Kravchenko<sup>16,1</sup>, B. Krikler<sup>11</sup>, G. Kumsiashvili<sup>30</sup>, Y. Kuno<sup>30</sup>, Y. Kuriyama<sup>19</sup>, Y. Kurochkin<sup>2</sup>, A. Kurup<sup>11</sup>, B. Lagrange<sup>11,19</sup>, J. Lai<sup>30</sup>, M. J. Lee<sup>12,\*</sup>, H. B. Li<sup>13,7</sup>, R. P. Litchfield<sup>11</sup>, W. G. Li<sup>13</sup>, T. Loan<sup>40</sup>, D. Lomidze<sup>10</sup>, I. Lomidze<sup>10</sup>, P. Loveridge<sup>32</sup>, G. Macharashvili<sup>36</sup>, Y. Makida<sup>18</sup>, Y. J. Mao<sup>31</sup>, O. Markin<sup>22,25</sup>, Y. Matsuda<sup>30</sup>, A. Melkadze<sup>10</sup>, A. Melnik<sup>2</sup>, T. Mibe<sup>18</sup>, S. Mihara<sup>18</sup>, N. Miyamoto<sup>30</sup>, Y. Miyazaki<sup>20</sup>, F. Mohamad Idris<sup>24</sup>, K. A. Mohamed Kamal Azmi<sup>24</sup>, A. Moiseenko<sup>16</sup>, M. Moritsu<sup>18</sup>, Y. Mori<sup>19</sup>, T. Motoishi<sup>30</sup>, H. Nakai<sup>30</sup>, Y. Nakai<sup>20</sup>, T. Nakamoto<sup>18</sup>, Y. Nakamura<sup>30</sup>, Y. Nakatsugawa<sup>13</sup>, Y. Nakazawa<sup>30</sup>, J. Nash<sup>26</sup>, H. Natori<sup>12,41</sup>, V. Niess<sup>8</sup>, M. Nioradze<sup>36</sup>, H. Nishiguchi<sup>18</sup>, K. Noguchi<sup>20</sup>, T. Numao<sup>37</sup>, J. O'Dell<sup>32</sup>, T. Ogitsu<sup>18</sup>, S. Ohta<sup>30</sup>, K. Oishi<sup>20</sup>, K. Okamoto<sup>30</sup>, T. Okamura<sup>18</sup>, K. Okinaka<sup>30</sup>, C. Omori<sup>18</sup>, T. Ota<sup>23</sup>, J. Pasternak<sup>11</sup>, A. Paulau<sup>2,16</sup>, D. Picters<sup>30</sup>, V. Ponariadov<sup>1</sup>, G. Quémener<sup>4</sup>, A. A. Ruban<sup>3,29</sup>, V. Rusinov<sup>22,25</sup>, B. Sabirov<sup>16</sup>, H. Sakamoto<sup>30</sup>, P. Sarin<sup>15</sup>, K. Sasaki<sup>18</sup>, A. Sato<sup>30</sup>, J. Sato<sup>33</sup>, Y. K. Semertzidis<sup>12,17</sup>, N. Shigyo<sup>20</sup>, Dz. Shoukavy<sup>2</sup>, M. Slunecka<sup>6</sup>, D. Stöckinger<sup>38</sup>, M. Sugano<sup>18</sup>, T. Tachimoto<sup>30</sup>, T. Takayanagi<sup>30</sup>, M. Tanaka<sup>18</sup>, J. Tang<sup>35</sup>, C. V. Tao<sup>40</sup>, A. M. Teixeira<sup>8</sup>, Y. Tevzadze<sup>†,36</sup>, T. Thanh<sup>40</sup>, J. Tojo<sup>20</sup>, S. S. Tolmachev<sup>3,29</sup>, M. Tomasek<sup>9</sup>, M. Tomizawa<sup>18</sup>, T. Toriashvili<sup>10</sup>, H. Trang<sup>40</sup>, I. Trekov<sup>36</sup>, Z. Tsamalaidze<sup>16,10</sup>, N. Tsverava<sup>16,10</sup>, T. Uchida<sup>18</sup>, Y. Uchida<sup>11,\*</sup>, K. Ueno<sup>18</sup>, E. Velicheva<sup>16</sup>, A. Volkov<sup>16</sup>, V. Vrba<sup>9</sup>, W. A. T. Wan Abdullah<sup>24</sup>, P. Warin-Charpentier<sup>34</sup>, M. L. Wong<sup>30</sup>, T. S. Wong<sup>30</sup>, C. Wu<sup>13,27,30</sup>, T. Y. Xing<sup>13,7</sup>, H. Yamaguchi<sup>18</sup>, A. Yamamoto<sup>18</sup>, M. Yamanaka<sup>21,42</sup>, T. Yamane<sup>30</sup>, Y. Yang<sup>20</sup>, T. Yano<sup>30</sup>, W. C. Yao<sup>30</sup>, B. Yeo<sup>17</sup>, H. Yoshida<sup>30</sup>, M. Yoshida<sup>18</sup>, T. Yoshioka<sup>20</sup>, Y. Yuan<sup>13</sup>, Yu. V. Yudin<sup>3,29</sup>, M. V. Zdorovets<sup>14</sup>, J. Zhang<sup>13</sup>, Y. Zhang<sup>13</sup>, and K. Zuber<sup>38</sup>

<sup>1</sup>Belarusian State University (BSU), 220030, Minsk, Belarus

<sup>2</sup>B. I. Stepanov Institute of Physics, National Academy of Sciences of Belarus, 220072, Minsk, Belarus

<sup>3</sup>Budker Institute of Nuclear Physics (BINP), Novosibirsk, 630090, Russia

<sup>4</sup>Laboratoire de Physique Corpusculaire (LPC), 14000 Caen, France

<sup>5</sup>Computing Center of the National Institute of Nuclear Physics and Particle Physics (CC-IN2P3), 69627 Villeurbanne, France

<sup>6</sup>Charles University, Prague, 116 36, Czech Republic

<sup>7</sup>University of Chinese Academy of Sciences, Beijing 100049, People's Republic of China

<sup>8</sup>Laboratoire de Physique de Clermont (LPC), CNRS-IN2P3 and Université Clermont Auvergne, 63178 Clermont-Ferrand, France

- <sup>9</sup>Czech Technical University, Prague, 160 00, Czech Republic  
<sup>10</sup>Georgian Technical University (GTU), 0160 Tbilisi, Georgia  
<sup>11</sup>Imperial College London, London SW7 2BW, UK  
<sup>12</sup>Institute for Basic Science, Daejeon, 34051, Korea  
<sup>13</sup>Institute of High Energy Physics (IHEP), Beijing 100049, People's Republic of China  
<sup>14</sup>Institute of Nuclear Physics (INP), Almaty, 050032, Kazakhstan  
<sup>15</sup>Indian Institute of Technology Bombay, Mumbai 400076, India  
<sup>16</sup>Joint Institute for Nuclear Research (JINR), Dubna, 141980, Russia  
<sup>17</sup>Korea Advanced Institute of Science and Technology, Daejeon, 34141, Korea  
<sup>18</sup>High Energy Accelerator Research Organization (KEK), Tsukuba, Ibaraki 305-0031, Japan  
<sup>19</sup>Research Reactor Institute, Kyoto University, Kyoto 606-8501, Japan  
<sup>20</sup>Kyushu University, Fukuoka 819-0395, Japan  
<sup>21</sup>Kyushu Sangyo University, Fukuoka 813-8503, Japan  
<sup>22</sup>P. N. Lebedev Physical Institute of the Russian Academy of Sciences, Moscow, 119991, Russia  
<sup>23</sup>Departamento de Física Teórica and Instituto de Física Teórica, IFT-UAM/CSIC, Universidad Autónoma de Madrid, 28049 Madrid, Spain  
<sup>24</sup>National Centre for Particle Physics, Universiti Malaya, 50603 Kuala Lumpur, Malaysia  
<sup>25</sup>Moscow Physical Engineering Institute, National University, Moscow, 115409, Russia  
<sup>26</sup>Monash University, Melbourne, Victoria 3800, Australia  
<sup>27</sup>Nanjing University, Nanjing 210093, People's Republic of China  
<sup>28</sup>Novosibirsk State Technical University (NSTU), Novosibirsk, 630073, Russia  
<sup>29</sup>Novosibirsk State University (NSU), Novosibirsk, 630090, Russia  
<sup>30</sup>Osaka University, Osaka 560-0043, Japan  
<sup>31</sup>Peking University, Beijing 100871, People's Republic of China  
<sup>32</sup>STFC Rutherford Appleton Laboratory (RAL), Didcot, Oxon OX11 0QX, UK  
<sup>33</sup>Saitama University, Saitama 338-8570, Japan  
<sup>34</sup>Laboratory of Nuclear and High Energy Physics (LPNHE), CNRS-IN2P3 and Sorbonne Université, 75252 Paris, France  
<sup>35</sup>Sun Yat-Sen University, Guangzhou 510275, People's Republic of China  
<sup>36</sup>High Energy Physics Institute of I. Javakhishvili Tbilisi State University (HEPI-TSU), 0186 Tbilisi, Georgia  
<sup>37</sup>TRIUMF, Vancouver, BC V6T 2A3, Canada  
<sup>38</sup>Technische Universität Dresden, 01062 Dresden, Germany  
<sup>39</sup>Utsunomiya University, Utsunomiya, Tochigi 321-8585, Japan  
<sup>40</sup>University of Science, Vietnam National University, Ho Chi Minh City, Vietnam  
<sup>41</sup>Present address: Institute of Materials Structure Science, High Energy Accelerator Research Organization, Tsukuba, Ibaraki 305-0801, Japan  
<sup>42</sup>Present address: Nambu Yoichiro Institute of Theoretical and Experimental Physics (NITEP), Osaka City University, Osaka 558-8585, Japan  
<sup>†</sup>Deceased.  
<sup>\*</sup>E-mail: P.Dornan@imperial.ac.uk, myeongjaelee@ibs.re.kr, Yoshi.Uchida@imperial.ac.uk

Received April 25, 2019; Revised September 9, 2019; Accepted October 7, 2019; Published March 13, 2020

The Technical Design for the COMET Phase-I experiment is presented in this paper. COMET is an experiment at J-PARC, Japan, which will search for neutrinoless conversion of muons into electrons in the field of an aluminum nucleus ( $\mu-e$  conversion,  $\mu^-N \rightarrow e^-N$ ); a lepton flavor-violating process. The experimental sensitivity goal for this process in the Phase-I experiment is  $3.1 \times 10^{-15}$ , or 90% upper limit of a branching ratio of  $7 \times 10^{-15}$ , which is a factor of 100 improvement over the existing limit. The expected number of background events is 0.032. To achieve the target sensitivity and background level, the 3.2 kW 8 GeV proton beam from J-PARC will be used. Two types of detectors, CyDet and StrECAL, will be used for detecting the  $\mu-e$  conversion events, and for measuring the beam-related background events in view of the Phase-II experiment, respectively. Results from simulation on signal and background estimations are also described.

## 1. Introduction

Despite successfully predicting and allowing understanding of phenomena in particle physics such as, most notably, the prediction and discovery of the Higgs boson, the Standard Model (SM) cannot provide the ultimate description of nature: it lacks a viable dark matter candidate, offers no explanation for the observed matter–antimatter asymmetry of the Universe, and does not account for neutrino oscillation phenomena. There are also theoretical difficulties such as the hierarchy problem or the number of parameters in the SM, further suggesting the need for physics beyond the SM (BSM).

The observation of neutrino oscillations implies that neutrinos are massive, and that individual lepton flavors are not conserved. This contradicts the original SM formulation, in which neutrinos are massless by construction, and (accidental) symmetry leads to the conservation of total and individual lepton numbers. Such a departure from the SM paradigm also indicates that numerous other processes that are forbidden in the SM might indeed occur in nature. In particular, the violation of flavor conservation in the neutral lepton sector opens the door to the interesting possibility of charged-lepton flavor violation (CLFV). In addition to constituting a discovery of new physics, the observation of a CLFV transition could provide crucial information on the nature of the BSM physics at work. In the presence of new physics, one of the most interesting CLFV processes that can occur is the transition of a muon to an electron in the presence of a nucleus  $\mu^- N \rightarrow e^- N$ . The aim of the COMET experiment [1–3] is to search for the  $\mu^- N \rightarrow e^- N$  process.

COMET is an international collaboration and will take place at the Japan Proton Accelerator Research Complex (J-PARC) in Tokai, Japan. The experiment will be conducted in two phases. Phase-I will employ a simplified detector and will be used to investigate the beam and backgrounds whilst aiming at a sensitivity two orders of magnitude better than the current limit. Phase-II will use the information gained in Phase-I, a much more intense beam, and a more complex detection system to achieve a further two orders of magnitude of sensitivity. A third phase, PRISM (Phase-Rotated Intense Slow Muons) [4,5], is being investigated and could potentially provide a further factor of 100 improvement.

## 2. Charged-lepton flavor violation and muon-to-electron conversion

In the minimal extension of the SM, Dirac masses for neutrinos are incorporated and the total lepton number retains a good symmetry, but leptonic mixings including CLFV are possible. Although allowed at the loop level (mediated by massive neutrinos and  $W^\pm$  bosons), CLFV processes such as radiative decays ( $\ell_i \rightarrow \ell_j \gamma$ ) yield extremely small rates, being suppressed by  $(m_\nu/M_W)^2$ , where  $m_\nu$  and  $M_W$  are the masses of the neutrino and W boson, respectively. As an example, in the SM extended with massive Dirac neutrinos, the predicted rate for a  $\mu \rightarrow e\gamma$  transition is [6–9]

$$\text{BR}(\mu \rightarrow e\gamma) = \frac{3\alpha}{32\pi} \left| \sum_{j=1}^3 U_{ej} U_{\mu j}^* \frac{m_{\nu_j}^2}{M_W^2} \right|^2 \simeq \mathcal{O}(10^{-55} - 10^{-54}), \quad (1)$$

where best-fit values for neutrino data ( $m_{\nu_j}$  for the neutrino mass and  $U_{ij}$  for the element of the PMNS (Pontecorvo–Maki–Nakagawa–Sakata) neutrino mixing matrix) were used.

The observation of a CLFV signal would thus require a more ambitious extension of the SM. Many appealing new physics models—motivated by explaining the observational and theoretical issues of the SM—not only allow for CLFV, but predict rates that could be within current and future experimental sensitivity. Muons are one of the best laboratories to look for CLFV, and several

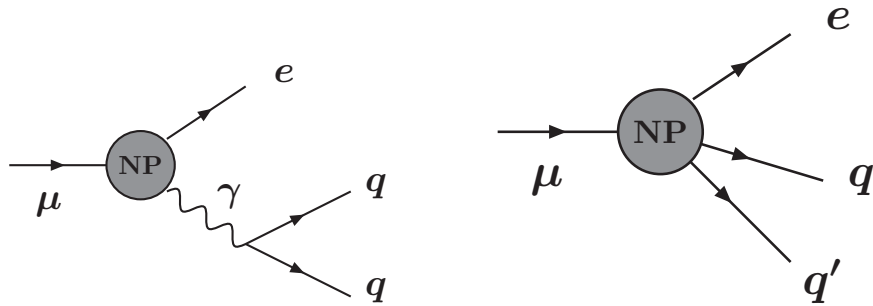


**Fig. 1.** Schematic description of the two (tree-level) effective contributions to  $\mu-e$  conversion: in the left (right) panel is the photonic (four-fermion/contact) interaction. The shaded circles denote a BSM flavor-violating interaction.

processes can be studied, all associated with the conversion of muon-to-electron flavor. In addition to the radiative and three-body decays,  $\mu \rightarrow e\gamma$  and  $\mu \rightarrow 3e$ , flavor-violating muon conversions can occur in the presence of nuclear Coulomb interactions. This is the case of  $\mu^-N \rightarrow e^-N$ , a process that yields a monoenergetic electron and hence an excellent experimental signature.

### 2.1. $\mu^-N \rightarrow e^-N$ conversion

One of the most important muon CLFV processes is the coherent neutrinoless conversion of muons to electrons ( $\mu-e$  conversion). When a negatively charged muon is stopped in matter, a muonic atom is formed and, after cascading down the energy levels, the muon becomes bound in the  $1s$  ground state. It will then normally either decay in orbit ( $\mu^- \rightarrow e^- \nu_\mu \bar{\nu}_e$ ) or be captured by the nucleus  $\mu^-N(A, Z) \rightarrow \nu_\mu N(A, Z - 1)$ . However, BSM processes can lead to neutrinoless muon capture:

$$\mu^- + N(A, Z) \rightarrow e^- + N(A, Z). \quad (2)$$

This violates the conservation of individual lepton flavors,  $L_e$  and  $L_\mu$ , but conserves the total lepton number,  $L_{\text{total}}$ .

The branching or conversion ratio<sup>1</sup> of  $\mu-e$  conversion is defined as

$$\text{BR}(\mu^-N \rightarrow e^-N) \equiv \frac{\Gamma(\mu^-N \rightarrow e^-N)}{\Gamma(\mu^-N \rightarrow \text{all})}, \quad (3)$$

in which  $\Gamma$  is the decay width. The time distribution of  $\mu-e$  conversion follows the lifetime of a muonic atom, which depends on the type of nucleus. For aluminum it is 864 ns.

*Photonic and non-photonic contributions* As schematically depicted in the panels of Fig. 1, two distinct contributions can give rise to  $\mu-e$  conversion: the photonic (electromagnetic) dipole contribution, responsible for  $\mu \rightarrow e\gamma$  decays and the non-photonic (contact) interaction, which does not contribute to radiative CLFV muon decays. While for the former the photon is absorbed by the capturing nucleus, for the latter CLFV is due to the exchange of heavy virtual particles that couple to the quark system<sup>2</sup>. This is in contrast to the  $\mu \rightarrow e\gamma$  process, which is only sensitive to

<sup>1</sup> As  $\mu-e$  conversion is not a decay process, it is correct to call its probability a conversion ratio or CR. However, as it is widely called a branching ratio in the various literature, we call it a branching ratio or BR throughout this paper.

<sup>2</sup> To calculate the rate of  $\mu-e$  conversion, proper treatments from the quark level to the nucleon level and to the nucleus level have to be made [10].

electromagnetic dipole interactions. Thus if CLFV transitions are observed, a comparison between the results from dedicated experiments (e.g., MEG and COMET) can be a powerful discriminator between CLFV extensions of the SM. With solely BSM dipole interactions [11] the rate of the  $\mu \rightarrow e\gamma$  process is typically  $\mathcal{O}(200\text{--}400)$  times that of the neutrinoless  $\mu\text{-}e$  conversion process [12]. The ratio between the long-distance photonic contribution to the  $\mu\text{-}e$  conversion process and the rate of  $\mu^+ \rightarrow e^+\gamma$  decays can be parametrized by

$$\frac{\text{BR}(\mu^+ \rightarrow e^+\gamma)}{\text{BR}(\mu^-N \rightarrow e^-N)} = \frac{96\pi^3\alpha}{G_F^2 m_\mu^4} \frac{1}{3 \times 10^{12} B(A, Z)} \sim \frac{428}{B(A, Z)}, \quad (4)$$

where  $B(A, Z)$  represents the rate dependence on the target nucleus with mass and atomic numbers ( $A$  and  $Z$ ). This has been calculated based on various approximations; e.g., using  $B(A = 27, Z = 13) = 1.1$  [13], one obtains a  $\text{BR}(\mu^+ \rightarrow e^+\gamma)/\text{BR}(\mu N \rightarrow e N)$  of 389 for  $^{27}\text{Al}$ .

A wide variety of new physics models mediated by (pseudo)scalar, (axial) vector, or tensor currents can give rise to short-distance (non-photonic) CLFV interactions. Following Ref. [14], the width for muon-to-electron conversion (for a target  $N$ ) can be written as

$$\begin{aligned} \Gamma(\mu^-N \rightarrow e^-N) = & \frac{m_\mu^5}{4\Lambda^4} \left| eC_L^D D_N + 4 \sum_{h=p,n} \left\{ G_F m_\mu m_h S_N^{(h)} \left( \sum_{q=u,d,s} \frac{C_{qq}^{SLL} + C_{qq}^{SLR}}{m_\mu m_q G_F} f_{Sh}^{(q)} + \tilde{C}_{gg}^L f_{Gh} \right) \right. \right. \\ & \left. \left. + V_N^{(h)} \left( \sum_{q=u,d,s} (C_{qq}^{VRL} + C_{qq}^{VRR}) f_{Vh}^{(q)} \right) \right\} \right|^2 + (L \leftrightarrow R). \end{aligned} \quad (5)$$

where  $C$  denotes the Wilson coefficients evaluated at the nucleon scale (e.g.,  $C^D$  is responsible for the dipole interactions at the origin of  $\mu \rightarrow e\gamma$ ),  $f_n^{(q)}$  is the nucleon form factors, and the quantities  $D_N$ ,  $S_N$  and  $V_N$  are target-dependent.

As discussed in Ref. [15], while the current experimental bounds on  $\mu \rightarrow e\gamma$  are clearly powerful in constraining the dipole operators (and indirectly other scalar and tensor operators, via mixing effects), neutrinoless muon-to-electron conversion is the most sensitive observable to explore operators involving quarks; it also appears to be the best to study (most) vector interactions and, as a result of the cleaner experimental conditions, it may even eventually prove more sensitive to the dipole operators than  $\mu \rightarrow e\gamma$ . For the four-fermion operators, those involving  $b$ ,  $c$ , or  $s$  quarks can lead to significant contributions and thus to important constraints due to the renormalization effects, whilst the three-body decay,  $\mu \rightarrow 3e$ , is the most powerful observable to explore and constrain the four-fermion operators with  $\mu eee$  flavor structure. An example of the comparative constraining power of different CLFV processes on pairs of effective couplings can be seen in Fig. 2 (obtained under several simplifying assumptions).

*Dependence on muon stopping target material* The rates of coherent  $\mu\text{-}e$  conversion for general effective CLFV interactions (such as dipole, scalar, and vector interactions) have been calculated for various nuclei [14,16] taking into account relativistic wave functions as well as the proton and neutron distributions (with associated ambiguities). The results, shown in Fig. 3, indicate that the branching ratios for  $\mu\text{-}e$  conversion increase for light nuclei up to the atomic number of  $Z \sim 30$ , remain large for the region of  $Z = 30\text{--}60$ , and then decrease for heavy nuclei of  $Z > 60$ . It should be noted that the different physics models give different estimations of the  $\mu\text{-}e$  conversion rates,

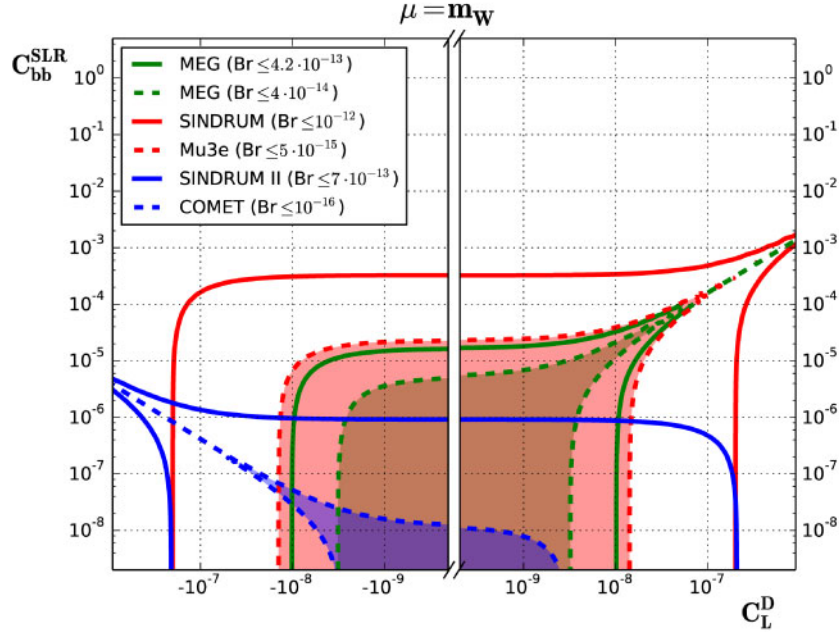


**Fig. 2.** Allowed regions in the  $C_L^D$ – $C_{bb}^{SLR}$  parameter space, from  $\mu \rightarrow e\gamma$  (green),  $\mu \rightarrow 3e$  (red), and  $\mu \rightarrow e$  conversion (blue), for current experimental bounds (full lines) and future sensitivities (dashed lines). From Ref. [15].

which also depend on the target materials. Therefore, experiments with different target materials and comparisons of the results are important to give a hint to the CLFV model.

*Spin-dependent and spin-independent contributions* CLFV tensor and axial-vector four-fermion operators could also contribute to  $\mu$ – $e$  conversion; these couple to the spins of nucleons, and can therefore mediate a spin-dependent  $\mu$ – $e$  conversion [17,18]. As these have a different atomic number dependence than the spin-independent terms this could in principle be used to investigate the operators responsible.

## 2.2. CLFV models and $\mu$ – $e$ conversion

BSM models can lead to significant CLFV contributions via the introduction of new sources of flavor violation (corrections to SM vertices, or new flavor-violating interactions) and/or new currents. The size of these contributions depends upon the new physics model; however, the generic features for  $\mu^- N \rightarrow e^- N$  conversion can be illustrated with the following (new) interaction terms in the BSM Lagrangian:

$$\mathcal{L}_1 \sim g_{e\mu}^\phi \bar{\mu} e \phi + g_{qq}^\phi \bar{q} q \phi, \quad (6)$$

$$\mathcal{L}_2 \sim h_{\mu\psi\phi} \bar{\mu} \psi \phi + h_{e\psi\phi} \bar{e} \psi \phi. \quad (7)$$

In Eq. (6),  $\phi$  generically refers to a scalar or vector boson (under the assumption of appropriate Lorentz contractions), while  $g_{ff}^\phi$  denotes its couplings to fermions, which must be non-diagonal for charged leptons. In this case contributions to CLFV can occur both at tree level, as depicted in Fig. 4 ( $t$ -channel), or at higher orders.

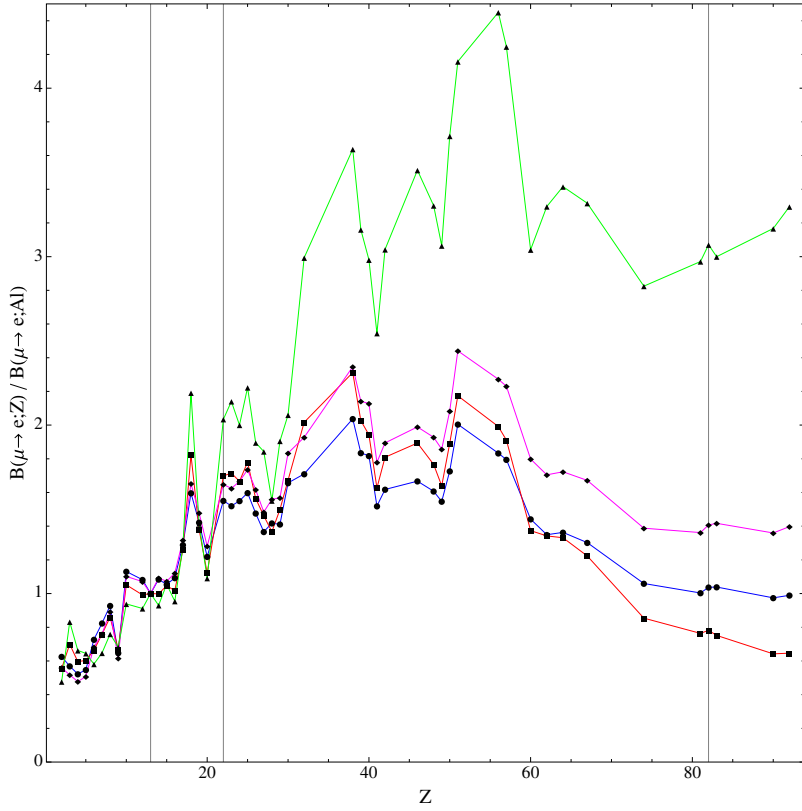


**Fig. 3.** Target dependence of the muon-to-electron conversion rate in different single-operator dominance models. The different lines correspond to the  $\mu-e$  conversion rate for a given atomic number  $Z$ , normalized to the rate in aluminum ( $Z = 13$ ), as a function of the atomic number, for four theoretical models: dipole interaction (blue), scalar interaction (red), vector interaction with photons (magenta), vector interaction with  $Z^0$  bosons (green). The vertical lines correspond to  $Z = 13$  (Al),  $Z = 22$  (Ti), and  $Z = 82$  (Pb). Taken from Ref. [14].

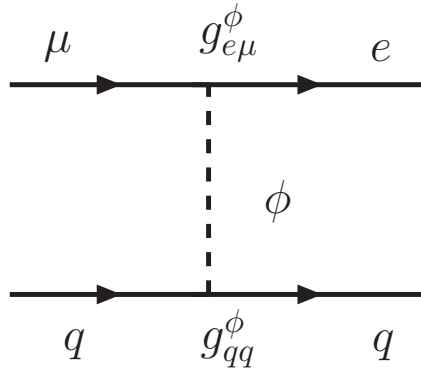


**Fig. 4.** Schematic representation of  $\mu^- N \rightarrow e^- N$  conversion at the tree level ( $t$ -channel exchange), mediated by a scalar or vector boson ( $\phi$ ).

The possibility referred to in Eq. (7) requires new fermions  $\psi$  in addition to the vector/scalar bosons. The combination  $\psi\phi$  must carry lepton flavor, and the coupling  $h_{\ell\psi\phi}$  must be non-diagonal. In BSM constructions, at least one of  $\psi$  and  $\phi$  is a new particle, and often both are (as in models in which some symmetry ensures that new particles are always pair-produced). A diagrammatic view of the new contributions can be found in Fig. 5.

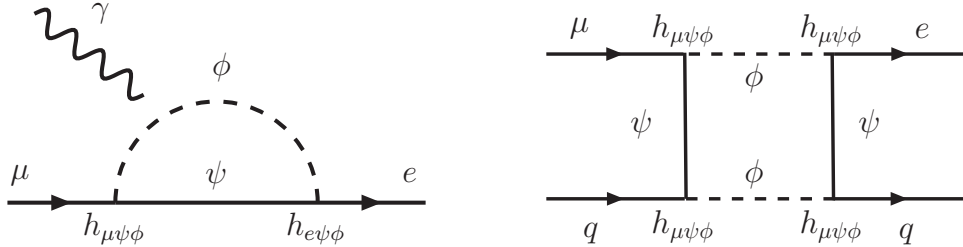


**Fig. 5.** Schematic representation of photonic contributions to  $\mu$ - $e$  flavor transitions (left panel), and of the box-diagram contribution to  $\mu^- N \rightarrow e^- N$  conversion (right panel), in the presence of new fermions ( $\psi$ ) and new vector/scalar bosons ( $\phi$ ).

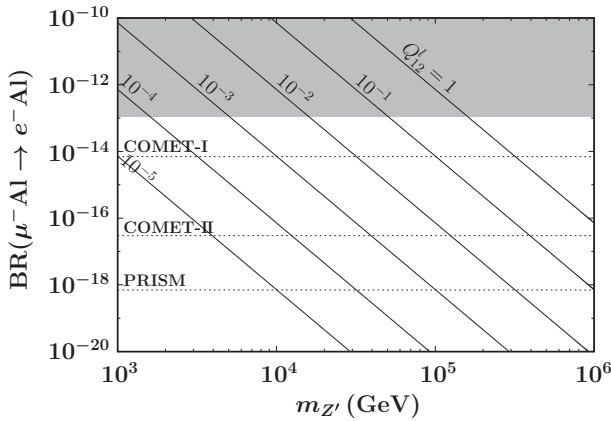


**Fig. 6.** The rate of neutrinoless muon-to-electron conversion as a function of the  $Z'$  mass. Diagonal lines denote regimes for the CLFV coupling  $Q_{12}^\ell(Z'\bar{\ell}_i\ell_i)$ . The gray region is excluded by the SINDRUM experiment. COMET Phases I and II are denoted by “COMET-I” and “COMET-II” here.

*Tree-level contributions to  $\mu$ - $e$  conversion* Many BSM models predict the existence of a massive neutral vector boson, often called a  $Z'$ . One example is the sequential Standard Model (SSM), in which the interaction of the  $Z'$  and ordinary matter inherit the structure of the SM interactions. CLFV arises from new flavor-violating couplings of the vector boson to leptons  $Z'\bar{\ell}_i\ell_i$ , whose strength is parametrized by  $Q_{ij}^\ell$  couplings [19]. The LHC experiments have searched for neutral heavy particles decaying into dileptons of different flavor  $e^\pm\mu^\mp$ , and have placed a lower limit on the mass of an SSM  $Z'$ ,  $m_{Z'} \gtrsim 3.01 \text{ TeV}$  (at 95% C.L.), for  $Q_{12}^\ell = 1$  [20]. Figure 6 displays the rate of neutrinoless muon-to-electron conversion as a function of the SSM  $Z'$  mass, for different regimes of the CLFV coupling  $Q_{12}^\ell$ . This clearly shows that  $\mu^- N \rightarrow e^- N$  conversion offers a sensitivity to new physics scales well beyond the reach of the LHC.

Another case is the type III realization of the seesaw mechanism, in which the SM content is extended by two or more generations of fermion triplets,  $\Sigma$  [21,22]. The charged states of the triplet mix with charged leptons, leading to lepton flavor-violating couplings to the  $Z^0$  boson. This induces significant differences in the contributions to CLFV observables. Radiative decays remain a one-loop transition whilst  $\ell_i \rightarrow 3\ell_j$  decays and neutrinoless  $\mu$ - $e$  conversion can occur at tree level. For the  $\mu$ - $e$  system one finds [23]

$$\text{BR}(\mu \rightarrow e\gamma) = 1.3 \times 10^{-3} \times \text{BR}(\mu \rightarrow 3e) = 3.1 \times 10^{-4} \times \text{BR}(\mu^- \text{Ti} \rightarrow e^- \text{Ti}), \quad (8)$$

strikingly different to other seesaw realizations.

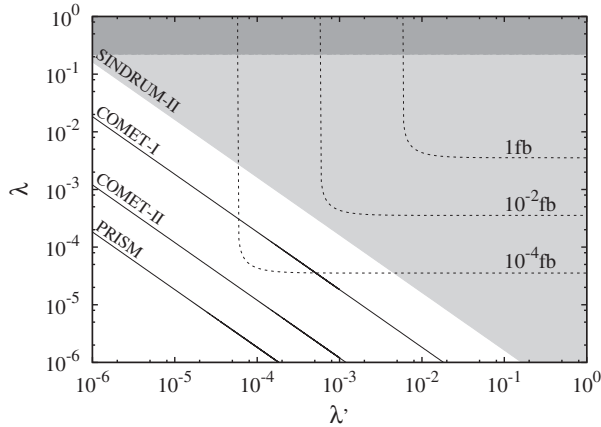


**Fig. 7.** Exclusion contours in  $\text{BR}(\mu^- \text{Al} \rightarrow e^- \text{Al})$  and  $\sigma(pp \rightarrow \mu^- e^+)$  in an RPV scenario, for  $m_{\tilde{\nu}} = 1 \text{ TeV}$ , and  $\lambda = \lambda_{312} = \lambda_{321} = -\lambda_{132} = -\lambda_{231}$ . The shaded regions denote limits on  $\lambda$  (dark shaded band) and the combination  $(\lambda, \lambda')$  (light shaded region) arising from CLFV muonium–antimuonium oscillation searches and from SINDRUM bounds on  $\mu^- N \rightarrow e^- N$  conversion, respectively. COMET Phases I and II are denoted by “COMET-I” and “COMET-II” here. Taken from Ref. [25].

SUSY models that violate R-parity can lead to sizable CLFV rates giving tree-level contributions to  $\mu^- N \rightarrow e^- N$  conversion mediated by (*t*-channel) scalar exchange. In this case the scalar neutrino  $\tilde{\nu}_{iL}$  plays the role of  $\phi$  in Eq. (6). LHC searches for different flavor dileptons have set limits on the  $\tilde{\nu}_\tau$  mass,  $m_{\tilde{\nu}_\tau} > 1.0 \text{ TeV}$  for  $\lambda_{132} = \lambda_{231} = \lambda'_{311} = 0.01$ , and  $m_{\tilde{\nu}_\tau} > 3.3 \text{ TeV}$  for  $\lambda_{132} = \lambda_{231} = \lambda'_{311} = 0.2$  [24] (with 1, 2, 3 denoting  $e$ ,  $\mu$ , and  $\tau$  flavors). Figure 7 shows the contour of  $\text{BR}(\mu^- \text{Al} \rightarrow e^- \text{Al})$  and  $\sigma(pp \rightarrow \mu^- e^+)$  for  $m_{\tilde{\nu}} = 1 \text{ TeV}$ . The LHC limit excludes only part of the upper-right corner, leading to much looser constraints than those imposed by the SINDRUM limit on  $\mu^- N \rightarrow e^- N$  conversion. In fact, a synergy of different muon CLFV processes, muon  $g-2$ , and direct LHC search results leads to powerful constraints on the RPV model parameters [25].

BSM contributions to  $\mu^- N \rightarrow e^- N$  conversion can also be mediated by the exchange of a scalar particle in the *s*-channel. This corresponds to interactions of the type  $h_{\ell q \phi} \ell q \phi$ , as given in Eq. (7) and can be realized if the scalar mediator carries both hadron and lepton numbers, as is the case of (scalar) leptoquark models [26].

*Loop contributions to μ-e conversion* Several higher-order processes including photons, Z and Higgs penguins and boxes mediated by fermions and vector/scalar bosons, with both SM and new exotic particles, can induce  $\mu^- N \rightarrow e^- N$ . Although contributions can occur at two-loop order or even higher levels, most BSM constructions already induce CLFV observables at the loop level.

From the interaction terms in Eq. (7), when both  $\psi$  and  $\phi$  are new particles, CLFV transitions are only realized by higher-order processes: loops are constructed by connecting  $\mu$  to  $e$  via exotic fermion ( $\psi$ ) and boson ( $\phi$ ) closed lines. The addition of interactions with quarks such as  $\bar{q}\psi\phi$  allows for box-diagram contributions to  $\mu^- N \rightarrow e^- N$  conversion. An illustration is provided by SUSY models with R-parity conservation, with an example of the contributions to CLFV observables depicted in Fig. 8.

General SUSY models (as is the case of the minimal supersymmetric Standard Model, MSSM) do not offer an explanation for neutrino oscillation, and are thus a good illustrative example of having CLFV completely decorrelated from flavor violation in the *neutral* lepton sector. An estimate of generic SUSY contributions to radiative lepton decays (e.g.,  $\mu \rightarrow e\gamma$ ) arising from loops mediated

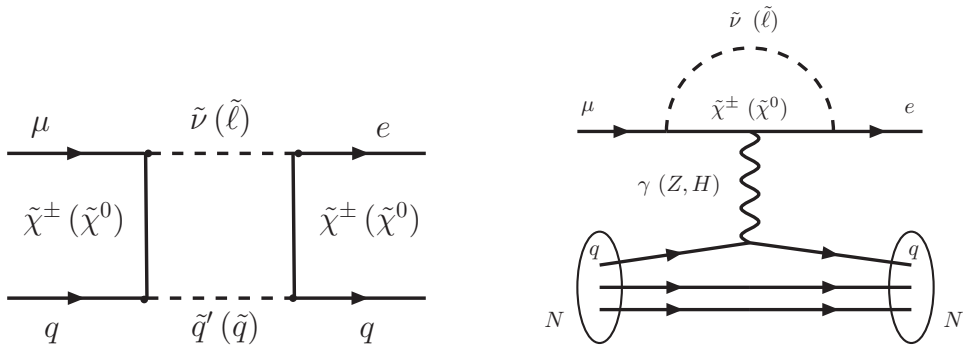


**Fig. 8.** Diagrams for  $\mu^- N \rightarrow e^- N$  conversion via box (left) and penguin (right) diagrams, arising from SUSY R-parity conserving interactions;  $\chi$  denotes a neutralino or chargino,  $\tilde{\nu}(\tilde{\ell})$  represents a scalar lepton (neutral or charged), and  $\tilde{q}$  stands for a scalar quark.

by charged sleptons (sneutrinos) and neutralinos (charginos) leads to the approximate expression

$$\text{BR}(\mu \rightarrow e\gamma) \sim \frac{\alpha}{4\pi} \left( \frac{M_W}{M_{\text{SUSY}}} \right)^4 \sin^2 \theta_{\tilde{e}\tilde{\mu}} \left( \frac{\Delta m_{\tilde{\ell}}^2}{M_{\text{SUSY}}^2} \right)^2, \quad (9)$$

in which  $M_{\text{SUSY}}$  denotes the SUSY breaking scale,  $\theta_{\tilde{e}\tilde{\mu}}$  and  $\Delta m_{\tilde{\ell}}^2$  corresponding to the slepton mixing angle and mass square difference.

Similarly to the tree-level case, in a regime in which virtual photon exchange proves to be the dominant contribution to  $\mu$ - $e$  conversion (e.g., Refs. [27,28] and the comparative study of Ref. [29]), one also recovers a relation between the latter and the radiative decays:

$$\text{BR}(\mu^- N \rightarrow e^- N) \approx \mathcal{O}(\alpha) \times \text{BR}(\mu \rightarrow e\gamma). \quad (10)$$

### 2.3. Other possible BSM processes

#### 2.3.1. Lepton-number-violating $\mu^- N \rightarrow e^+ N^{(\prime)}$ conversion

If the new physics responsible for CLFV also includes a source of lepton number violation (LNV; in general associated with the presence of BSM Majorana states), then the muonic atom can undergo both a CLFV and LNV transition [30]:

$$\mu^- + N(A, Z) \rightarrow e^+ + N'(A, Z - 2). \quad (11)$$

Having different initial and final state nuclei precludes the coherent enhancement of the transition amplitude—which implies that it will not be augmented in large- $Z$  atoms. The experimental signal is less clean than that of the coherent conversion; the emitted positron is no longer monoenergetic and there are more sources of background [31–43].

#### 2.3.2. CLFV muonic atom decay $\mu^- e^- \rightarrow e^- e^-$

In the presence of new physics, there is another CLFV process that can occur in a muonic atom, the Coulomb-enhanced decay into a pair of electrons [44],

$$\mu^- + e^- \rightarrow e^- + e^-, \quad (12)$$

in which the initial fermions are the muon and the atomic 1s electron. As with the neutrinoless conversion, this can be induced by dipole and contact interactions. Experimentally this has several

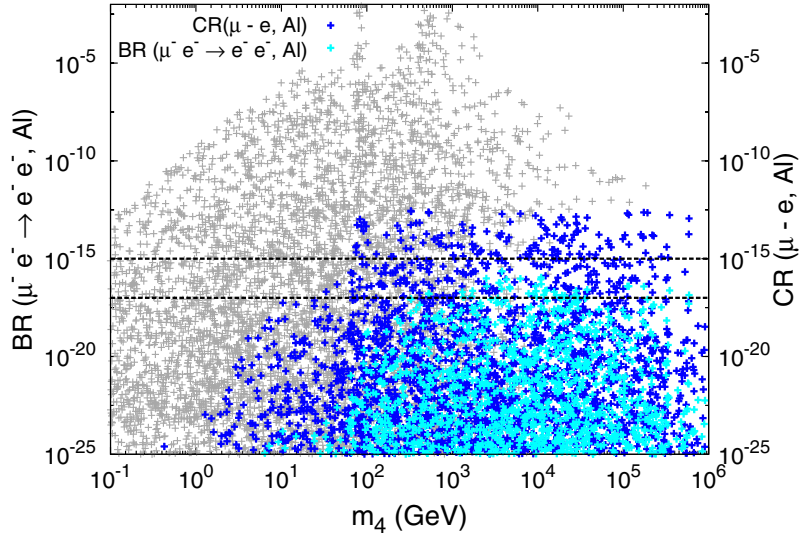


**Fig. 9.**  $\mu-e$  conversion (blue) and  $\mu e \rightarrow ee$  (cyan) for aluminum targets, as a function of the sterile fermion mass ( $m_4$ ), in a “3+1” toy model; horizontal dashed lines denote COMET’s Phase-I and II sensitivities [45].

advantages compared with  $\mu \rightarrow e\gamma$ , or  $\mu \rightarrow 3e$ . Compared with  $\mu \rightarrow e\gamma$  the CLFV muonic atom decay is sensitive to both contact and dipole interactions and its measurement is easier as no photon detection is involved; when compared to  $\mu \rightarrow 3e$ , the new observable has a larger phase space and a cleaner experimental signature, consisting of back-to-back electrons with a well defined energy ( $\sim m_\mu/2$ ).

A phenomenological study of this observable was carried out in Ref. [45], in the framework of the SM extended by sterile fermions (ad hoc extensions and a (3,3) inverse seesaw realization); the comparative prospects for the COMET experiment are displayed in Fig. 9.

#### 2.4. Experimental aspects of $\mu^- N \rightarrow e^- N$

The event signature of coherent neutrinoless  $\mu-e$  conversion in a muonic atom is the emission of a monoenergetic single electron in a defined time interval. The energy of the signal electron ( $E_{\mu e}$ ) is given by

$$E_{\mu e} = m_\mu - B_\mu - E_{\text{recoil}} \quad (13)$$

where  $m_\mu$  is the muon mass,  $B_\mu$  is the binding energy of the 1s-state muonic atom, and  $E_{\text{recoil}}$  denotes the nuclear recoil energy, which is small. For aluminum,  $E_{\mu e} = 104.97$  MeV and the lifetime of the muonic atom is 864 ns.

This makes neutrinoless  $\mu-e$  conversion very attractive experimentally. Firstly, the  $e^-$  energy of about 105 MeV is well above the endpoint energy of the muon decay spectrum ( $\sim 52.8$  MeV). Secondly, since the event signature is a monoenergetic electron, no coincidence measurement is required. Thirdly, the long lifetime means that backgrounds associated with the beam flash can be eliminated. Thus the search for this process has the potential to improve sensitivity by using a high muon rate without suffering from accidental background events. Backgrounds are discussed in more detail in Sect. 10.

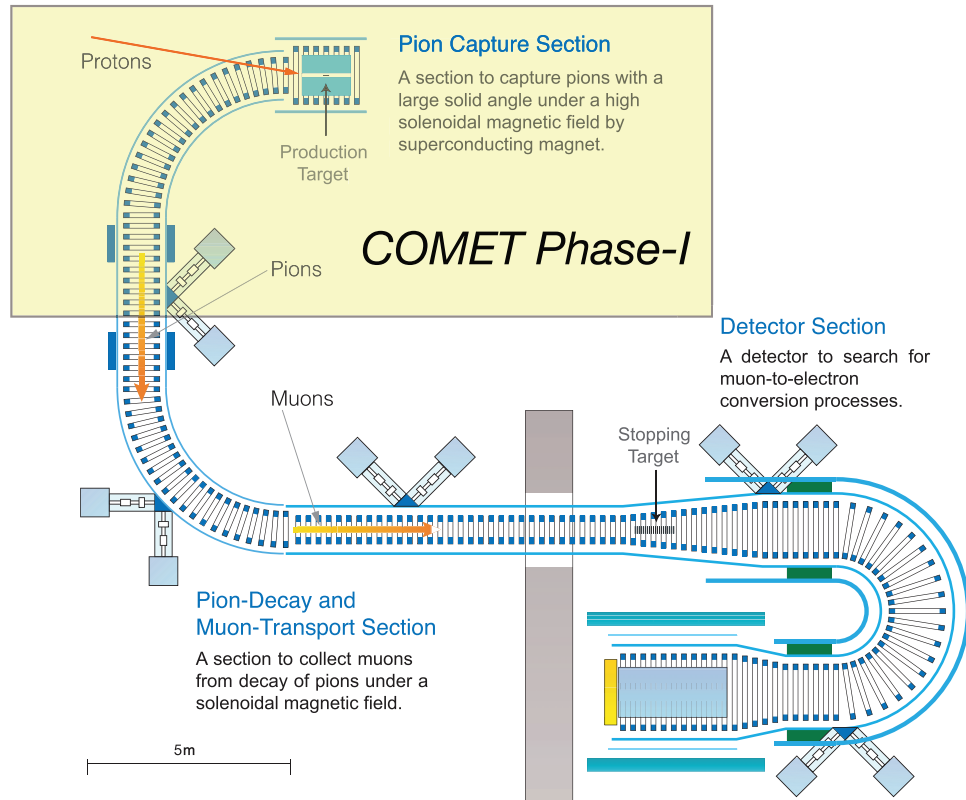


**Fig. 10.** Schematic layout of COMET (Phase-II) and COMET (Phase-I) (not to scale).

### 3. The COMET experiment

COMET stands for COherent Muon to Electron Transition and the experiment seeks to measure the neutrinoless, coherent transition of a muon to an electron ( $\mu-e$  conversion) in the field of an aluminum nucleus. The experiment will be carried out using a two-staged approach.

COMET Phase-I aims at a single-event sensitivity (SES) of  $3.1 \times 10^{-15}$ , roughly a factor 100 better than the current experimental limit. The goal of the full experiment is an SES of  $2.6 \times 10^{-17}$ , which we refer to as Phase-II. This ultimate sensitivity goal is a factor of about 10 000 better than the current experimental limit of  $B(\mu^- + \text{Au} \rightarrow e^- + \text{Au}) \leq 7 \times 10^{-13}$  from SINDRUM-II at PSI [46].

A schematic layout of the COMET experiment is shown in Fig. 10. The experiment will be carried out in the Nuclear and Particle Physics Experimental Hall (NP Hall) at J-PARC using a bunched 8 GeV proton beam that is slow-extracted from the J-PARC main ring. Muons for the COMET experiment will be generated from the decay of pions produced by collisions of the 8 GeV proton beam on a production target. The yield of low-momentum muons transported to the experimental area is enhanced using a superconducting pion-capture solenoid surrounding the proton target in the pion-capture section shown in Fig. 10. Muons are momentum- and charge-selected using curved superconducting solenoids in the muon-transport section, before being stopped in an aluminum target. The signal electrons from the muon stopping target are then transported by additional curved solenoids to the main detector, a straw-tube tracker and electron calorimeter, called the StrECAL detector.

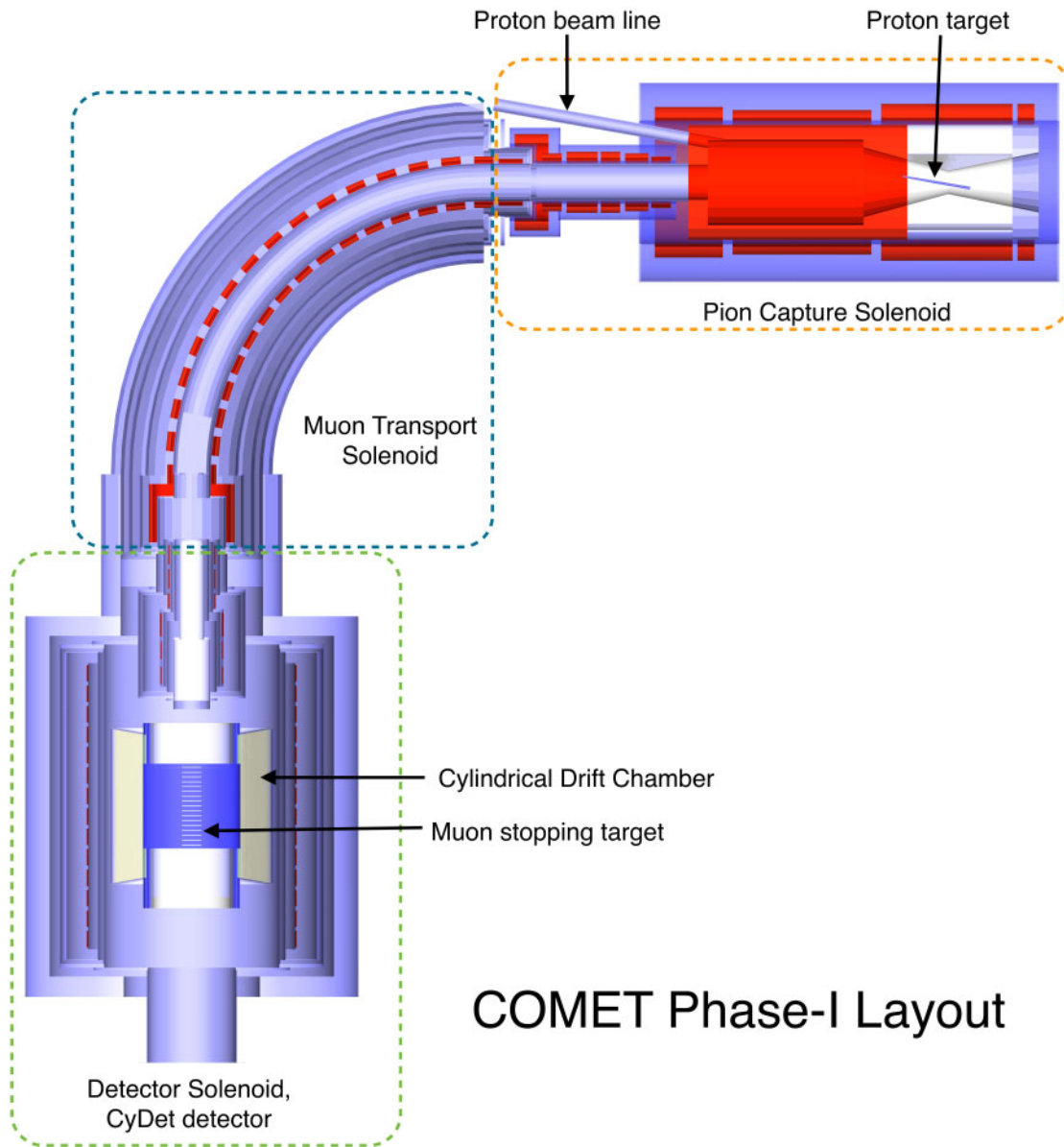


**Fig. 11.** Schematic layout of COMET Phase-I.

### 3.1. COMET Phase-I

The COMET Phase-I will have the pion-capture and muon-transport sections up to the end of the first  $90^\circ$  bend of the full experiment. The muons will then be stopped in the aluminum target at the center of a cylindrical drift chamber in a 1 T magnetic field. A schematic layout of the COMET Phase-I setup is shown in Fig. 11 and an illustration of how COMET Phase-I relates to Phase-II is given in Fig. 10. For COMET Phase-I, the primary detector for the neutrinoless  $\mu-e$  conversion signals consists of a cylindrical drift chamber and a set of trigger hodoscope counters, referred to as the CyDet detector. The experimental setup for Phase-I will be augmented with prototypes of the Phase-II StrECAL detector. As well as providing valuable experience with the detectors, the StrECAL and CyDet detectors will be used to characterize the beam and measure backgrounds to ensure that the Phase-II single-event sensitivity of  $2.6 \times 10^{-17}$  can be realized [47].

**Table 1.** Comparison of experimental plans of COMET Phase-I and II and the SINDRUM-II experiment.

Experiment	SINDRUM-II	COMET Phase-I	COMET Phase-II
Location	PSI (Switzerland)	J-PARC (Japan)	J-PARC (Japan)
Proton energy	590 MeV	8 GeV	8 GeV
Proton beam power		3.2 kW	56 kW
$N$ (proton)		$3.2 \times 10^{19}$	$6.8 \times 10^{20}$
$N$ (stopped muon)	$4.37 \times 10^{13}$	$1.5 \times 10^{16}$	$1.1 \times 10^{18}$
Transport solenoid shape	Linear	Half C-shape	Full C-shape
Muon target material	Au	Al	Al
Sensitivity (90% C.L.)	$7 \times 10^{-13}$	$7 \times 10^{-15}$	$2.6 \times 10^{-17}$
Total DAQ time	81 days	$\sim 150$ days	$\sim 180$ days

For Phase-I a total number of protons on target (POT) of  $3.2 \times 10^{19}$  is planned; this will provide around  $1.5 \times 10^{16}$  muons stopped in the target. This will enable the design goal of COMET Phase-I to be achieved: a single-event sensitivity, which, in the absence of a signal, translates to a 90% confidence level branching ratio limit of  $7 \times 10^{-15}$ . This is a factor of about 100 better than the current limit on gold from SINDRUM-II [46]. The important experimental parameters of COMET Phase-I and II and the SINDRUM-II experiment are compared in Table 1.

### 3.2. COMET requirements

In order to obtain the desired improvement in sensitivity, the experiment requires an intense muon source, coming from a pulsed proton beam with a high inter-bunch extinction factor.

*Highly intense muon source* To achieve an experimental sensitivity better than  $10^{-16}$ ,  $\mathcal{O}(10^{18})$  muons are needed. Two methods are adopted to increase the muon beam intensity. One is to use a high-power proton beam from J-PARC, the other is to use a highly efficient pion collection system. The latter is achieved by surrounding the proton target with a 5 T superconducting solenoid. The principle of this pion-capture system has been experimentally demonstrated at the MuSIC (Muon Science Innovative beam Channel) facility at the Research Centre for Nuclear Physics (RCNP), Osaka University [48].

*Proton beam pulsing with high proton extinction* There are several potential sources of electron background events in the signal energy region, one of which is prompt beam-related background events. In order to suppress the occurrence of such background events, a pulsed proton beam will be employed, where proton leakage between the pulses is tightly controlled. As a muon in an aluminum muonic atom has a lifetime of the order of  $1 \mu\text{s}$ , a pulsed beam can be used to eliminate prompt beam background events by performing measurements in a delayed time window, provided that the beam pulses are shorter than this lifetime and the spacing between them is comparable or longer. Stringent requirements on the beam extinction, defined as the number of leakage protons with respect to the number of protons in a beam pulse, are necessary. Tuning of the proton beam in the accelerator ring, as well as making use of additional extinction-improving techniques (such as modifying the timing of kicker magnets), will also be done.

*Curved solenoids for charge and momentum selection* High-momentum muons can produce electron background events in the energy region of 100 MeV, and therefore must be eliminated. This is

achieved by transporting the pion/muon beam through a system of curved superconducting solenoids. As they pass through the curved solenoid, the centers of the helical motion of the charged particles drift perpendicularly to the plane in which their paths are curved, with the magnitude of the drift proportional to their momentum. To compensate for this a dipole field parallel to the drift direction will be applied for a given reference momentum to keep the centers of the helical trajectories in the bending plane. Hence, with suitably placed collimators, high-momentum and positively charged particles can be eliminated. Since the muon momentum dispersion is proportional to a total bending angle, the COMET C-shape beam line produces a larger separation of the muon tracks as a function of momentum and hence an improved momentum selection. In COMET Phase-II, additional curved solenoids will be used in a C-shaped electron transport system between the muon stopping target and the electron spectrometer to eliminate low-momentum backgrounds to the electron signal.

### 3.3. The Phase-I program

The purpose of COMET Phase-I is two-fold. The first is to make background measurements for COMET Phase-II, and the second is a search for  $\mu-e$  conversion at an intermediate sensitivity. COMET Phase-I serves several roles that are highly complementary to the Phase-II experiment. It provides a working experience of many of the components to be used in Phase-II and enables a direct measurement of backgrounds. Significantly, it will also produce competitive physics results, both of the  $\mu-e$  conversion process and of other processes that COMET Phase-II cannot investigate.

*Background measurements* Currently, background levels must be estimated by extrapolating the existing data over several orders of magnitude. Phase-I will be used to obtain data-driven estimates of backgrounds, and hence inform the detailed design of COMET Phase-II. Using a shorter 90° muon-transport solenoid in Phase-I enables the investigation of the secondary beam in the kinematic region that will be used in Phase-II. In Phase-I the StrECAL detector will be placed at the downstream end of the muon-transport beam line and will be dedicated to background measurements, in particular:

- direct measurement of the inter-bunch extinction factor;
- direct measurement of unwanted secondary particles in the beam line such as pions, neutrons, antiprotons, photons, and electrons;
- direct measurement of background processes that have not been measured at the required accuracy, such as muon decays in orbit and radiative muon capture.

*Search for  $\mu-e$  conversion* Even in this partial configuration, COMET Phase-I will conduct a world-leading measurement of  $\mu-e$  conversion using the CyDet detector located inside a 1 T solenoid magnet surrounding the muon stopping target. This cylindrical geometry is necessary, since the curved electron transport solenoid will not be deployed in Phase-I and thus a planar type detector such as the StrECAL detector would suffer from backgrounds caused by beam-related particles.

*Other searches* In contrast to COMET Phase-II, the CyDet detector surrounds the muon stopping target directly in Phase-I, and can observe both positive and negative particles from the muon stopping target. This allows for a search for the lepton-number-violating process  $\mu^-N \rightarrow e^+N'$  ( $\mu^-e^+$  conversion) concurrently with the  $\mu^-N \rightarrow e^-N$  search. The anticipated experimental sensitivity for  $\mu^-e^+$  conversion could be similar to  $\mu^-N \rightarrow e^-N$  conversion, although a detailed estimation has not yet been performed. In addition, the cylindrical drift chamber will have a relatively large

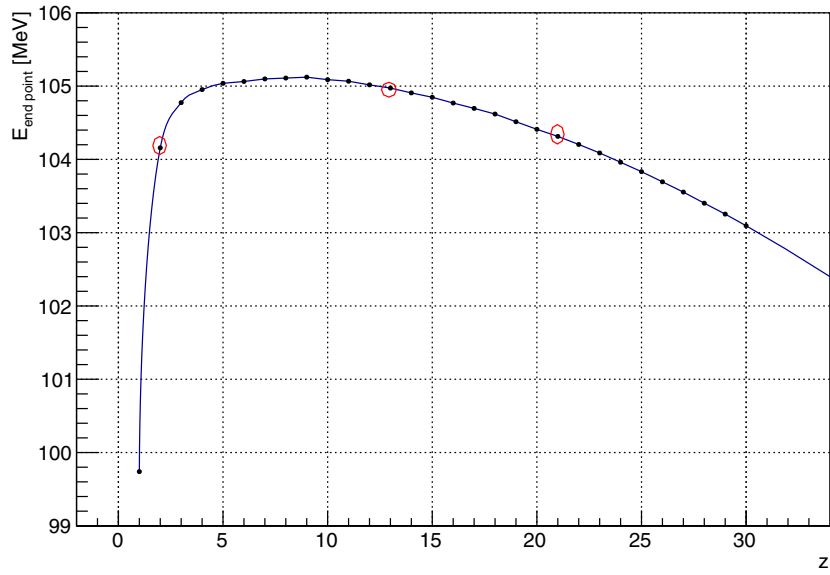


**Fig. 12.** DIO endpoint energy as a function of atomic number. The red circles highlight the atomic numbers corresponding to He, Al, and Ti (from left to right).

geometrical coverage, and thereby a coincidence measurement with a large solid angle is achievable. This allows a search for  $\mu^- e^- \rightarrow e^- e^-$  conversion in a muonic atom, which is an as-yet unmeasured process. Using a lower-intensity beam,  $< 10^7$  muon/s, a measurement of  $\mu^- e^- \rightarrow e^- e^-$  could be carried out with the CyDet detector.

### 3.4. Backgrounds

While the signal of  $\mu^- N \rightarrow e^- N$  is 105 MeV monoenergetic electron, there are several potential sources of electron background events in the energy region around 100 MeV, which can be grouped into three categories as follows: intrinsic physics backgrounds, which come from muons stopped in the target; beam-related backgrounds, which are caused by both muons and other particles in the muon beam; other miscellaneous backgrounds due to cosmic rays, fake tracking events etc.

*Intrinsic physics backgrounds* The major intrinsic physics background is muon decay in orbit (DIO) in the muonic atom. For this the  $e^-$  endpoint energy can extend to the energy of the  $\mu-e$  conversion signal when the kinematics corresponds to the limit of producing neutrinos at rest and with the system recoiling against the nucleus. The DIO endpoint energy depends on the element as shown in Fig. 12. Hence with an aluminum stopping target it is important to avoid materials whose DIO endpoint energy is higher than aluminum, i.e., materials from  $Z = 5$  to  $Z = 12$ , such as carbon and nitrogen. However, helium ( $Z = 2$ ) can be used.

The energy distribution of DIO falls steeply toward its endpoint as the fifth power of  $(E_{\mu e} - E_e)$ , where  $E_{\mu e}$  and  $E_e$  are the energy of the signal electron and that of DIO electrons, respectively [49–52]. The momentum resolution of the  $e^-$  detector is crucial to eliminate this background; for a resolution better than 0.2%, the contribution from DIO occurs at a level below  $10^{-16}$ .

Another prominent background process is radiative muon capture (RMC), given by

$$\mu^- + N(A, Z) \rightarrow \nu_\mu + N(A, Z - 1) + \gamma, \quad (14)$$

followed by internal and/or external asymmetric  $e^+e^-$  conversion of the photon ( $\gamma \rightarrow e^+e^-$ ). The kinematic endpoint ( $E_{\text{RMC}}^{\text{end}}$ ) of radiative muon capture is given by

$$E_{\text{RMC}}^{\text{end}} \sim m_\mu - B_\mu - \Delta_{Z-1}, \quad (15)$$

where  $\Delta_{Z-1}$  is the difference in nuclear binding energy of the two nuclei. Other intrinsic physics backgrounds could result from particle emission (such as protons and neutrons) after nuclear muon capture.

*Beam-related backgrounds* Beam-related background events may originate from muons, pions, or electrons in the beam. Muon decays in flight may create electrons in the energy range of 100 MeV if the muon momentum is greater than 75 MeV/c. Pions in the beam may also produce background events by radiative pion capture (RPC),

$$\pi^- + N(A, Z) \rightarrow N(A, Z-1) + \gamma, \quad (16)$$

followed by internal and external asymmetric  $e^+e^-$  conversion. There are also electrons arising directly in the secondary beam from the production target. To eliminate the backgrounds from pions and electrons, the purity of the beam (after transport) is very important.

*Other backgrounds* Cosmic-ray backgrounds must be eliminated by shielding, and detecting and vetoing the signals.

#### 4. Producing the muon beam

COMET requires negatively charged low-energy muons that can be easily stopped in a thin target to efficiently produce muonic atoms. Muons of appropriate momentum originate from the decay of low-energy pions produced in the backward direction by an incident pulsed proton beam from the J-PARC main ring onto a carbon target in the Nuclear and Experimental Hall. The beam must be pulsed as the lifetime of the muonic atom is a critical factor for isolating the signal. High-energy pions must also be eliminated as they can potentially cause background events.

The Phase-I beam line consists of a section for pion production and capture (pion-capture section), a section of muon transport (muon-transport section) and a bridging section from the muon beam line to the detector (bridge section). At the “downstream” end of the muon beam line is the aluminum target in the detector solenoid (DS). A schematic layout of the COMET Phase-I muon beam line is shown in Fig. 11 and the top figure of Fig. 18.

##### 4.1. The proton beam

The proton beam pulse width must be much less than the gap between pulses and significantly shorter than the lifetime of a muonic atom in aluminum, which is 864 ns. It is critical that an extremely high extinction rate, better than  $10^{-10}$ , between pulses be achieved. A proton beam of 8 GeV is employed with pulses of 100 ns duration, separated by at least 1.17  $\mu$ s. The beam energy is chosen to be 8 GeV, which is sufficiently high to produce an adequate number of muons but low enough to minimize antiproton production, which could lead to unwelcome population of particles in the signal time window.

In the J-PARC linac, a chopper with a very fast rise time (10 ns) is required to ensure that the rapid cycling synchrotron (RCS) can be filled with high efficiency and with the appropriate gaps

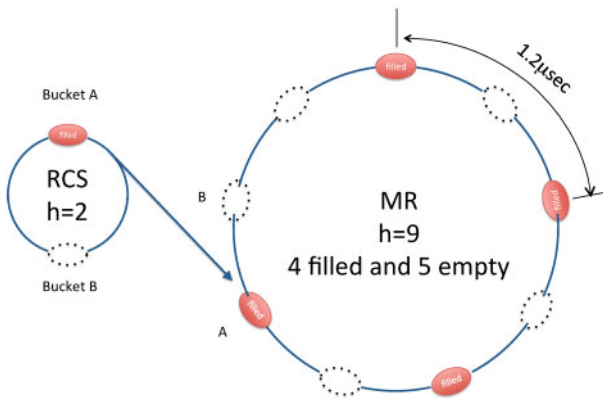


**Fig. 13.** The COMET bunch structure in the RCS and MR where four buckets are filled producing 100 ns proton bunches separated by at least  $1.17 \mu\text{s}$ .

between bunches. Inefficiencies could result in stray protons between the bunches and this needs to be minimized in order to avoid placing unachievable demands on the extinction system. The RCS will accept 400 MeV protons from the linac and accelerate them to 3 GeV. Four sets of acceleration are performed in the RCS with two bunches for each main ring (MR) acceleration cycle.

A  $1.17 \mu\text{s}$  pulsed beam structure is achieved by filling only four out of the nine MR buckets for MR operation at a harmonic number of nine. The four filled buckets are distributed around the ring in such a way that an empty bucket exists between the filled buckets<sup>3</sup>. A schematic showing the four-bucket structure is presented in Fig. 13.

Beam injection from the RCS into the MR using kicker magnets is a critical aspect for COMET due to the inter-bunch extinction requirements. A dedicated injection method, “single bunch kicking”, is realized by shifting the injection kicker excitation timing by 600 ns such that any particles remaining in empty buckets are not injected into the MR. A preliminary test in 2012 showed this to be effective at improving the extinction significantly and that the extinction level could be maintained through acceleration and extraction if the RF acceleration voltage was raised above its nominal value.

Slow extraction for COMET will be similar to that of the 30 GeV beam into the NP Hall, but needs to be modified so that the beam is extracted at the lower energy of 8 GeV, with the bunch structure retained. The major change for this “bunched slow extraction”, in contrast to the normal slow extraction, is that the RF voltages need to be maintained and not turned off during extraction. The required extinction factor can be achieved by increasing the RF voltage; however, there is a trade-off with the heat load on the cavity.

#### 4.1.1. Acceleration test

A series of proton beam acceleration tests was conducted in May 2014. Every second acceleration bucket of the MR was filled with 3 GeV protons from the RCS and accelerated to 8 GeV before extraction to the abort line. Protons corresponding to the 3.2 kW operation were accelerated to measure various beam parameters. The accelerator configuration was then optimized for COMET operation, in order to minimize beam loss.

<sup>3</sup> Also, a  $1.75 \mu\text{s}$  pulsed beam structure is possible by filling only three out of the nine MR buckets. In this case the three filled buckets are distributed around the ring in such a way that two empty buckets exist between filled buckets.

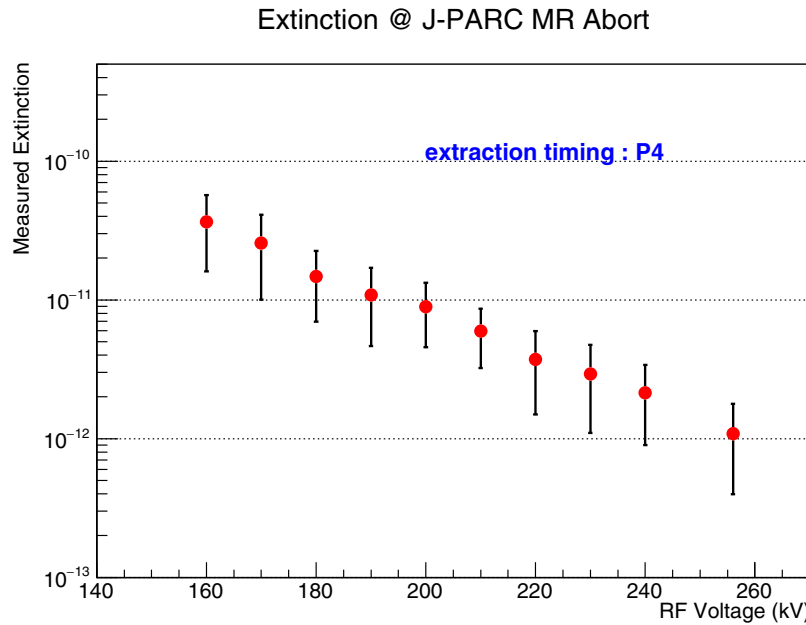


**Fig. 14.** Extinction levels measured at the MR abort line with a single bucket filled with the number of protons equivalent to that of 3.2 kW operation, as a function of the applied RF voltage during beam circulation after acceleration.

Systematic studies of the proton beam extinction factor were carried out with an extinction monitor installed in the MR abort line. The monitor is sensitive to single protons while covering a large dynamic range by using a plastic scintillator with four photomultipliers with different light attenuators. The beam extinction factor was studied by counting the number of protons scattered off a pulse after extracting whole beam bunches to the MR abort line with fast-extraction kickers. During the flat-top period, where beam extraction is usually conducted, the acceleration RF voltage was kept on to study the extinction factor dependence on the RF voltage.

The results of the extinction factor study are shown in Fig. 14. When the RF voltage was reduced less than 100 kV, it was observed that accelerated particles start to be scattered along the ring into the gaps between the bunches, resulting in deterioration of the extinction factor as large as  $10^{-10}$ . The extinction could be improved to as low as  $10^{-12}$  by applying an RF voltage of 255 kV. This is sufficiently small for the COMET experiment, so the voltage will be optimized for long-term operations in order to keep the RF cavity temperatures stable within the capabilities of the water cooling system.

#### 4.1.2. Proton beam line

The COMET experiment is being constructed in the NP Hall. In addition to the existing beam line (A-line) a new beam line is being built (B-line) with two branches, one to serve high-momentum (up to 30 GeV) experiments and the other for COMET (8 GeV). In the low-momentum running for COMET the entire beam is sent to the B-line. A schematic of the beam lines is shown in Fig. 15. To realize multiple operation modes, a Lambertson magnet followed by two septum magnets are deployed to provide the A/B-line branches. The proton beam line will be common for both COMET Phase-I and Phase-II.

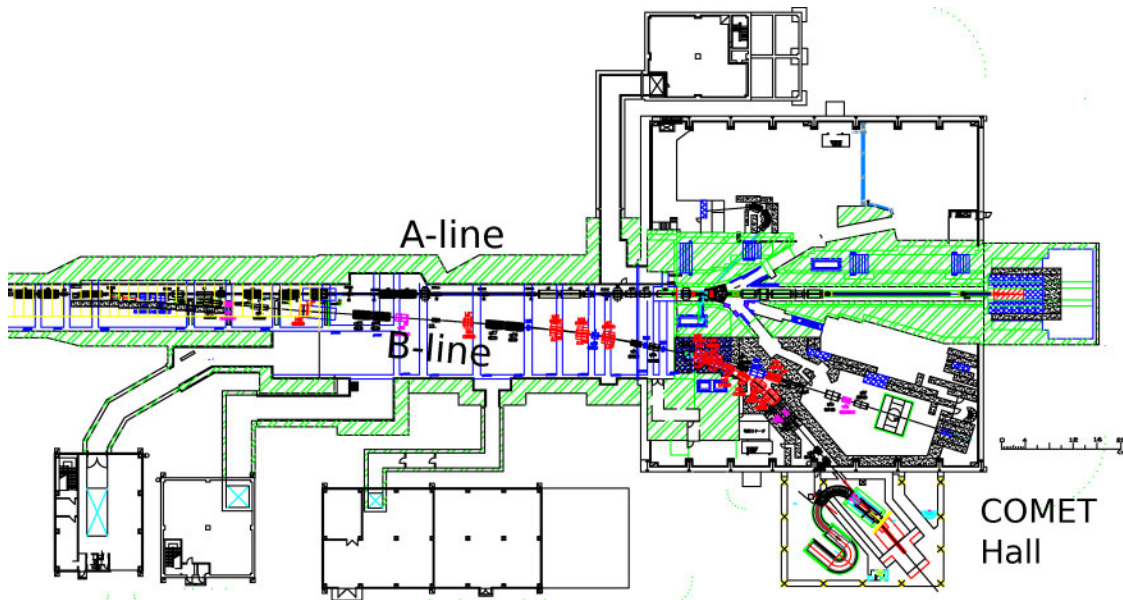


**Fig. 15.** The A and B-lines from the MR into the NP Hall. A schematic of the COMET experiment is shown in the bottom right.

The proton beam dump is designed to fulfill radiation safety requirements and this is evaluated using a PHITS [53] simulation. The resulting size of the required iron dump is 4 m wide and 5 m deep.

Beam profile monitors will be installed at several locations along the beam line including: downstream of the A/B-line branch; the boundary of the switch yard (the tunnel between the MR and the NP Hall); and the NP Hall, as well as upstream of the COMET building entrance. The same technology, RGIPM (residual gas ionization profile monitor) will be used as for the A-line beam monitors. In addition to the RGIPMs, an RGICM (residual gas ionization current monitor) will be installed near the COMET building entrance for beam intensity monitoring. The RGICM uses similar technology to the RGIPM, but precisely measures the current of ionization electrons, which is proportional to the beam intensity.

A diamond detector with a fast response and high sensitivity in a high-radiation environment will be employed for measuring the proton beam extinction factor and beam profile [54].

The beam optics of the proton beam line have been optimized by a TRANSPORT simulation. The  $3\sigma$  beam emittance at the extraction point used in the simulation is  $1.7 \pi \text{ mm mrad}$  in the horizontal direction and  $10.6 \pi \text{ mm mrad}$  in the vertical direction, which is based on the measurement of the beam profile in the switch yard after the beam extraction from the MR.

Beam loss due to interaction of the beam halo through the proton beam line is evaluated to be 0.003% using a TURTLE simulation.

#### 4.2. Pion production at the primary target

The proton target will be installed within the bore of the capture solenoid and designed to maximize the capture of low-energy negative pions produced in the backward direction. Both the target station and muon-capture solenoid region will be designed for the Phase-II beam power of 56 kW since, once constructed and exposed to the beam, the target station infrastructure will be activated and cannot be

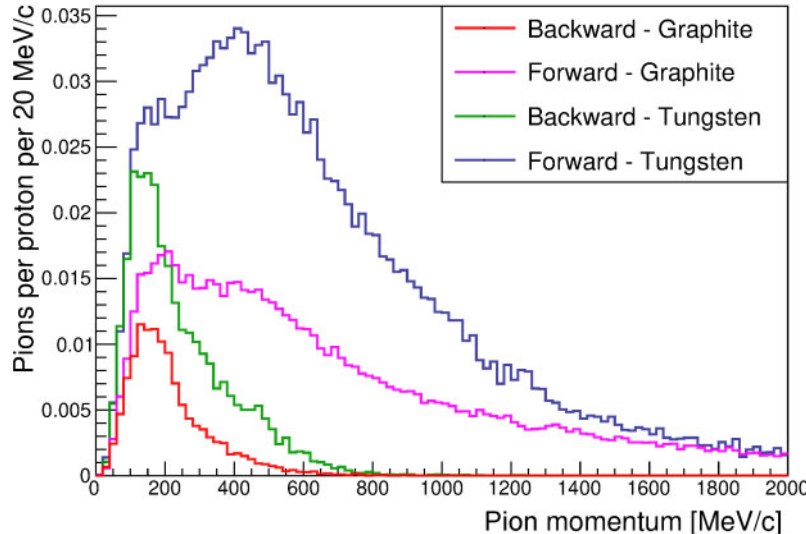


**Fig. 16.** Momentum distribution of pions exiting in the forward and backward regions of tungsten and graphite targets bombarded by an 8 GeV proton beam. The spectra are generated using Geant4 using the QGSP-BERT hadronization model.

modified. However, the target itself will be replaced between the two phases, and the target station will be designed with remote handling capability to allow for this.

While pion production is maximized with a high-Z material, it is proposed to use a graphite target for Phase-I. This will minimize the activation of the target station and heat shield, which will significantly ease the necessary upgrades for Phase-II operation where a tungsten target will be employed.

The Phase-I beam power of 3.2 kW will deposit a heat load of approximately 100 W in the graphite target material. This can easily be radiated to the solenoid shield. The target support system to accurately position the target within the solenoid inner shield will have a low-mass design.

Pion production yields from protons incident on graphite and tungsten targets in the backward and forward regions with respect to the proton beam direction are presented in Fig. 16.

Figure 17 shows the yields of pions and muons as a function of proton energy, calculated using Geant4. As seen in Fig. 17, the pion yield increases almost linearly with proton energy and therefore with proton beam power.

The choice of proton energy was determined by considering the pion production yield and backgrounds. In particular, backgrounds from antiproton production are important. The current choice of proton energy is 8 GeV, which is above the threshold energy for antiproton production, 6.56 GeV.

#### 4.3. Pion capture

The pions are captured using a high-strength solenoidal magnetic field giving a large solid angle acceptance. Figure 18 shows the layout of the pion-capture system, which consists of the pion production target, high-field solenoid magnets for pion capture, and a radiation shield. Pions emitted into the backward hemisphere with a transverse momentum less than 100 MeV/c are captured by using a solenoid magnet of 5 T, and inner bore of 30 cm. This gives adequate acceptance for the parent pions of muons with momentum below 75 MeV/c.

The predicted yields 3 m backwards from the proton target from different hadron production simulations were obtained by using the Geant4 [55] and MARS15 [56] programs. From the result

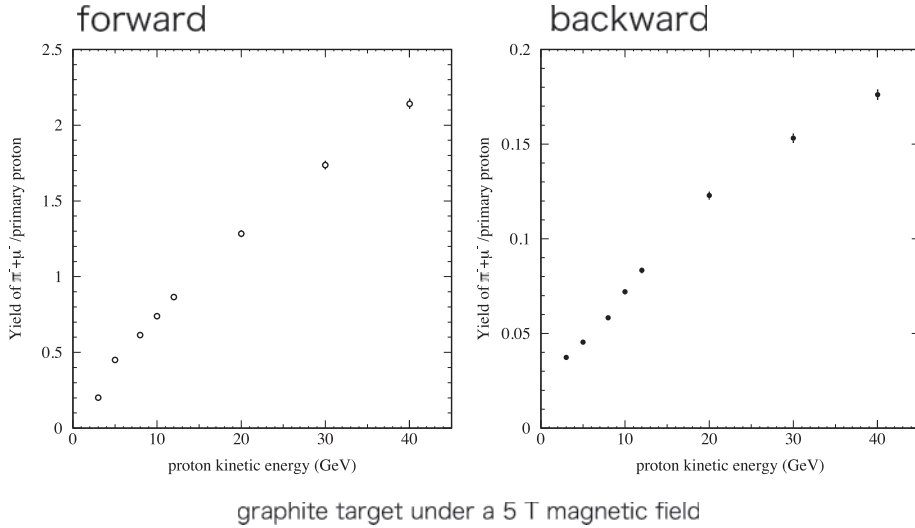


**Fig. 17.** Yields per proton of forward pions and muons, left, and backward pions and muons, right, from a graphite target in a magnetic field of 5 T, as a function of proton energy.

**Table 2.** Comparison of the  $\pi^-$  and  $\mu^-$  yields 3 m meters backwards from the proton target for different hadron production codes.

Models	Simulator	$N(\pi^- + \mu^-)/p$ at 3 m
CEM	MARS	$0.061 \pm 0.001$
CEM/LAQGSM	MARS	$0.138 \pm 0.001$
LAQGSM	MARS	$0.144 \pm 0.001$
LAQGSM	Geant	$0.1322 \pm 0.0007$
QGSP_BERT	Geant	$0.0511 \pm 0.0002$
QGSP_BIC	Geant	$0.1278 \pm 0.0005$
FTFP_BERT	Geant	$0.0440 \pm 0.0002$

shown in Table 2, it was found that the pion yields are different up to three times between the hadron production models. The QGSP\_BERT and FTFP\_BERT hadron production models have the lowest yield and so the QGSP\_BERT model has been used to conservatively estimate and optimize the muon beam.

The captured pions have a broad directional distribution. In order to increase the acceptance of the muon beam line it is desirable to make them more parallel to the beam axis by decreasing the magnetic field adiabatically. Under a solenoidal magnetic field, the product of the radius of curvature,  $R$ , and the transverse momentum,  $p_T$ , is an invariant:

$$p_T \times R \propto \frac{p_T^2}{B} = \text{constant}, \quad (17)$$

where  $B$  is the magnitude of the magnetic field. Therefore, if the magnetic field decreases gradually,  $p_T$  also decreases, yielding a more parallel beam. This is the principle of the adiabatic transition. Quantitatively, when the magnetic field is reduced by a factor of two,  $p_T$  decreases by a factor of  $\sqrt{2}$ . However, this causes the radius of curvature to increase by a factor of  $\sqrt{2}$  and hence the inner radius of the magnet in the pion decay section has to be  $\sqrt{2}$  times that of the pion-capture solenoid. Thus the pion beam can be made more parallel at the cost of an increased beam size. In the COMET Phase-I

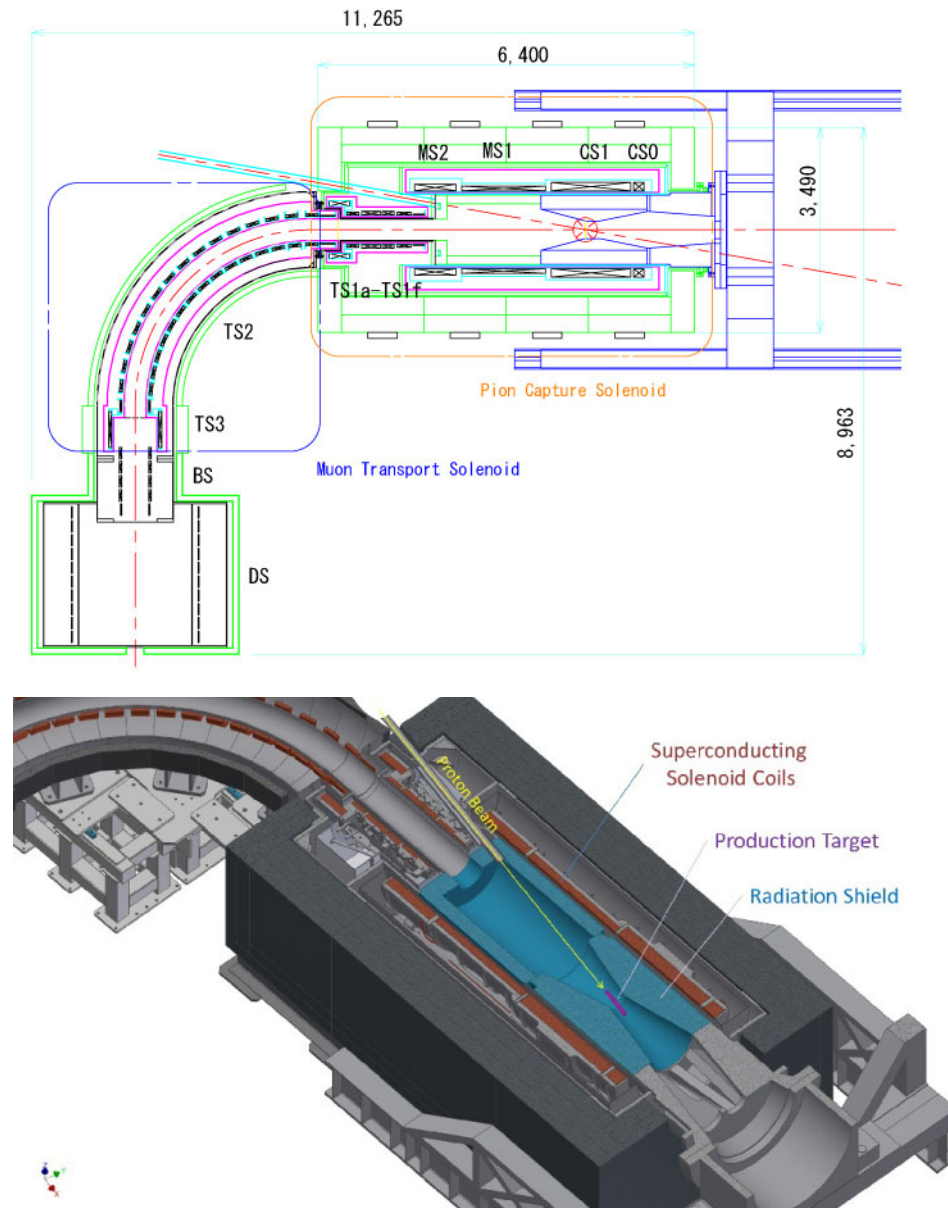


**Fig. 18.** (Top) Layout of the COMET Phase-I solenoid system, which consists of the pion-capture solenoid (orange box), muon-transport solenoid (blue box), beam dump (right part of pion-capture solenoid), and detector solenoid (bottom part of muon-transport solenoid). The pion production target (proton target) is located at the center of the pion-capture solenoid, marked by a red circle. The slanted direction of the pion production target to the beam line is shown by the red solid-dashed line. CS: capture solenoid, MS: matching solenoid, TS: transport solenoid, BS: bridge solenoid, and DS: detector solenoid. (Bottom) Layout of the pion-capture solenoid system in 3D view.

solenoid system, a magnetic field of 5 T in the pion-capture solenoid (CS) gradually decreases to 3 T at the matching solenoid (MS).

#### 4.4. Muon beam transport

The muon beam transport consists of curved and straight superconducting solenoid magnets of 3 T and  $\sim 7.6$  m length. The requirements are:

- the muon transport should be long enough for pions to decay to muons;
- the muon transport should have a high transport efficiency for muons with a momentum of  $\sim 40$  MeV/c; and
- the muon transport should select muons with low momentum and eliminate muons of high momentum ( $p_\mu > 75$  MeV/c) to avoid backgrounds from muon decays in flight.

The optimal muon momentum is  $\sim 40$  MeV/c. Muons with higher momentum are less likely to be stopped and give rise to backgrounds in the signal region from decays in flight. Positive muons are another potential source of background. Curved solenoid transport is used to minimize these.

A charged particle in a solenoidal field follows a helical trajectory and, in a curved solenoid, the central axis of this trajectory drifts in the direction perpendicular to the plane of curvature. The magnitude of this drift,  $D$ , is given by

$$D = \frac{1}{qB} \left( \frac{s}{R} \right) \frac{p_L^2 + \frac{1}{2}p_T^2}{p_L}, \quad (18)$$

$$= \frac{1}{qB} \left( \frac{s}{R} \right) \frac{p}{2} \left( \cos \theta + \frac{1}{\cos \theta} \right), \quad (19)$$

where  $q$  is the electric charge of the particle (with its sign),  $B$  is the magnetic field at the axis, and  $s$  and  $R$  are the path length and the radius of curvature of the curved solenoid, respectively. Here,  $s/R$  ( $= \theta_{\text{bend}}$ ) is the total bending angle of the solenoid, hence  $D$  is proportional to  $\theta_{\text{bend}}$ .  $p_L$  and  $p_T$  are longitudinal and transverse momenta so  $\theta$  is the pitch angle of the helical trajectory. Particles with opposite signs drift in opposite directions and this is used for charge and momentum selection with a collimator placed after the curved solenoid.

To keep the center of the helical trajectories of the 40 MeV/c muons in the bending plane, a compensating dipole field parallel to the drift direction must be applied.

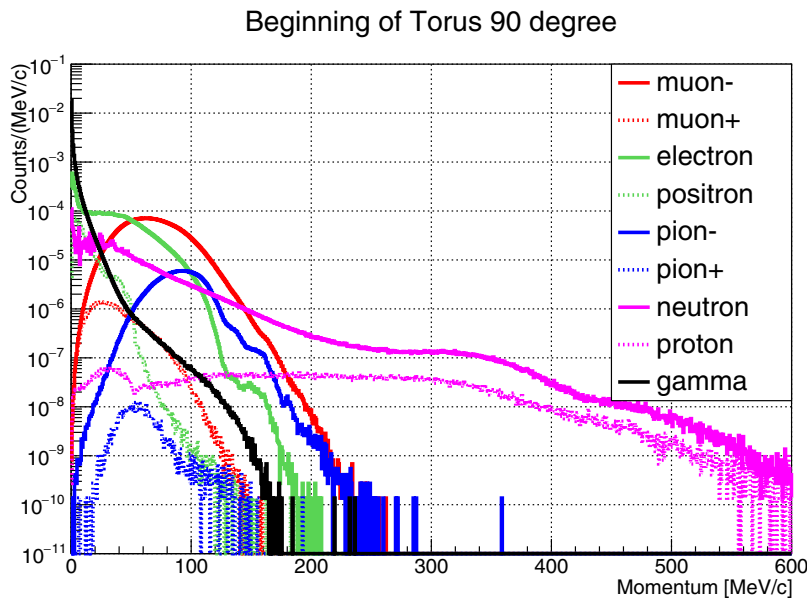
The COMET Phase-I beam line uses one curved solenoid with a bending angle of 90° with a compensating dipole field of  $\sim 0.05$  T. The collimator system is designed to remove particles traveling 8.5 cm above or 10 cm below the beam height and will be realized by installing two plates of stainless steel at the exit of the muon-transport system. To separate the muon stopping target region, filled with helium, from the muon beam line in vacuum, a vacuum window of 500  $\mu$ m titanium will be installed at the exit of the curved solenoid. The muon-transport section and the detector solenoid (DS) are connected by the beam bridge solenoid (BS), where the magnetic field changes from 3 T to 1 T.

#### 4.4.1. Muon beam yields

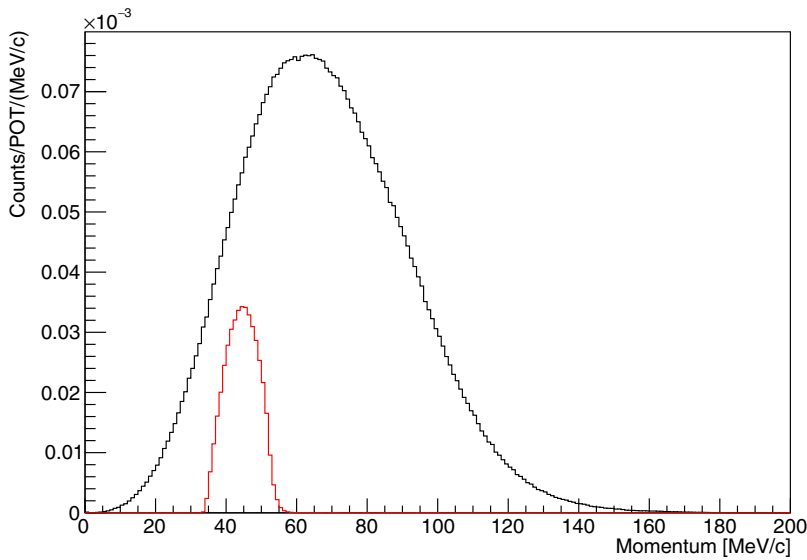
The momentum distribution of various beam particles at the exit of the first 90° curved solenoid with the muon beam collimator is given in Fig. 19.

Figure 20 shows the distribution of the muon momenta at the end of the muon-transport solenoid. The solid black line shows those reaching the end of the muon-transport solenoid including the muon beam collimator, and the red line those stopping in the target. The low-energy cut-off of the red line at about 35 MeV/c is due to absorption in the titanium safety windows.

Estimates using the QGSP\_BERT model of the number of muons and pions per proton after the muon-transport section and on the muon stopping target are summarized in Table 3. The number of muons stopping in the muon stopping target is about  $4.7 \times 10^{-4}$  per proton, and so with a 0.4  $\mu$ A proton beam, the yield of stopped muons is about  $1.2 \times 10^9$  per second.



**Fig. 19.** Momentum distributions of various beam particles at the exit of the first 90° curved solenoid, using a graphite proton target.



**Fig. 20.** Distributions of momentum at the end of the muon beam transport solenoid. Black and red solid lines are those arriving at the end of the muon-transport solenoid including the muon beam collimator, and stopping in the muon stopping target.

**Table 3.** Muon and pion yields per proton in front of the bridge solenoid (BS), after the BS, and stopped in the muon stopping target.

Yield (per proton):	After muon-transport section	Stopped in muon target
Muons	$5.0 \times 10^{-3}$	$4.7 \times 10^{-4}$
Pions	$3.5 \times 10^{-4}$	$3.0 \times 10^{-6}$

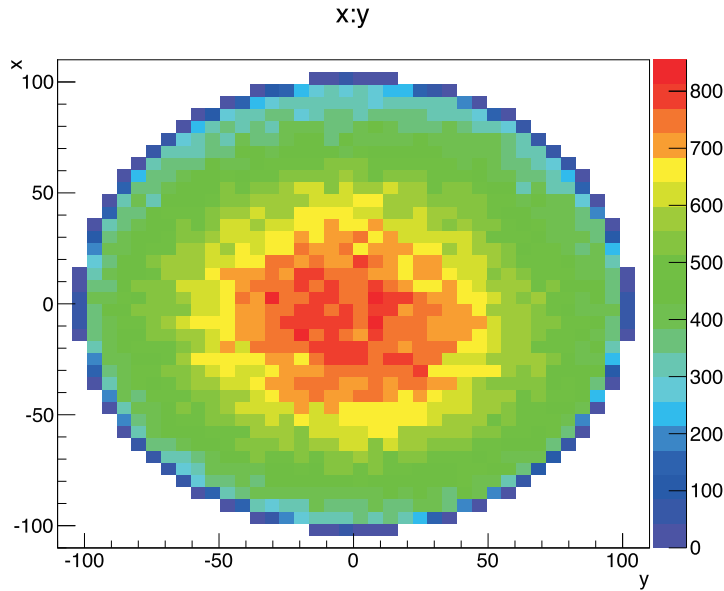


**Fig. 21.** The distribution of stopped muons stopped projected on the  $x$  and  $y$  axes. The  $z$  axis (color codes) shows the number of stopped muons in arbitrary units.

#### 4.5. Muon stopping target

The muon stopping target is placed in the center of the DS and designed to maximize the muon stopping efficiency and acceptance for the  $\mu-e$  conversion electrons. The design must also minimize the energy loss of the conversion electrons as this increases their momentum spread.

To eliminate beam-related background events arising from prompt beam particles the measurement window will only open approximately  $0.7 \mu\text{s}$  after the primary proton pulse. High- $Z$  target materials are not appropriate for the stopping target since the muonic atom lifetime decreases with increasing  $Z$ . Aluminum ( $Z = 13$ ) with a muonic atom lifetime of 864 ns is the preferred target over titanium ( $Z = 22$ ) and lead ( $Z = 82$ ), which have muonic atom lifetimes of 330 ns and 74 ns respectively.

The configuration and dimensions of the muon stopping target have been optimized [57] for maximum muon stopping efficiency and for minimal backgrounds and energy spread of the electrons.

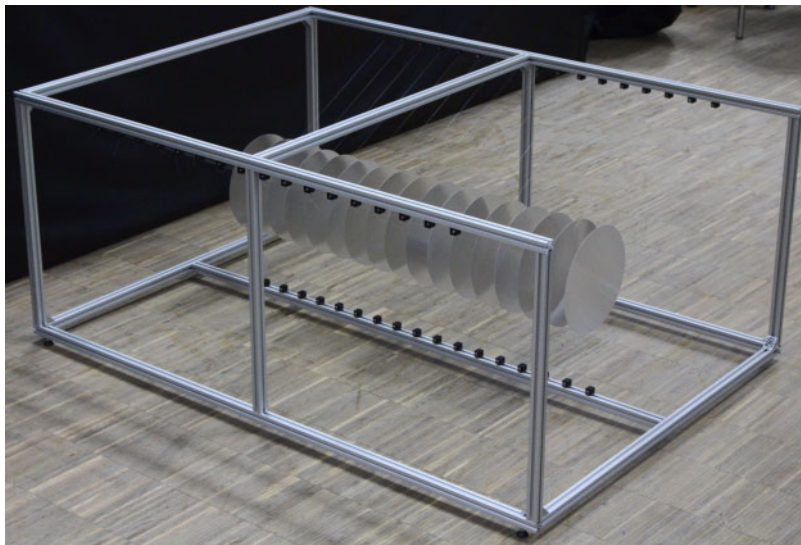
The current design consists of 17 aluminum disks, 100 mm in radius and  $200 \mu\text{m}$  in thickness, with 50 mm spacings.

Figure 21 shows the distribution of the number of muons stopped in each of the 17 disks of the muon stopping target. In optimizing the design, one must take into consideration that the total number of stopped muons increases with the number of target disks, but that this has a cost in the form of additional energy loss of the electron in the target. From Fig. 21, the proposed target size would give reasonable radial coverage.

A mock-up muon stopping target for testing is shown in Fig. 22. Each aluminum disk is supported by three spokes. The spokes are connected to the ring structure that is placed inside the inner wall of the cylindrical drift chamber (CyDet). The spokes are made of aluminum or a high- $Z$  material to avoid backgrounds from muons stopped in the spokes.

##### 4.5.1. X-ray monitor

When the muonic atoms are formed on the muon stopping target, a cascade of X-rays is emitted as the muons drop down to the  $1s$  state. This can be used to tag and count the formation of these muonic



**Fig. 22.** A mock-up muon stopping target for testing.

atoms. In turn, this can help measure the number of muon captures that forms the denominator for the  $\mu-e$  conversion rate that is the ultimate output of this experiment.

The observation of such muonic X-rays from aluminum has been achieved in the past in cosmic rays [58], and, for COMET, a design based on the principles of these earlier measurements is being studied at this time. This involves a high-efficiency germanium detector combined with a coincidence and anti-coincidence system.

## 5. CyDet: the cylindrical detector system

The cylindrical detector system (CyDet) is the main detector system for the  $\mu-e$  conversion search in COMET Phase-I. It consists of a cylindrical drift chamber (CDC) and a cylindrical trigger hodoscope (CTH). Figure 23 shows a schematic layout of the CyDet. It is located after the BS in the muon-transport section, and installed inside the warm bore of a large 1 T superconducting detector solenoid (DS) and around the stopping target.

This detector has been adopted for Phase-I as there is no downstream curved solenoid electron transport and so most beam particles that do not stop in the muon stopping target will go downstream and escape from the detector region without leaving any hits in the detector system.

A key feature of COMET is to use a pulsed beam that allows for the elimination of prompt beam backgrounds by looking only at tracks that arrive several hundred nanoseconds after the prompt beam flash. Therefore, any momentum-tracking devices must be able to withstand the large flux of charged particles during the burst of “beam flash” particles.

### 5.1. Cylindrical drift chamber

The detector is designed to avoid high hit rates due to beam particles, DIO electrons, and low-energy protons emitted after the nuclear capture of muons. Among the small fraction of particles that eventually enter the CDC and leave hits, DIO electrons and low-energy protons dominate. The protons are easily identified, because the energy deposits in the CDC cells are about 100 times larger than those of similar-momentum electrons. To achieve the required sensitivity for Phase-I, the momentum resolution must be about  $200 \text{ keV}/c$  for  $105 \text{ MeV}$  electrons. At this energy, the momentum

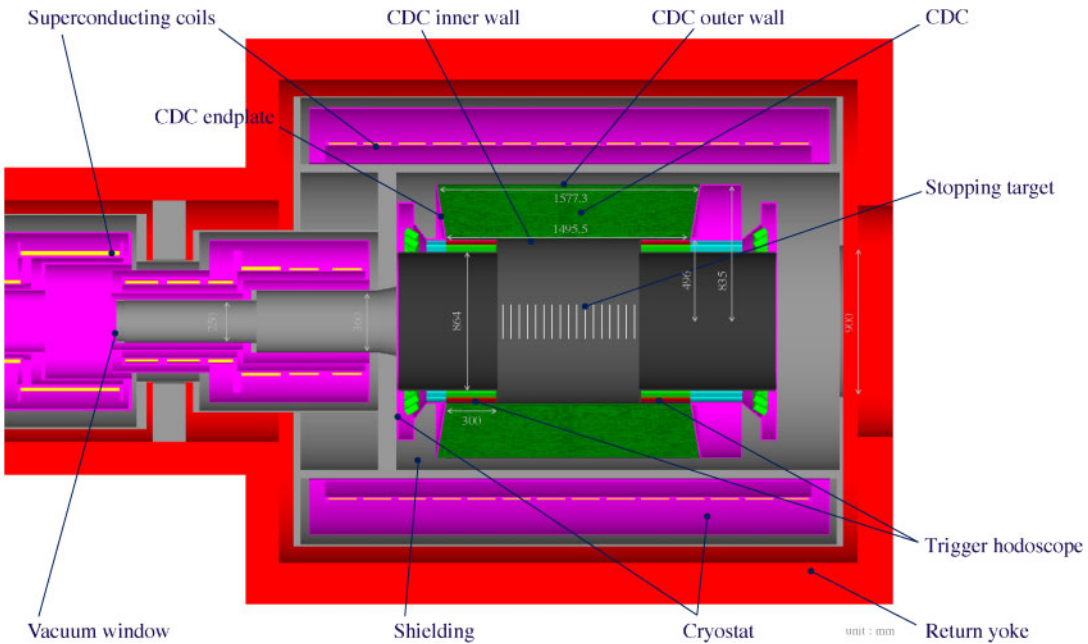


**Fig. 23.** Schematic layout of the CyDet detector.

resolution is dominated by multiple scattering. Consequently, the CDC must be a low-mass detector and this dictates the construction and the choices of cell configuration, wires, and the gas mixture.

#### 5.1.1. Layer and cell configuration

The CDC is arranged in 20 concentric sense layers with alternating positive and negative stereo angles. Cylindrical drift chambers with only stereo layers have been constructed in the past, such as the KLOE drift chamber [59]. The 1st and 20th sense layers have a lower high voltage (HV) and act as guard layers to remove the space charge that would otherwise accumulate.

Each cell has one sense wire surrounded by an almost-square grid of field wires. The ratio of the total number of field wires to sense wires is 3:1. The cell size is 16.8 mm wide and 16.0 mm high and nearly constant over the entire CDC region. Square cells are well suited to the low-momentum tracks that can enter the drift cells at large angles with respect to the radial direction. The stereo angle  $\varepsilon$  is set to 64–75 mrad to achieve a longitudinal spatial resolution  $\sigma_z$  of about 3 mm. In total there are 4986 sense wires and 14 562 field wires.

The field wires are made of aluminum in order to reduce multiple scattering. Whilst it would be desirable to use  $\phi 80\ \mu\text{m}$  aluminum wires, the operation voltage for this case would then need to be below 1730 V to keep the electric field on the wire surface below 20 kV/cm, above which corona discharges and whisker growth can occur on the wires. However, tests with the CDC prototype have shown that 1730 V is not enough to obtain sufficient signal gain. Consequently,  $\phi 126\ \mu\text{m}$  wires are used, allowing operation with voltages of up to 1900 V, and simulations show that the change in the momentum resolution does not significantly affect the physics sensitivity. A tension of 80 g is applied to the field wires to match the gravitational sag of the sense wires.

The sense wires are made of gold-plated tungsten, 25  $\mu\text{m}$  in diameter, tensioned to 50 g. The deflection due to gravity is about 50  $\mu\text{m}$  at the center of the CDC. The total tension force on the endplates is 1.4 tonne.

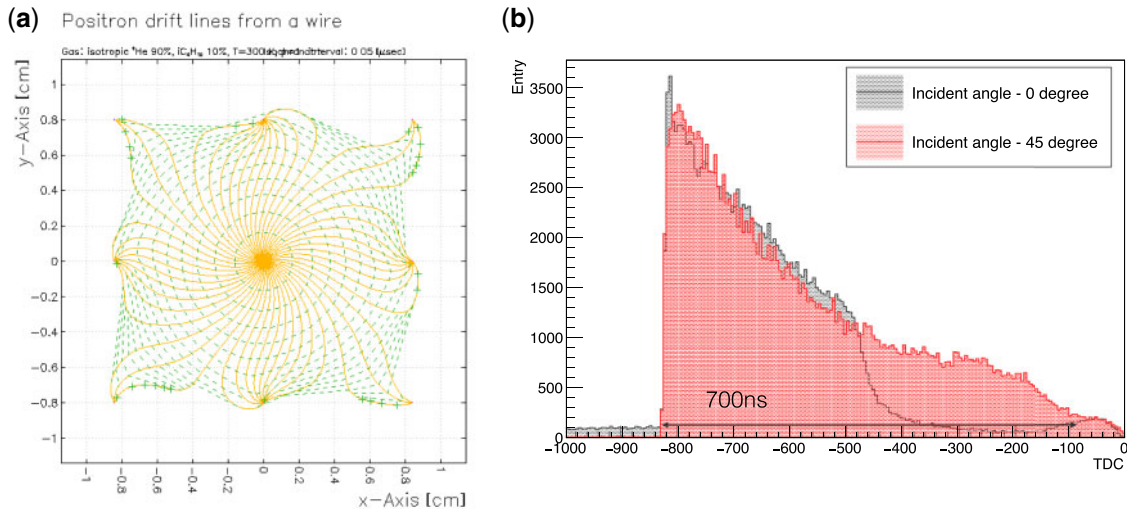


**Fig. 24.** (a) Garfield simulation of the drift lines for a CDC cell under a 1 T magnetic field, and (b) the drift time distribution for two incident angles from the fourth prototype. Gas composition is He:i-C<sub>4</sub>H<sub>10</sub> (90:10).

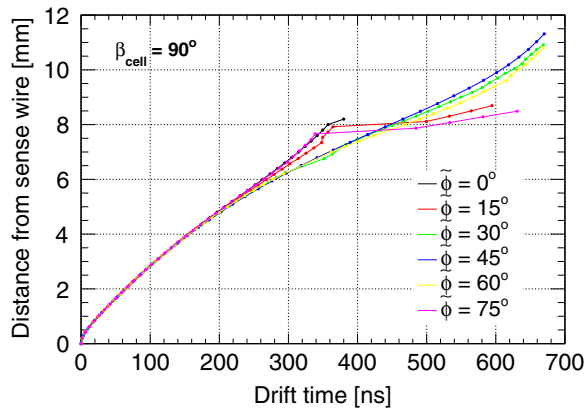


**Fig. 25.** Space-time correlations with different incident angles ( $\tilde{\phi}$ ) without magnetic field, calculated with a Garfield simulation.

The chamber gas is He:i-C<sub>4</sub>H<sub>10</sub> (90:10), which has a radiation length of about 1300 m. The field and sense wires reduce the average value of the radiation length of the CDC tracking volume to 507 m. An HV up to 1900 V is applied to the sense wires with the field wires at ground potential, giving an avalanche gain of approximately  $1-4 \times 10^4$ . Typical drift lines for a cell are shown in Fig. 24, calculated for this gas mixture.

The Garfield program has been used to study cell properties, including drift time isochrones, time-distance relationships, distortions, and gain variations. Typical drift time distributions are shown in Fig. 24(b). Space-time correlations with different incident angles are shown in Fig. 25.

### 5.1.2. Mechanical design

The main parameters of the CDC are summarized in Table 4. There are three main mechanical parts composing the CDC: the endplates, the inner wall, and the outer wall. The radii of the inner and outer walls are chosen to avoid DIO electrons with momentum less than 60 MeV/c from hitting the CDC and to fully cover the tracks of 105 MeV/c signal electrons. The walls are made from carbon-fiber-reinforced plastic (CFRP); the inner wall is 0.5 mm thick and the outer wall 5 mm. The inner and

**Table 4.** Main parameters of the CDC.

Inner wall	Length	1495.5 mm
	Radius	496.0–496.5 mm
	Thickness	0.5 mm
Outer wall	Length	1577.3 mm
	Radius	835.0–840.0 mm
	Thickness	5.0 mm
Number of sense layers	20 (including two guard layers)	
Sense wire	Material	Au-plated W
	Diameter	25 $\mu\text{m}$
	Number of wires	4986
	Tension	50 g
Field wire	Material	Al
	Diameter	126 $\mu\text{m}$
	Number of wires	14 562
	Tension	80 g
Gas	Mixture	He:i-C <sub>4</sub> H <sub>10</sub> (90:10)
	Volume	2084 L

outer walls have thin aluminum foils glued inside them to eliminate charge-up on the CFRP. Tapered aluminum endplates with 10 mm thickness are chosen for the endplates to adequately support a 1.4 tonne wire tension load.

The mechanical properties of the design have been calculated through finite element analysis using SolidWorks. The total wire tension load is calculated to be  $F_{\text{wire}} = 12\ 700 \text{ N/m}^2$  based on the parameters described in Table 4. The maximum deformation of the endplate is estimated to be as small as 1.1 mm for a tapered angle of 10°. The deformation was applied as pre-tension in advance of wire stringing, and then the pre-tension was released as the wires were strung to keep the constant deformation and sufficient wire tension.

### 5.1.3. Electronics

The Belle-II CDC readout electronics board (RECBE) [60] is used for the front-end readout of the CDC with appropriate modifications. Each board has 48 input channels, 6 ASD (amplifier shaper discriminator) ASIC chips [61], 6 ADCs, and an FPGA. Data is sent to the DAQ PC via an optical fiber cable. RJ45 connectors are used to download the firmware into the FPGA and for transmitting clock, trigger, and busy signals between the fast control and trigger (FCT) board described in Section 8.1.

Eight pre-production RECBE boards underwent burn-in tests in 2015. As a result of these tests and employing the Arrhenius model to predict how time-to-fail varies with temperature, the RECBE lifetime estimate is longer than 2.5 years for one board. The readout electronics are located on the CDC downstream endplate and the HV cables are connected on the upstream endplate. Production of all the readout boards (128 boards with spares) was completed by the IHEP group in China in 2015.

Figure 26 shows a block diagram of the COMET CDC readout implemented in the FPGA of RECBE. The main features are:

- the fast control block receives the reference clock, trigger (trigger number) from the FCT board and sends a busy signal to stop receiving triggers if the buffer is full;

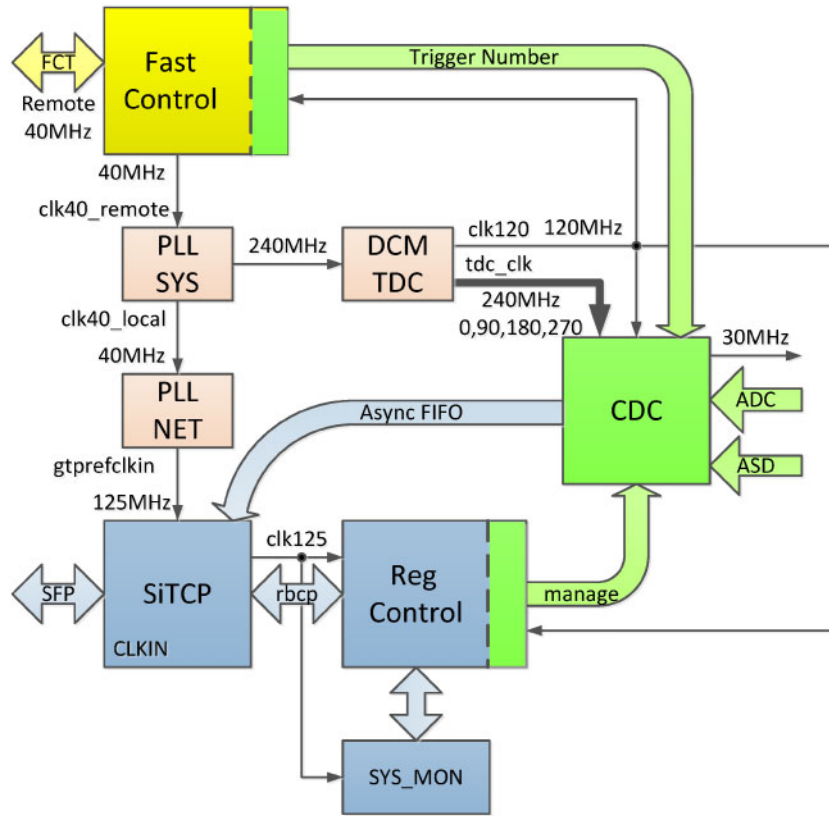


**Fig. 26.** Block diagram of the RECBE firmware. In yellow is the 40 MHz domain, which comes from the FCT board, in green is the 120/240 MHz domain, which manages the ADC and TDC, and in blue is the 125 MHz domain, which matches the data transfer rate of the Gigabit Ethernet.

- the **CDC** block arranges data of drift time and charge from the TDCs and ADCs;
- the **SiTCP** block is used to transmit the event data to the DAQ system via a Gigabit Ethernet fiber link;
- the **reg control** block is responsible for configuration and status;
- the **SYS MON** block is used for status monitoring, such as temperature and voltage.

The size of the ring buffer that stores the ADC and TDC data is 256 deep, corresponding to  $\sim 8.533 \mu\text{s}$ . Typically, the event window size for the **CDC** is 32 samples corresponding to  $\sim 1.067 \mu\text{s}$ , which makes the trigger latency  $\sim 7 \mu\text{s}$ . Hence typically, eight events can be stored in the buffer.

The front-end readout boards are installed near the detector region where the radiation level is high. The radiation effects, in particular from neutrons, on the FPGA hardware will be a severe problem. We have developed high-reliability firmware with auto-recovery schemes, and evaluated it with a neutron beam. In the test, soft error rates were measured and good performances of the schemes were demonstrated [62].

## 5.2. *CDC performance estimation and tests*

### 5.2.1. *CDC hit rates*

The **CDC** hit rates have been studied with Geant4 simulations. Potential sources causing noise hits are grouped into three categories:

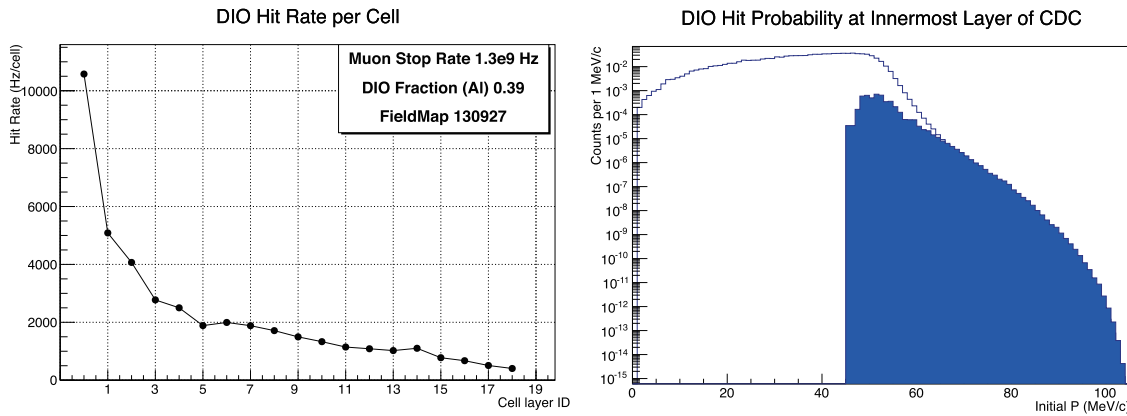


**Fig. 27.** (Left) DIO electron hit rate for each CDC cell layer. Note that a cell-layer ID of 0 means the guard layer. (Right) Momentum distribution of the DIO electrons. The blue histogram shows those of electron hits in the CDC.

- (1) muons and pions at the muon stopping target and its vicinity, which create secondary (or tertiary) particles in the CDC;
- (2) a prompt beam flash;
- (3) neutrons that are either in a beam, from the proton target, or the proton dump.

*Hit rate contribution from stopped muons and pions* The estimated hit rates of each CDC cell at different layers from DIO electrons from stopped muons are shown in Fig. 27 (left). The rate decreases quickly at deeper CDC layers, since the DIO momentum spectrum drops as a function of electron momentum, as shown in Fig. 27 (right). From Fig. 27 (left), the time-averaged rate for the innermost sense wire is at most 5 kHz/cell, yielding an instantaneous rate of about 15.6 kHz/cell allowing for the duty factor of the J-PARC MR proton beam cycle, which is about 3. This implies a hit occupancy for one bunch cycle of  $1.17 \mu\text{s}$  of about 1.8%.

Using the results from the AlCap<sup>4</sup> experiment at PSI, the time-averaged hit rate on a single cell from proton emission from muon capture is estimated to be 1.4 kHz. Other sources of hits following nuclear muon capture, such as bremsstrahlung photons, muonic X-rays, neutrons from nuclear muon capture, and  $\gamma$ -rays from the final state nucleus have also been considered. The magenta points and lines in Fig. 28 summarize the CDC occupancy caused by stopped muons that result in a total occupancy of between 7% and 10%.

The hit rate contribution from stopped pions is also summarized with the cyan points and lines in Fig. 28. Their contribution is small compared to the other categories.

*Hit rate contribution from beam flash* Although the beam flash is very short the associated CDC hits arrive over a period as a result of the drift time. The distribution of drift times could be different for different gas mixtures, as described in Sect. 5.1. The drift time distribution from the fourth prototype tests at SPring-8 are shown in Fig. 24(b). The maximum drift time, coming from the cell corners, is 700 ns and Fig. 29 shows the relation between prompt beam flashes, event timing in the time window of measurement, and the drift time of the hits. As the separation of the beam

<sup>4</sup> AlCap is a collaboration between COMET and Mu2e that measures the rate and spectrum of particles emitted from nuclear muon capture on aluminum [63].

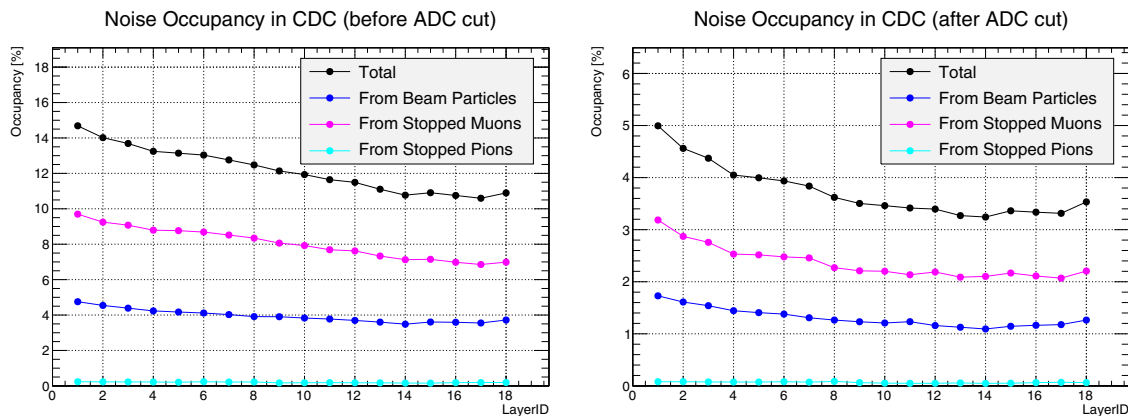


**Fig. 28.** CDC single hit occupancy as a function of the CDC layers for a gas mixture of He:i-C<sub>4</sub>H<sub>10</sub> (90:10). The left and right figures are respectively those before the energy deposit cut and after the cut, which selects hits with energy deposits smaller than 5 keV. The closed circles filled with blue, magenta, cyan, and black are respectively from beam particles, stopped muons, stopped pions, and total occupancy.

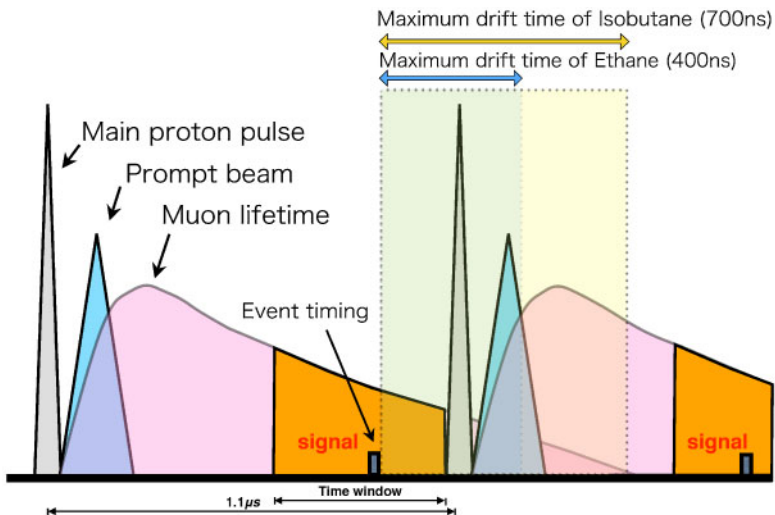


**Fig. 29.** Relation between prompt beam flash, event timing in the time window of measurement, and drift time of hits in a time period of two beam cycles.

pulses is 1170 ns the following beam flash will come within the drift time of 700 ns and therefore the CyDet detector must be able to accommodate the beam flash. The major sources creating noise hits are photon and neutron interactions, which depend strongly on the muon beam design, in particular the collimation. Radiation shielding to prevent photons hitting the CDC (in particular the endplates) is important. The total contribution from beam flash is estimated to lead to around 4% occupancy as shown in Fig. 28. In Fig. 30 a sample event display with beam flash is shown. The event in Fig. 30 occurs 1090 ns after the prompt beam timing, and therefore the time period for open hits covers the following beam bunch. It can be seen that noise hit rates are not too large.

**Hit rate contribution from ambient and beam neutrons** A fraction of the fast neutrons from the beam target will penetrate the endplates and inner and outer walls and degrade to a thermal spectrum. These have been simulated with both PHITS and Geant4, which indicate that, with paraffin shields

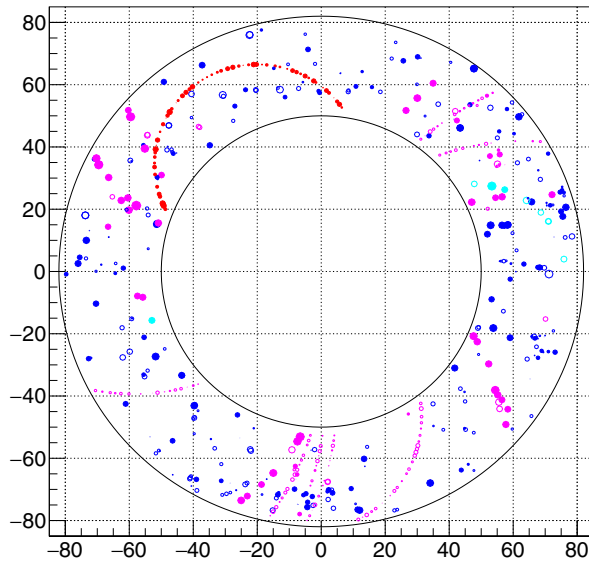


**Fig. 30.** Simulated CDC event display for a gas mixture of He:i-C<sub>4</sub>H<sub>10</sub> (90:10). This event occurs 1090 ns after the prompt beam flash. Hits in red, cyan, magenta, and blue are respectively from signal tracks, tracks from pion capture, tracks from muon capture, and other noise hits. The hits in open circles and closed circles are respectively those with energy greater and smaller than 5 keV.

installed along the beam line, the hit rate induced by ambient and beam neutrons can be made very small.

### 5.2.2. Charge measurement

Most noise hits are either associated with low-energy electrons or positrons created by photon conversion, electrons from DIO decays of muons, and protons created from nuclear muon capture. For the conversion electrons and positrons, typical energies are a few MeV and their helical trajectories will have a very small radius and are likely to stay in the same CDC cell for a long time. In some cases, when created at one of the endplates they may travel along the CDC and reach the other endplate. Therefore many of these noise hits will have a *large* charge in the hit cell. Low-momentum protons are heavily ionizing and so will also deposit a lot of energy in a CDC cell.

The CDC readout system is capable of measuring total charges with 30 MHz sampling. Figure 31 shows the total energy deposit for electron signals of  $\mu-e$  conversion and noise hits. Hence about 68% of the noise hits can be identified and removed by only retaining hits with an energy deposit smaller than 5 keV, while 99% of the signal hits will pass this selection. Figure 28 (right) shows the hit occupancy after this selection. The original hit occupancy of 12% would then be reduced to about 3.5%. This high-charge cut is carried out in the RECBE firmware as described in Section 5.1.3.

### 5.2.3. Prototype CDC tests

Four small-sized prototype chambers were constructed in order to examine the performance of the CDC; their specifications are summarized in Table 5.

The first prototype chamber was constructed in order to examine the performance in a tentative design. The second and third prototypes are simple box-type chambers with sense wire diameters of 25 and 30  $\mu\text{m}$ , respectively. They were constructed for the beam test at ELPH, Tohoku University in December 2014. The chambers were irradiated by electron beams for three gas mixtures as shown

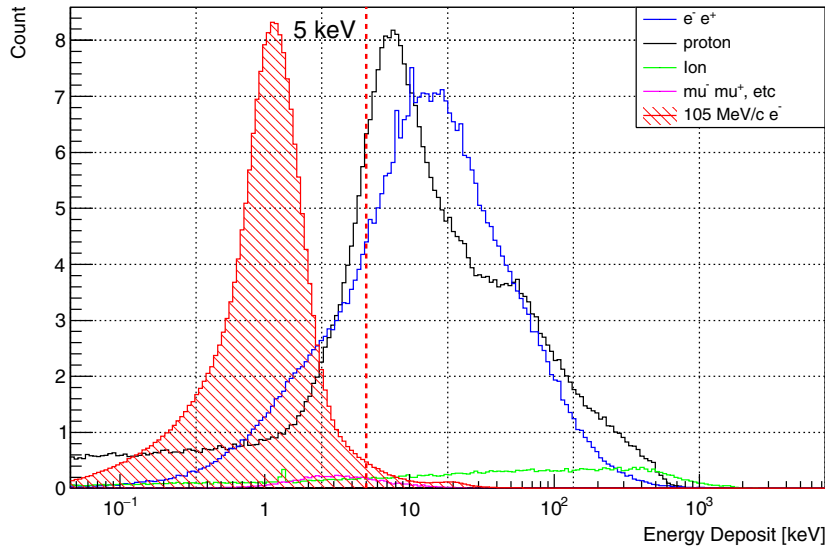


**Fig. 31.** Total energy deposits per cell for signal electrons and noise hits. The signal electrons are shown in the red shaded histogram; noise hits from various sources are shown in other histograms. A 5 keV threshold line (as used in the event displays) is also shown.

**Table 5.** Specifications of the prototype chambers.

Prototype	1	2	3	4
Sense wire $\phi$ [ $\mu\text{m}$ ]	30	25	30	25
Field wire $\phi$ [ $\mu\text{m}$ ]	126	80	80	126
# of sense layers	11	5	5	9
# of readout channels	199	27	27	87
Stereo angle [mrad]	25	70	70	66
Wire length [mm]	600	200	200	600
Angle coverage [deg]	30	8	8	15

in Fig. 32 (left). Figure 33 shows the hit efficiency as a function of the applied high voltage for each gas mixture. This confirmed that the operation voltage should be higher than 1800 V for He:i-C<sub>4</sub>H<sub>10</sub> (90:10) to achieve sufficient efficiency and led to the decision to use the 126  $\mu\text{m}$  diameter field wires<sup>5</sup>.

The fourth (final) prototype chamber was constructed after the mechanical specification of the CDC had been determined. It is a partial copy of the real CDC design and hence can be used to study the performance of the CDC under more realistic conditions. It was tested in an electron beam at LEPS/SPring-8 in July 2015, as shown in Fig. 32 (right), to examine the performance for three different gas mixtures. The hit efficiency, spatial resolution, and drift velocity for different applied high voltage and different threshold values were investigated. Figure 34 shows the hit efficiency and the spatial resolution as a function of applied high voltage. The spatial resolution was extracted from the standard deviation of residual distributions by fitting tracks excluding one layer. Therefore, the resolution here includes a tracking uncertainty.

<sup>5</sup> In this test, hit efficiency was saturated at nearly 95% due to the weakness of signal cables against electronic noise. This inefficiency was overcome by modifying cables after the test.

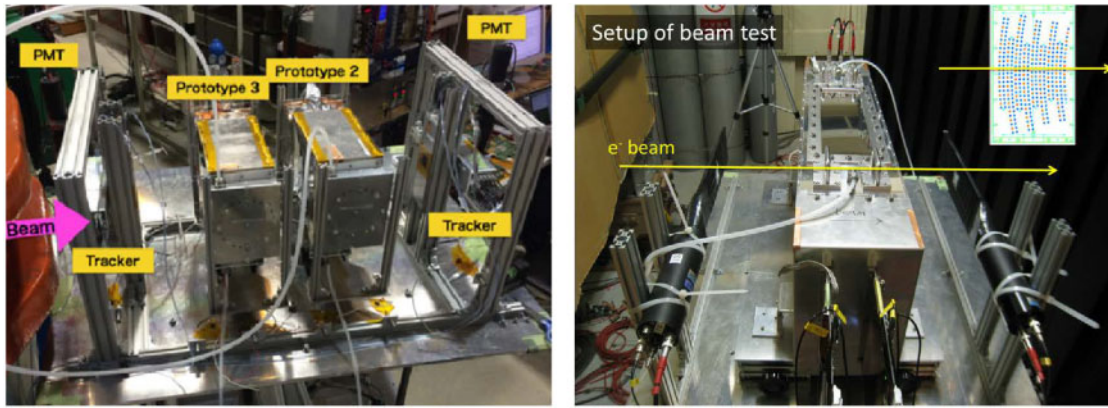


**Fig. 32.** Setups of the beam test of the second and third prototypes at ELPH/Tohoku University (left), and the beam test of the fourth prototype at LEPS/SPring-8 (right).

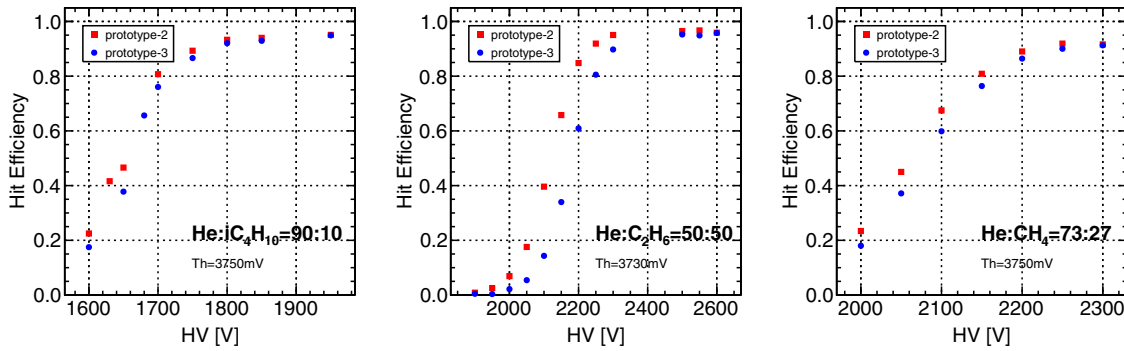


**Fig. 33.** Hit efficiency of the second and third prototypes for gas mixtures of He:i-C<sub>4</sub>H<sub>10</sub> (90:10) (left), He:C<sub>2</sub>H<sub>6</sub> (50:50) (middle), and He:CH<sub>4</sub>(73:27) (right). The second and third prototypes have sense wire diameters of 25 and 30  $\mu\text{m}$ , respectively.

The conclusion from the prototype studies is that the He:i-C<sub>4</sub>H<sub>10</sub> (90:10) gas mixture satisfies the requirements for efficiency and spatial resolution. These results, together with the Garfield predictions, are now used in the current Geant4 simulations.

#### 5.2.4. Aging tests

A preliminary aging test was performed in July 2014 at Osaka University. A test chamber was produced with Au–W sense wires of  $\phi 25 \mu\text{m}$  and Al field wires of  $\phi 80 \mu\text{m}$  and a He:i-C<sub>4</sub>H<sub>10</sub> (90:10) gas mixture. A central sense wire is the wire to be tested for the aging effect. There are two holes on each of the sides to irradiate X-rays with a <sup>55</sup>Fe source. One, “Side A”, is used to give charges with two <sup>90</sup>Sr sources, and the other, “Side B”, is used for reference as a not-aged sample wire.

To accelerate the aging (charge accumulation), the applied HV value of the test wire was set to 2600 V when the wire is exposed to <sup>90</sup>Sr sources, and an HV of 1500 V was applied to the other six wires. In this condition, we obtained an electric current of  $\sim 6.5 \mu\text{A}$  on the test wire. After every 30 minutes of exposure to two <sup>90</sup>Sr sources, the <sup>90</sup>Sr sources were replaced by a <sup>55</sup>Fe source for the gain measurement with 5.9 keV X-rays.

After about 21 hours, the accumulated charge reached about 47 mC/cm; the ratio of the ADC values of “Side A” against “Side B” is shown in Fig. 35. The black points indicate the results of the gain

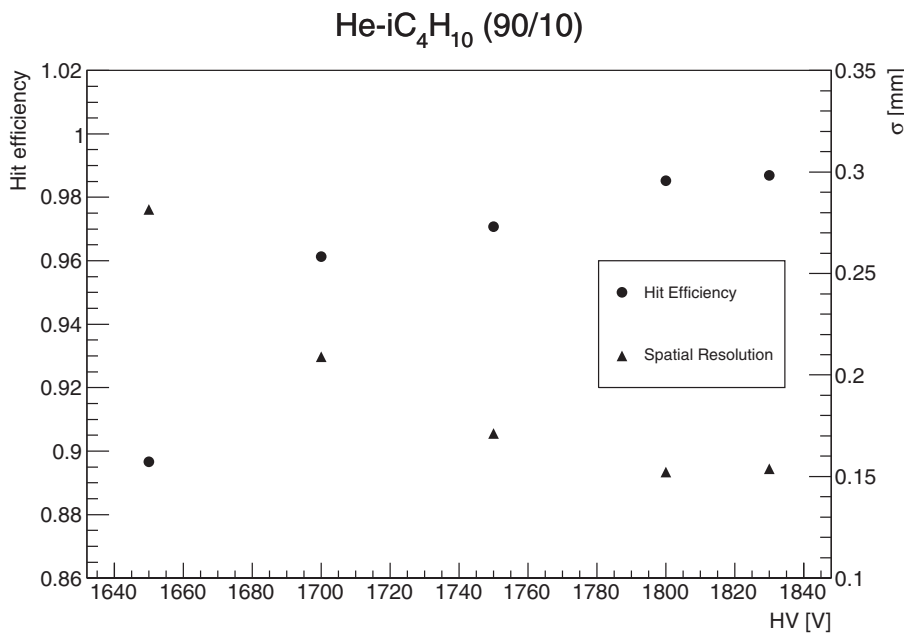


**Fig. 34.** Hit efficiency (left axis, circle markers) and spatial resolution (right axis, triangle markers) for the fourth prototype as a function of the applied high voltage.

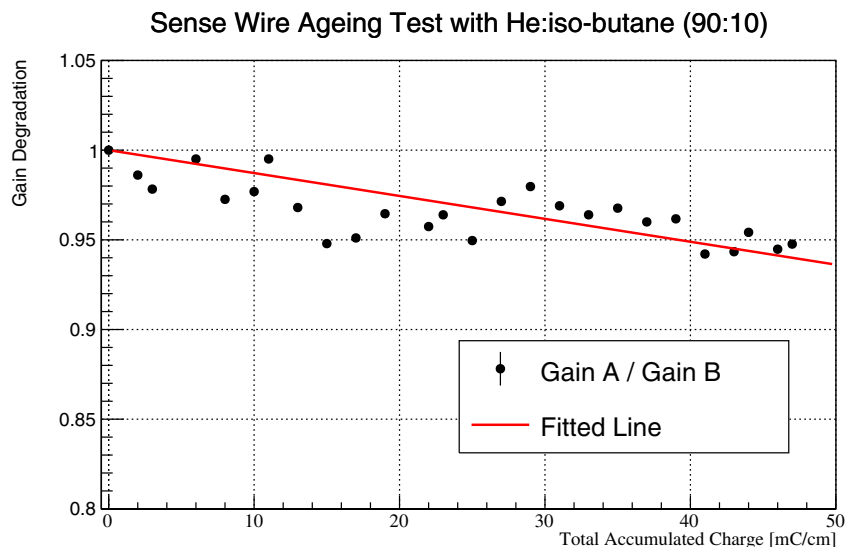


**Fig. 35.** The first result of the aging test with He:i-C<sub>4</sub>H<sub>10</sub> (90:10). The black points indicate the gain drop as a ratio of the measured gain against the gain not-aged area (Side B). The red line shows the fitted result with the data. The best-fit value of the gradient is  $-0.00132$ , corresponding to a gain drop of  $0.13\%/\text{mC}/\text{cm}$ .

measurement with only statistical uncertainties, and the red line is a fitted function with the points and a fixed offset ( $= 1.0$ ). The systematic uncertainty is not considered here. The best-fit value of the gradient is  $-0.0013$ , corresponding to a gain drop of  $0.13\%/\text{mC}/\text{cm}$ . The temperature, humidity, and atmospheric pressure were recorded in the experimental room during the measurement and no significant changes were observed.

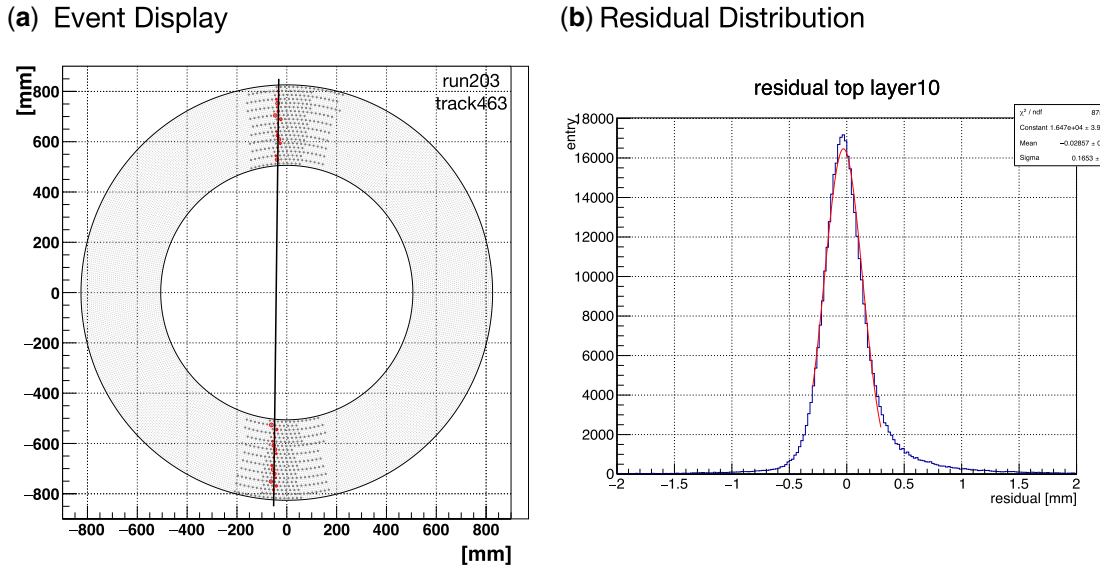


**Fig. 36.** (a) Typical event display in cosmic-ray tests. (b) Residual distribution for layer 10 at 1825 V. The distribution is fitted with a Gaussian.

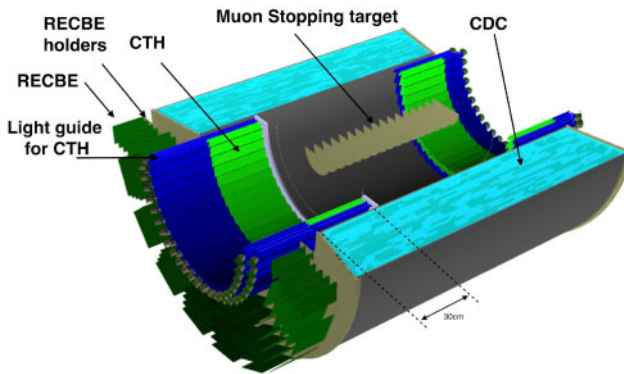


**Fig. 37.** A cross-sectional view of CyDet showing the layout of the CTH.

By considering our running period in Phase-I ( $O(100)$  days), the accumulated charge should be less than  $2 \text{ mC/cm/wire}$  with an estimated gain drop at the end of COMET Phase-I of only 0.3%, which is sufficiently small.

#### 5.2.5. Cosmic-ray tests

The CDC was constructed in 2016, and its performance evaluation test using cosmic rays started in summer 2016 [64]. Stable operation of the CDC was achieved with the He:i-C<sub>4</sub>H<sub>10</sub> (90:10) gas mixture and an applied high voltage up to 1850 V. Figure 36(a) shows a typical event display where a clear cosmic-ray track can be drawn. From the deviation of drift distance from the distance of closest approach between a hit wire and a reconstructed track, a residual distribution was obtained as shown in Fig. 36(b), giving a position resolution of  $170 \mu\text{m}$  including a tracking uncertainty.

#### 5.3. CyDet trigger hodoscope

The CyDet trigger hodoscopes (CTH) are placed at the upstream and downstream ends of the CDC to generate the first-level trigger. Figure 37 shows the location of CTH in the cross-sectional view of

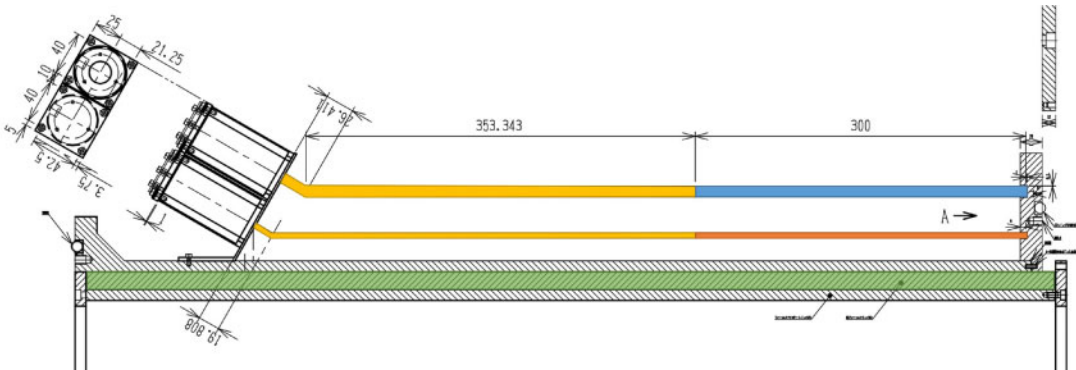


**Fig. 38.** Drawing of the downstream trigger hodoscope module. The yellow, blue, and orange parts correspond to the light guide, Cherenkov radiator, and plastic scintillator, respectively. For the upstream part, the design is the same but the length of the light guide is shorter.

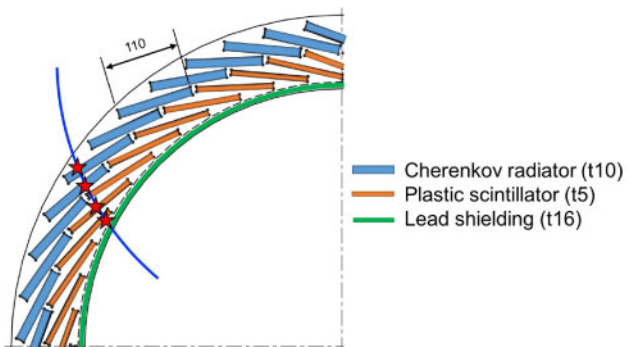


**Fig. 39.** A quarter of the hodoscope ring, also showing the example four-fold coincidence by a signal electron. Counters are tilted and located shifting half width so that four-fold coincidence with the neighboring counters can be required, in order to reduce accidental coincidence.

CyDet. Their position defines the fiducial region, which is for tracks entering the CDC between the CTH counters and then triggering after the first or subsequent turns. Each hodoscope consists of 48 modules, each module comprising a plastic scintillator and a Lucite Cherenkov counter, separated by a few cm, as shown in Fig. 38. The Cherenkov counters, together with the scintillation counters, identify electrons from the protons from nuclear muon capture and cosmic-ray muons. The Cherenkov and scintillation counters are tilted at specific angles to the tangent of the concentric circles so that a four-fold coincidence (two-fold in both Cherenkov and scintillator rings) can be made with a high acceptance for the signal electrons and a reduction in the fake triggers caused by  $\gamma$ -rays as shown in Fig. 39. A simple two-fold coincidence would be insufficient to reduce the fake trigger rates from energetic  $\gamma$ -ray conversions.

### 5.3.1. Design of CTH

The trigger hodoscopes must be operated in a 1 T solenoidal magnetic field and a high neutron fluence of about  $10^{11}$  (1 MeV-equivalent) neutrons per  $\text{cm}^2$ . The signal–noise ratio S/N is required to be larger than 20, and the time resolution less than 1 ns.

Despite the high magnetic field, the photosensor that best meets these requirements is a fine-mesh photomultiplier tube (PMT). Multi pixel photon counters (MPPCs) would not survive the neutron irradiation and avalanche photodiodes would not provide a sufficiently good S/N.

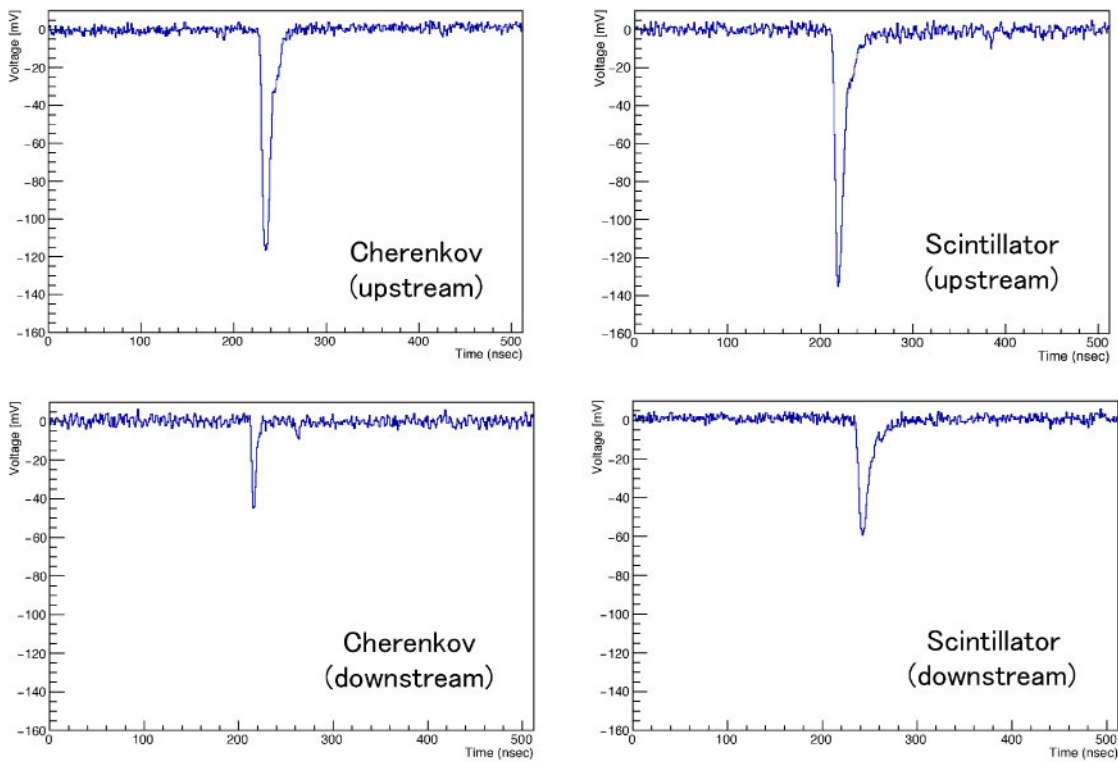


**Fig. 40.** Waveforms from the Cherenkov detector (left) and the scintillator (right).

Each module has two layers:  $300 \times 110 \times 5 \text{ mm}^3$  ultra-fast PVT-based scintillator (ELJEN EJ-230) [65] and  $300 \times 110 \times 10 \text{ mm}^3$  UV-transparent acrylic plastic as a Cherenkov radiator to identify the electrons. The acrylic plastic and the plastic scintillator are separately wrapped and connected via a light guide to a Hamamatsu H8409-70 [66] PMT. This PMT has a small transit time spread of 0.35 ns and a high gain of  $\sim 10^7$  and can operate in 1 T magnetic field, although the gain is somewhat reduced. To compensate for this, the signals are subsequently amplified.

The fiducial region is defined by the trajectories of signal electrons that enter the CDC on their first or multiple turns, and subsequently hit the CTH to generate the trigger. The length of the CTH counters has been optimized and chosen as 30 cm, in order to maximize the acceptance of the signal electrons.

The support structure of the trigger hodoscopes must both support the modules and also isolate them from the helium gas that surrounds the muon stopping target as helium causes degradation of PMTs due to increased after-pulsing.

### 5.3.2. Prototype tests

A beam test using 155 MeV/c electrons was carried out to evaluate detector performance without a magnetic field. Figure 40 shows typical waveforms measured in the beam test. The scintillator modules produce more light than the Cherenkov modules, and higher light yields are recorded for the upstream modules, which have shorter light guides. For all four module types, the readout meets the required S/N ratio.

Figure 41 shows the distribution of the difference in detection time between the Cherenkov detector and the scintillator (both were arranged closely so that the electron beam hit both counters).

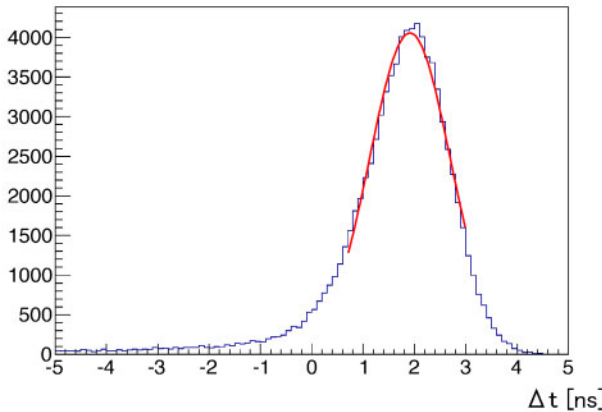


**Fig. 41.** Detection time difference between the Cherenkov detector and the scintillator.

From fitting the distribution, the combined  $\Delta T$  resolution is measured as 0.8 ns, which meets the requirement of resolution better than 1 ns.

*CTH trigger rates* A CyDet trigger is made by a four-fold coincidence of two adjacent CTH pairs of a scintillation and a Cherenkov counter. An example event is shown in Fig. 39. The trigger rate was estimated with a trigger coincidence window set at 10 ns and the time window of measurement either from 500 ns to 1170 ns or 700 ns to 1170 ns, as described in Sect. 10.1. The major background sources for fake trigger signals come from photon conversion in or near the CTH, with most photons coming from bremsstrahlung from Michel electrons produced in muon decay at rest in the stopping target. To reduce the fake trigger signals additional lead (Pb) shielding, about 16 mm thick, is required beneath the CTH. With this shielding, trigger rates of 26 kHz and 19 kHz are estimated for the time window of measurement from 500 ns and 700 ns respectively. These rates are the sum of the separate upstream and downstream CTH rates. As these trigger rates result in a rather high data rate, an online trigger selection using the CDC hit information will be implemented; this is discussed further in Section 8.1.

*CTH hit rates* The effects of this beam flash in the CTH have been examined experimentally. It was found that the gain of the CTH scintillator counter and of the CTH Cherenkov counter begin to degrade if the beam flash is greater than 25 MIPs for the scintillator and 120 MIPs for the Cherenkov respectively. The test results are summarized in Fig. 42. From the simulations, the average beam flashes are less than these limits and it is concluded that the effect of beam flash will not cause any loss.

The instantaneous rates after the prompt beam flash are estimated for each counter of the upstream CTH and downstream CTH separately as shown in Table 6. It should be noted that they are average instantaneous rates during the time period.

#### 5.4. CDC tracking

The CDC track reconstruction consists of a track finding process followed by a track fitting process. The former selects good hits in order to identify track-like structures and eliminate background noise, whereas the latter does track fitting with Kalman filtering to determine which hits are a most probable part of the track, whether a single continuous track is a good interpretation of the hit pattern, and

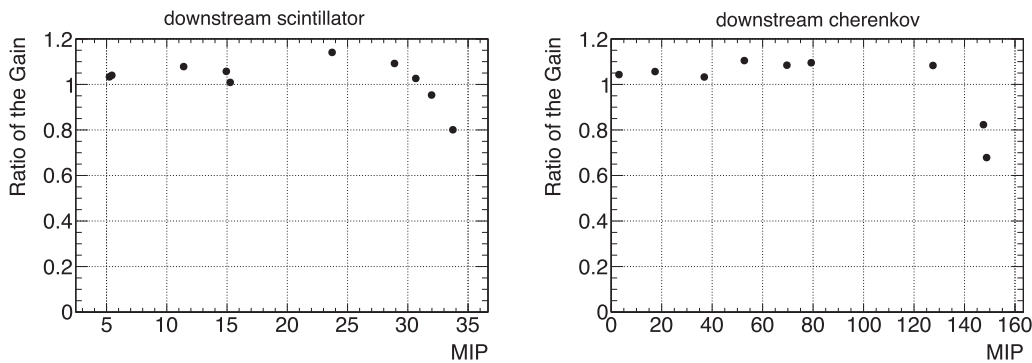


**Fig. 42.** Gain drop of the CTH scintillator counter (left) and CTH Cherenkov counter (right), measured by the second LED pulses, as a function of the pulse height of the first LED to simulate different amplitudes of beam flash. The gain drops of the CTH plastic scintillator and CTH Cherenkov counter start from 25 MIPs and 120 MIPs equivalent respectively.

**Table 6.** Average instantaneous hit rates during the time period after the prompt beam flash, from 200 ns to 1170 ns.

	upstream scintillator	upstream Cherenkov	downstream scintillator	downstream Cherenkov
Average rate (MHz)	3.5	1.5–2	4	3

(assuming that it is) finds the best estimate of the momentum of the charged particle that made the track. In the fitting process it is necessary to consider both single-turn and multiple-turn tracks.

*Track finding and reconstruction* The CyDet offline track finding algorithm outlined in this section filters out background hits using three main stages [67,68]. First, a gradient-boosted decision tree (GBDT) is used to classify the hit as signal or background based on the properties of the hit itself (local features), and the properties of neighboring hits (neighbor features). Second, it performs a circular Hough transform on the output of this GBDT, reweights the result, and inverts the transform to recover information about which hits form a circular path with signal-like hits. Third, a new GBDT uses this information, the local features, and the neighbor features to classify hits as signal or background. The output at this hit-filtering level suppresses nearly 98% of background hits while keeping 99% of signal hits<sup>6</sup>.

The algorithm has been tested on simulation data generated using Geant4 and ICEDUST. Figure 43 gives an example of a truth-labeled input event. The magenta points are the signal hits, while the dark-blue points are the background hits. The event shown has an uncommonly high occupancy of 15.4%, to illustrate the performance of the algorithm.

*Neighbor-level GBDT* The algorithm begins by considering three “local-level” classification features of each hit wire. The first of these is the energy deposition of the hit. A cut on this feature alone can reduce the background hits by 68% while retaining around 99% of signal hits. The second feature is the timing of the wire hit relative to the timing of the hit in the CTH trigger system. Signal hits tend to occur soon after these trigger hits, while background hits occur randomly with respect

<sup>6</sup> This analysis makes use of the `scikit-learn` [69] package in Python 2.7.

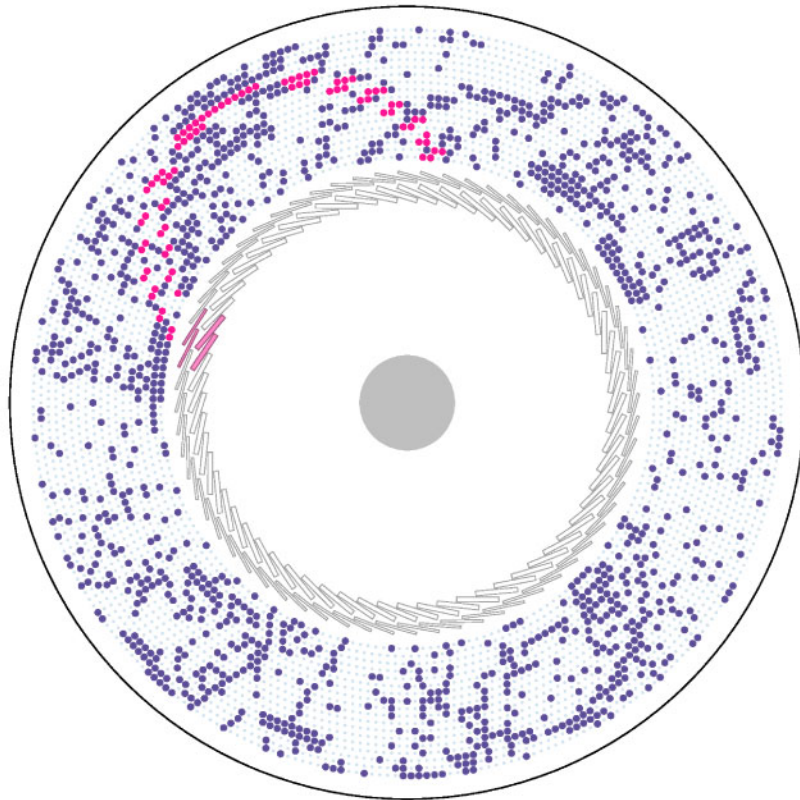


**Fig. 43.** A 15.4% occupancy event in the CyDet. This is a projected view from the central plane of the detector, looking in the direction of the beam line. The dark-blue points are hits caused from background processes, while the magenta hits correspond to the signal electron. The magenta-filled boxes represent the CTH hits by the signal electron.

to the trigger timing. The third feature is the hit’s radial distance from the center. The magnetic field and geometry are tuned so that signal tracks curve through the fiducial volume, rarely reaching the outer layers, yet always passing through the inner ones. The background hits are distributed more evenly throughout the layers, peaking slightly at the inner and outer layers.

The separation power of these features is further exploited by defining features that describe the neighboring wires of a hit, i.e., the “neighbor-level” features. Due to the alternating stereo angles, the features on the neighboring wires in the same layer are more powerful than adjacent layers, referred to as the left and right neighbors of a hit. Along with the local features, the left-right timing and energy deposit features are also used. This defines seven input features for the GBDT, referred to as the neighbor-level GBDT. Its output is visualized in Fig. 44.

While local and neighbor features alone yield promising results, there are still some isolated clusters of misclassified background hits, as well as a diminished response for isolated signal hits. To correct this, a circular Hough transform is used on the output of the GBDT to determine which hits lie in a circular pattern with other signal-like hits. Weights can then be defined for each wire hit based on the Hough transform and the GBDT output. Finally, a second GBDT, the track-level GBDT, is used to discriminate signal from background hits. The output from this GBDT, shown in Fig. 45 on the Monte Carlo sample used, demonstrates excellent separation between signal and background.

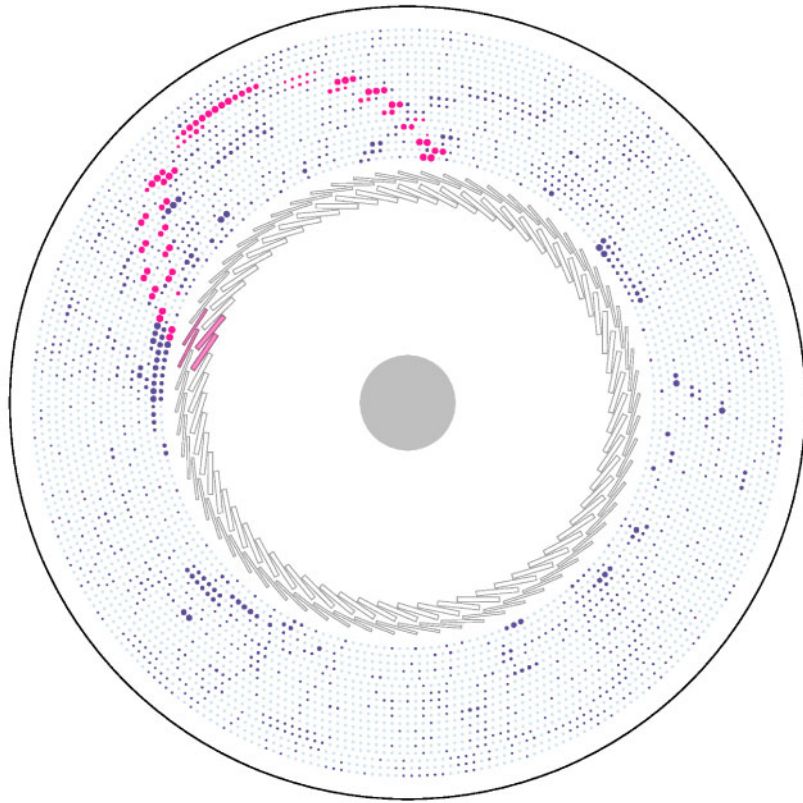


**Fig. 44.** A visual representation of the neighbor-level GBDT applied to the event shown in Fig. 43. The locations of the hits are shown by the outlines of the hits. The fill is scaled with the output of the GBDT, where a full circle corresponds to a signal-like response.

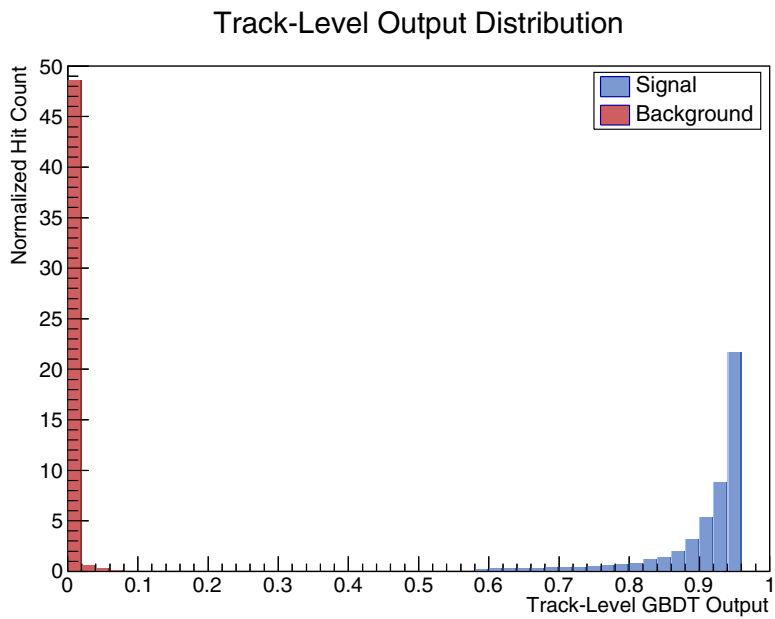


**Fig. 45.** Distribution of the output of the track-level GBDT, comparing the response from signal hits to the response from background hits.

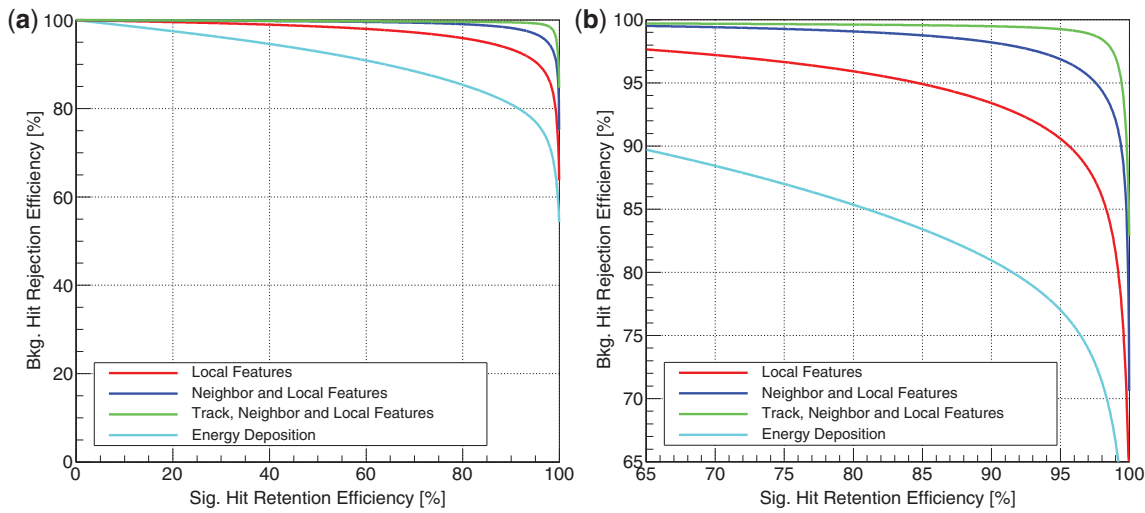


**Fig. 46.** ROC curves for four independent classifiers. The red curve is from a GBDT trained on energy deposition alone, the blue curve is from the neighbor-level GBDT, and the green curve is from the track-level GBDT. The cyan curve represents the cut-based case using energy deposition alone.

ROC curves are plotted in Fig. 46 to demonstrate the ability of the algorithm to reject background as a function of its ability to retain signal. The plots compare the performance of the neighbor-level GBDT, the track-level GBDT, and the baseline separation power of solely the energy deposition of a hit. They show that the background rejection rate for a signal efficiency of 99% is 98% with the track-level GBDT but just 68% using energy deposition alone.

## 6. StrECAL: the straw-tracker ECAL detector system

After the physics data taking with CyDet during Phase-I running, another detector system, StrECAL, will be installed instead of the CyDet. The StrECAL is a combination of a straw-tracker (a low-mass detector consisting of planes of gas-filled straws acting as drift chambers) and a crystal electromagnetic calorimeter. The primary purpose of this detector in Phase-I is to make direct measurements of the composition of the muon beam, but the detectors are very similar to those that will be employed in Phase-II, and act as a prototype for the Phase-II detectors.

### 6.1. Straw tracker

The straw tracker to be developed for Phase-I will make direct measurements of the particles in the muon beam line, and the rate of particle production (in particular antiprotons), as a function of the beam energy, and other backgrounds. It will be placed inside the vacuum vessel and the detector solenoid (DS), which has a field strength of 0.8–1.1 T. The detector will provide a precise measurement of a particle’s momentum and its identity, through  $\frac{dE}{dx}$ ,  $E/p$  and the time of flight information in combination with the calorimeter. For Phase-I, as shown in Fig. 19, many kinds of particles will reach and enter the DS. For both phases, the volume inside the magnet will be evacuated to enable good-quality measurements of the beam particles in Phase-I and to minimize the amount of material in Phase-II.

#### 6.1.1. Overall structure

The overall structure of the straw tracker is schematically shown in Fig. 47. Each of the five tracker super-layers, or “stations”, consists of four planes; two to measure the  $x$  coordinate and two to

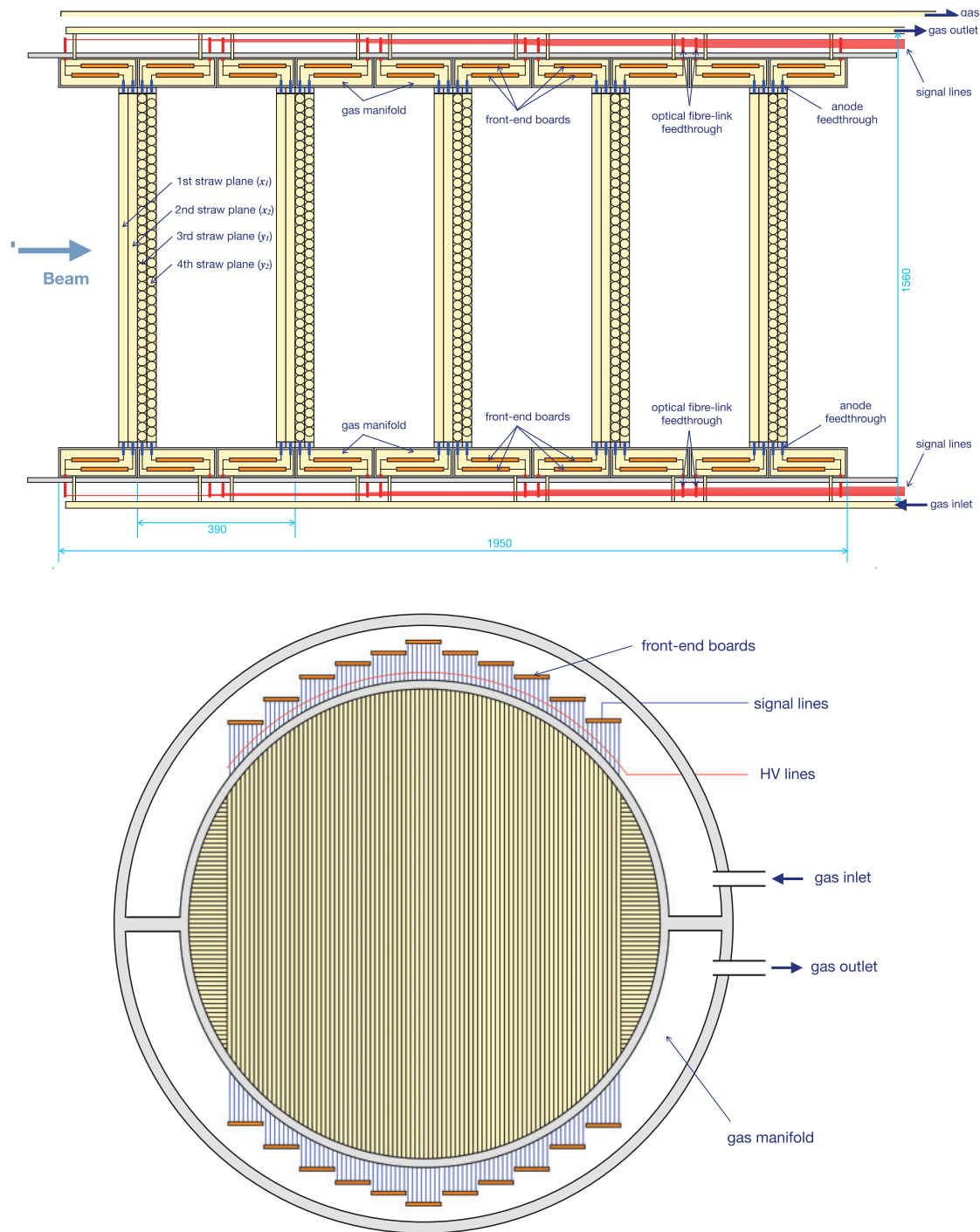


**Fig. 47.** Schematic view of the straw tracker. (Top) Side view. The straw dimensions are scaled by a factor of three for clarity. (Bottom) Cross-sectional view of a plane.

measure the  $y$  coordinate. Each pair of planes is staggered by half a straw diameter in order to resolve any left-right ambiguities. Each layer is constructed as a stand-alone unit and mounted on the detector frame that is inserted and removed from the DS on rails and linear bearings. A spare layer will also be built. Anode wires, made of gold-coated tungsten, are extracted via a feedthrough into the gas manifold as shown in Fig. 47. The anode wires are held at high voltage and the straw

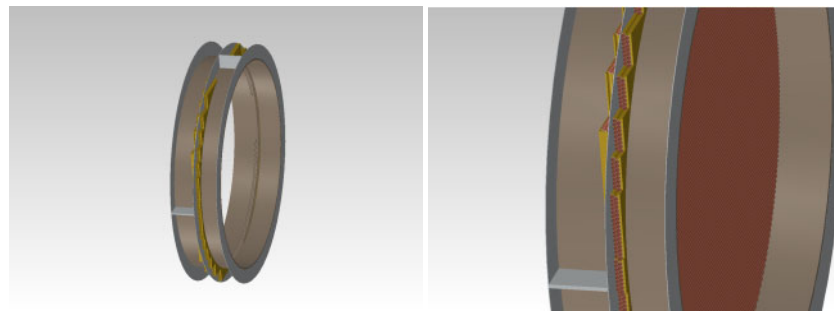


**Fig. 48.** Design of the support structure for one tracker station. (Left) Overview of one station without straws. (Right) Close-up view with straws.

wall is grounded, to act as the cathode. A gas mixture of 50% Ar and 50% C<sub>2</sub>H<sub>6</sub> is provided from this gas manifold to the straw tube. The straws have a diameter of 9.75 mm, range in length from 692 to 1300 mm, and are mounted on aluminum ring supports.

#### 6.1.2. Mechanical construction

The straw walls conduct electricity, and are made of a metallized polyethylene terephthalate (PET) film of 20  $\mu\text{m}$  thickness<sup>7</sup>. The support rings for the straws have inner and outer radii of 65 and 78 cm, respectively. Gas manifolds and electrical connections are also attached to the supports. The gap between them provides space to mount the front-end electronics, the power distributors, and the HV circuit. Each of the five stations are equally spaced and rigidly attached to each other.

Finite element analyses found an excess tension of 1.7 kg<sub>F</sub> on each straw compared to the original expectation, but also indicated that this results in acceptably small deformations.

#### 6.1.3. Straw tube

A method of straw production that does not require multiple over-woven layers has been developed by the JINR group for the NA62 experiment at CERN [70]. In this method, a single layer is rolled and attached to itself in a straight line using ultrasonic welding as schematically shown in Fig. 49. The JINR-COMET group have tried to develop a new welding station in order to produce the COMET-design tube, which is thinner than the NA62 tube, and finally succeeded in producing a 20  $\mu\text{m}$ -thick wall straw tube, after some R&D with the JINR-NA62 group. The provided straws, shown in Fig. 50, were mechanically tested and confirmed to be robust enough. The mass production of straw tubes for Phase-I, 2900 tubes including 500 spare tubes, has already been completed by the JINR-COMET group.

Possible deformations of the straw as a function of the pre-tensioning value were investigated since the pre-tensioning must be quite high to avoid deformations when it is operated inside the vacuum<sup>8</sup>. The measurement results for sag (defined by the deformation made by gravity from the normal position without gravity, also including 1.5 mm measurement offset) and elongation (including 2 mm measurement offset) for a 1 m straw are shown in Fig. 51. They show that tensions higher than 1 kg<sub>F</sub> prevent sagging, and this results in elongations of 1.7–2.0 mm. Therefore, straw deformations can be avoided by stretching the straws by 2 mm during assembly.

<sup>7</sup> R&D is currently ongoing to reduce the wall thickness; see Sect. 6.1.3.

<sup>8</sup> As a point of reference, the NA62 tracker is pre-tensioned at 1.5 kg<sub>F</sub> on each straw tube.

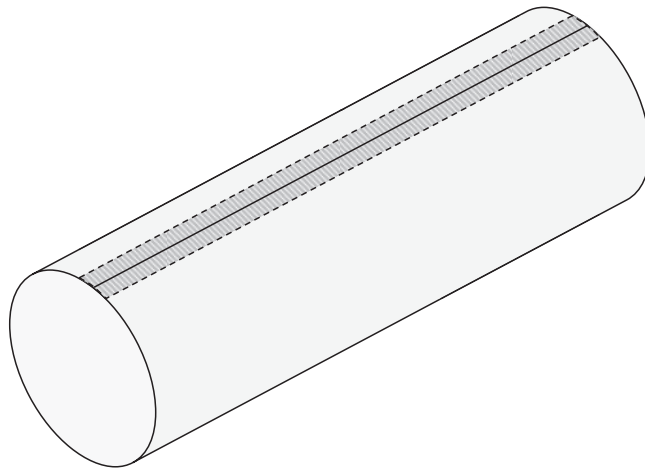


**Fig. 49.** The new straight-adhesion style for straw construction.



**Fig. 50.** Sample tubes with  $20 \mu\text{m}$ -thick walls with  $70 \text{ nm}$ -thick aluminum layers.

The sense wires are chosen to be gold-plated tungsten containing 3% rhenium. Additional supports for the anode wires are not required; wire stability can be estimated from the electrostatic force on an off-center anode wire [71]:

$$L_c = \pi R(CV)[2\pi\epsilon_0 T]^{1/2}, \quad (20)$$

where  $T$  is the tension on the wire,  $V$  is the applied voltage,  $C$  is the capacitance per unit length,  $L_c$  is the critical wire length for a given tension, and  $R$  is the straw radius. Assuming a straw radius of 4.9 mm, an anode wire radius of  $12.5 \mu\text{m}$ , a capacitance/length of  $10.5 \text{ pF/m}$ , a maximum voltage of 2.2 kV, and a critical length of 2 m, the required tension on the wire is found to be approximately 70 g.

#### 6.1.4. Simulation studies for the straw tracker

The processes occurring in the straw chamber are simulated using three simulation tools, HEED [72], MAGBOLTZ [73], and Garfield [74].

Figure 52 shows the results of these simulations. Figure 52(a) shows the calculated drift velocity for an Ar–C<sub>2</sub>H<sub>6</sub> 50:50 mixture as a function of the applied electric field, Fig. 52(b) shows the diffusion

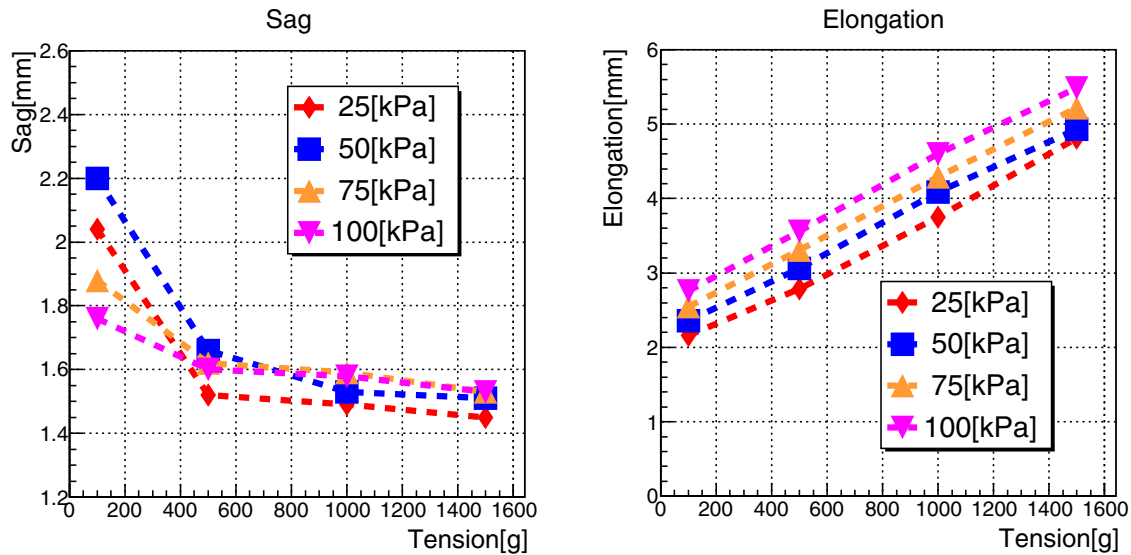


**Fig. 51.** Straw-pre-tensioning study results. (Left) The sag that is found for various pressure differences across the straw wall as a function of the applied tension. (Right) Elongations of the straws. The sag results include 1.5 mm measurement offset, which should be subtracted from the data points in order to get the actual sag values. The elongation results also include 2 mm measurement offset.

coefficients, and Fig. 52(c) shows the drift lines, where the strength of the magnetic field is 1 T. According to this study, the drift velocity is expected to be saturated at approximately 5 cm/ $\mu$ s for an electric field higher than  $10^3$  V/cm. Relatively low diffusion coefficients, roughly 100–300  $\mu$ m/cm, are expected for an electric field of the order of  $10^3$  V/cm; hence good spatial resolution can be expected.

#### 6.1.5. Spatial resolution estimation

To estimate the intrinsic spatial resolution, Garfield++ [75] simulations, validated where possible through comparisons with real data, are employed. The expected spatial resolution as a function of the distance from the wire for a gas mixture of Ar:C<sub>2</sub>H<sub>6</sub> (50:50) and an HV of 1900 V, where the incident particle is assumed to be a 100 MeV/c electron, is shown in Fig. 53. Electrical noise is not taken into account as it is not easy to predict the actual noise level. The results indicate that the straw tracker will satisfy the required performance for the beam background measurements.

#### 6.2. Readout electronics

The readout electronics boards will be installed in the gas manifold, so the front-end electronics must operate in the vacuum inside the DS to measure the analogue signal from the anode wires. All signals are digitized at the front-end boards, and stored in digital pipelines to allow for trigger latency. Once a trigger is issued, only those channels with signals above a set threshold are read, stored in buffers, and then serially transferred to the data acquisition system. The events are then rebuilt, analyzed, filtered, and finally committed to permanent storage.

To achieve a momentum resolution better than 200 keV/c, a spatial resolution of  $\sim$ 100  $\mu$ m is desired; this requires a timing resolution of better than 1 ns in the readout board.

The front-end boards, termed ROESTI (readout electronics for straw tube instrument), contain all the front-end processing: preamplification and pulse shaping, discrimination, and digitization, controlled by an FPGA-based readout controller, as shown in Fig. 54. Preamplification, pulse shaping,

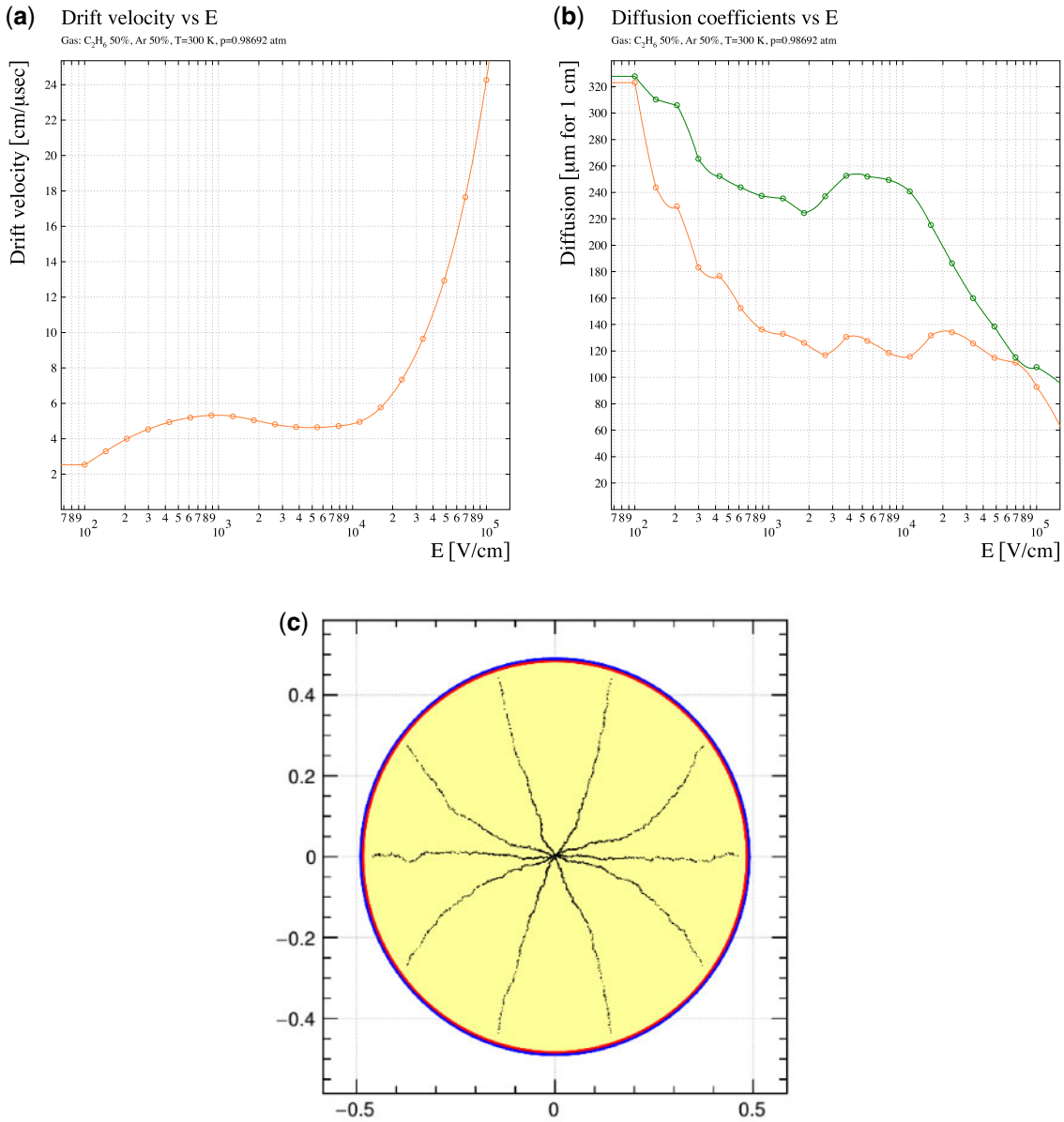


**Fig. 52.** Gaseous detector simulations for the COMET straw tracker with Garfield, for an Ar–C<sub>2</sub>H<sub>6</sub> 50:50 mixture under 300 K and 0.986 92 atm conditions. (a) Drift velocity and (b) diffusion coefficients as functions of the applied electric field and (c) drift lines and isochrones. For the diffusion coefficients, the orange and green lines correspond to the transverse and longitudinal coefficients, respectively.

and signal discrimination are performed by the ASD (amplifier shaper discriminator) chip<sup>9</sup>, and the amplified signal is then digitized by a DRS4 chip [76]. The digitized waveform data, correction data, and relevant metadata are then sent out via an optical fiber. The FPGA also has other input/output lines for triggering and JTAG connections. Development of the ROESTI board is supported by the KEK Electronics Group and the Open Source Consortium of Instrumentation (OpenIt).

<sup>9</sup> This ASD chip was originally developed for ATLAS MDT/TGC front-end electronics, and recently modified for Belle-II CDC electronics; this version is adapted from Belle for the COMET straw front-end.

## Position Resolution

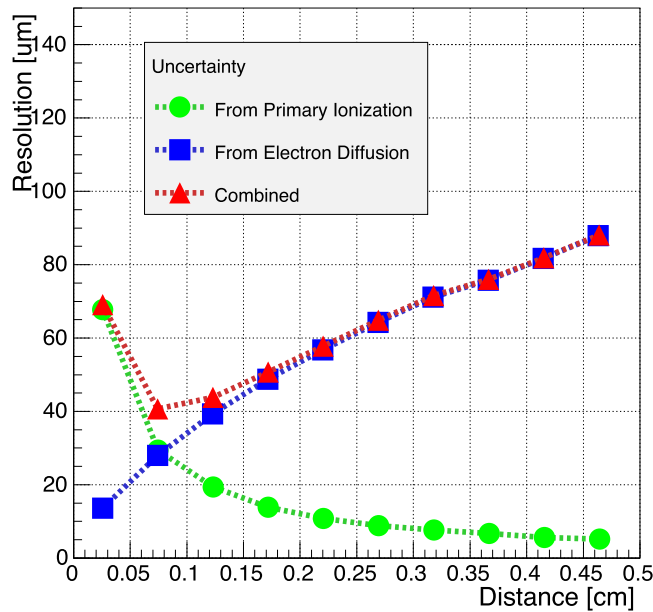


**Fig. 53.** Expected spatial resolution as a function of the distance from the wire, simulated by Garfield++ (Ar:C<sub>2</sub>H<sub>6</sub> (50:50), 1900 V).

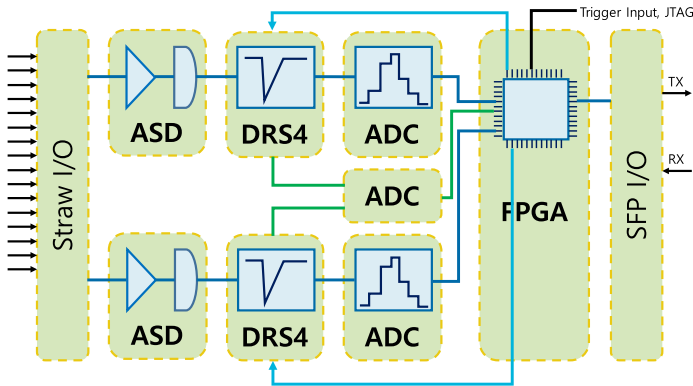


**Fig. 54.** The ROESTI front-end board for the straw tracker.

**FPGA firmware design** A modern FPGA design, Artix-7 (XC7A200T-2FBG676C, Xilinx), is used on the ROESTI board. The firmware is composed of five blocks; network interface, monitor, module control, trigger interface, and data interface. In the network interface block, the input/output signal can be transmitted/received between a PC and several boards. A UDP connection for parameter control between the board and PC is also found in this block. In the monitor block, the temperature and voltage in the FPGA are monitored and detection and correction of SEU (single-event upsets) and URE (unrecoverable errors) are also handled here. In the module control block, all chip parameters are controlled, including the ASD threshold for the DAC, the offset voltage, sampling speed for the DRS4 module, and, following a trigger signal, the start signal for sending information from the DRS4 to the ADC is issued. In the trigger interface block the trigger signal is handled and the information sent to the module control and data interface blocks. In the data interface block, ADC and

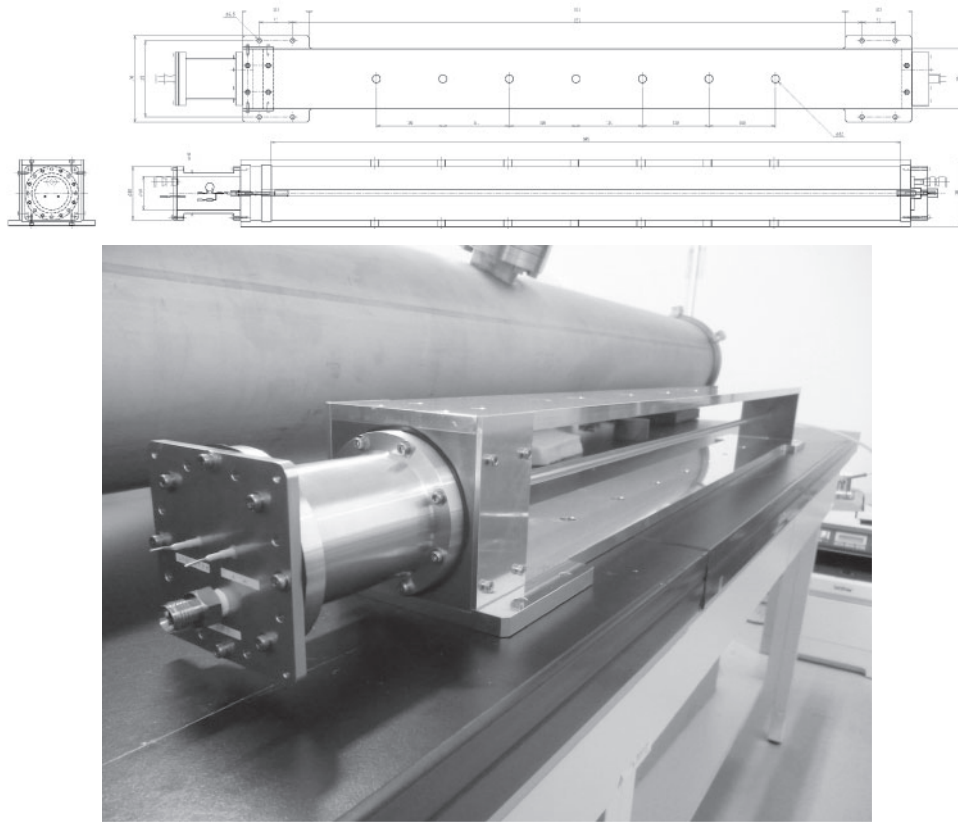


**Fig. 55.** The single-straw prototype. (Top) Drawing. (Bottom) Photo of the whole view.

monitor data are received and converted to packet data, which are then sent to the network interface block.

#### 6.2.1. Prototypes

*The single-straw prototype* A small prototype (the “single-straw prototype”) was built to investigate the gas tightness, operation in vacuum, and noise shielding.

A new feedthrough system was developed that provides not only electrical connections but also the straw tensioning scheme. The straws are stretched by rotating the bushing part of the feedthrough to pull the straw tube by about 2 mm, equivalent to a pre-tension of 1 kg<sub>F</sub>. Figure 55 shows a drawing and photograph of the single-straw prototype and the installation of the single-straw prototype into the vacuum vessel.

Measurements of the gas tightness revealed a leak rate of 0.0035 cm<sup>3</sup>/min/m, which, when scaled to the full spectrometer, is well within what is needed to keep pumping rates at modest levels, as shown in Fig. 56. The leakage test using a full-scale prototype is also conducted, which resulted smaller leakage than expected from the single-straw leakage test. Electrical shielding properties have also been tested using this prototype. Several gas mixtures were tested using <sup>55</sup>Fe as an X-ray source. By changing the applied HV, the gas gain was measured and the good gas amplification performance confirmed. These results from the single-straw prototyping validate the use of the newly developed straws with 20 µm walls for COMET Phase-I.

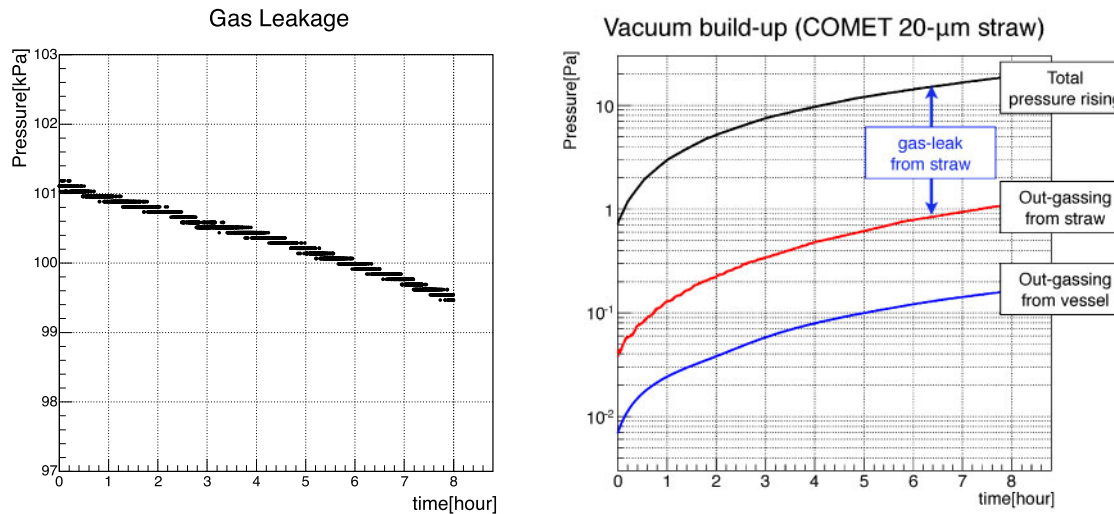


**Fig. 56.** Measured gas leakage: (Left) Pressure drop inside the straw tube as a function of time after it is over-pressurized to 2 bar. (Right) Pressure build-up as a function of time after pump closure.



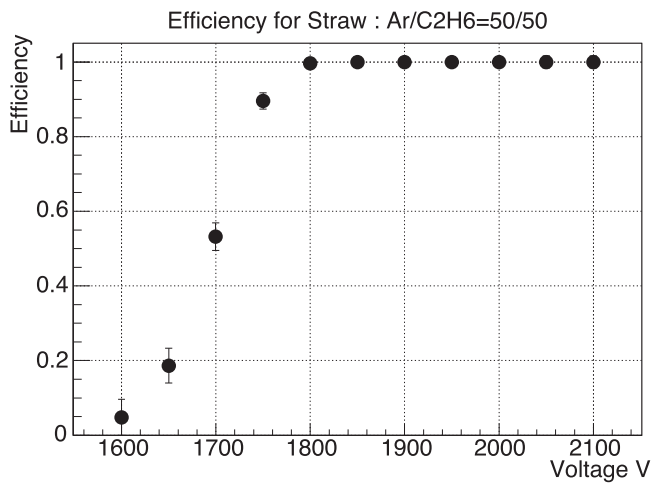
**Fig. 57.** The full-scale prototype, partially completed without the vacuum wall.

*Full-scale prototype* A second prototype, the “full-scale prototype”, has similar dimensions to a final tracker station but with fewer straws. It has six straw-tube planes, three for the  $x$ -coordinate and three for the  $y$ -coordinate, with each coordinate measured by 16 straw tubes. Figure 57 shows a partially completed prototype. The 20  $\mu\text{m}$ -wall straws are mounted using a newly developed feedthrough system and the entirety of the exterior is covered with a vacuum wall so that it can be evacuated, allowing the behavior in vacuum to be investigated. The prototype is constructed of aluminum so that it will not be affected by magnetic fields.

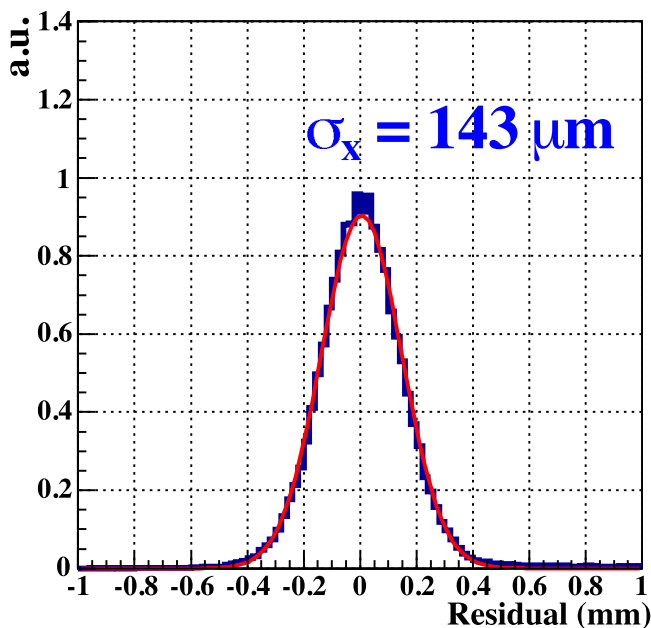
It has been operated in a 50–300 MeV/c electron test beam at the Research Centre for Electron Photon Science (ELPH), Tohoku University.

Figure 58 shows the measured single-straw detection efficiency for the Ar:C<sub>2</sub>H<sub>6</sub>(50:50) gas mixture as a function of applied HV. Figure 58 shows that a voltage higher than 1800 V results in full efficiency for a single straw although gaps between straw tubes<sup>10</sup> can lead to a small overall efficiency loss.

<sup>10</sup> The full-scale prototype has a small gap of 0.5 mm between each straw tube.



**Fig. 58.** Measured single-straw detection efficiency.



**Fig. 59.** Residual distribution for Ar:C<sub>2</sub>H<sub>6</sub>(50:50) gas mixture at HV = 1900 V.

Figure 59 shows the residual distributions for tracks. A spatial resolution of  $143.2 \mu\text{m}$  is obtained for an HV of 1900 V. This value includes the uncertainties arising from the precision of track reconstruction, and if this is taken into account the true spatial resolution is estimated to be  $119.3 \mu\text{m}$ . The left plot of Fig. 60 shows the dependence of the spatial resolution on the incident position for Ar:C<sub>2</sub>H<sub>6</sub>(50:50) and an HV of 2000 V, and the right plot shows the expected spatial resolution simulated with Garfield++. Here the green (open circle) plot shows the ideal spatial resolution. The left plot in Fig. 60 shows the measured incident-position dependence, which is well reproduced in the simulation as shown in the right plot of Fig. 60.

In conclusion, the detection efficiency and intrinsic spatial resolution are confirmed to meet requirements. The ability to maintain a vacuum inside the DS is also confirmed and expected to be better than what is required.

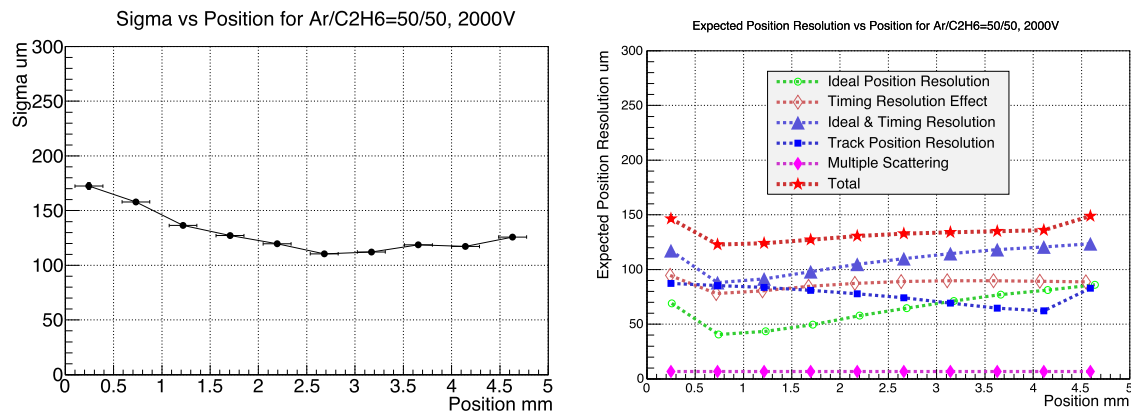


**Fig. 60.** Incident position dependence of the obtained spatial resolution, gas mixture = Ar:C<sub>2</sub>H<sub>6</sub>(50:50), HV = 2000 V. (Left) Data. (Right) Garfield++ simulation.

### 6.3. Electron calorimeter (ECAL)

The electron calorimeter (ECAL) system consists of segmented scintillating crystals. It is placed downstream of the straw tracker to measure the energy of electrons with good resolution and hence add redundancy to the electron momentum measurement. It will also provide an additional hit position on the electron track trajectory and provide the trigger signals.

The specifications for the ECAL are determined by its requirements for Phase-II running; they are an energy resolution of better than 5% at 105 MeV and a cluster position resolution that is better than 1 cm. The latter will enable the shower topology to also be used to discriminate electrons from neutrons and low-energy photons. The crystals need to have a good light yield, and fast response and decay times in order to reduce pileup. A schematic layout of the ECAL system is shown in Fig. 61.

*Scintillating crystals* The properties of candidate crystal types are summarized in Table 7. Taking into account both performance and cost, LYSO (lutetium–yttrium oxyorthosilicate, Lu<sub>2(1-x)</sub>Y<sub>2x</sub>SiO<sub>5</sub>) has been chosen for the ECAL. High segmentation is required both to reduce pileup and provide good position information. The ECAL will consist of crystal modules that have a 2×2 cm<sup>2</sup> cross section and whose length is 12 cm corresponding to 10.5 radiation length. The ECAL covers the cross section of the 50-cm radius detector region and 1920 crystals are needed.

*Photon detector* The photon detectors for the ECAL must be able to operate in the 1 T magnetic field, have a high quantum efficiency around the wavelength range of LYSO scintillation, and excellent linearity. The Hamamatsu S8664-1010 avalanche photodiode (APD) with an active area of 10×10 mm<sup>2</sup> satisfies these requirements; its characteristics are summarized in Table 8. Laboratory tests have been made to check the noise performance with a suitable preamplifier that confirm that the requirements are met.

#### 6.3.1. Readout electronics

A schematic diagram of the readout electronics for the ECAL system is shown in Fig. 62. The crystals and the APDs are located inside a vacuum vessel. The front-end card houses 16 full-bandwidth amplification channels that produce signals for energy measurements and four 4-input analogue adders that derive signals for triggering. In the full-bandwidth channel the input signal is amplified by a charge-sensitive amplifier (which integrates the signal), and then the signal shape is restored so

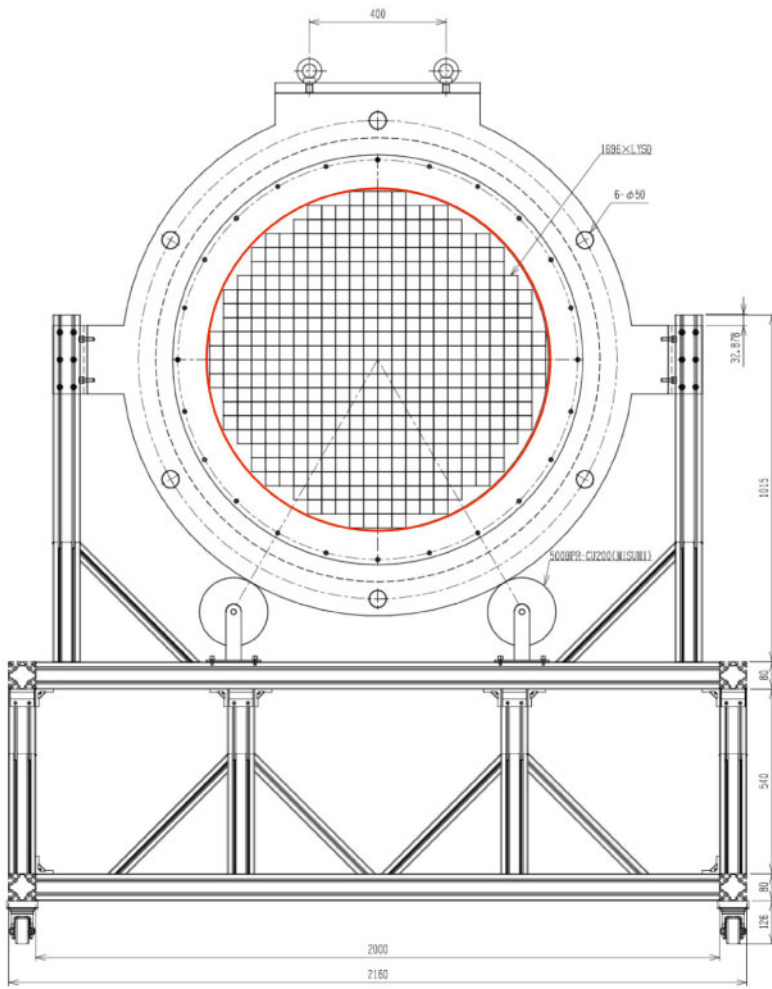


**Fig. 61.** A schematic layout of the electron calorimeter system. The matrix structures inside the red circle represent the LYSO crystal array.

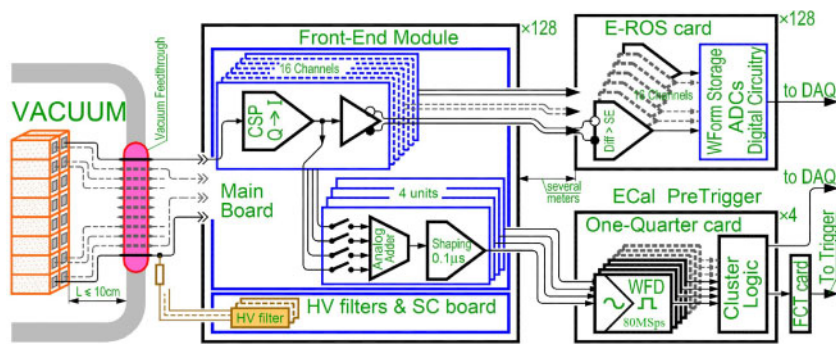
**Table 7.** Characteristics of inorganic scintillator crystals. The superscripts *f* and *s* represent the fast and slow components, respectively.

	GSO(Ce)	LYSO	PWO	CsI (pure)
Density (g/cm <sup>3</sup> )	6.71	7.40	8.3	4.51
Radiation length (cm)	1.38	1.14	0.89	1.86
Molière radius (cm)	2.23	2.07	2.00	3.57
Decay constant (ns)	600 <sup>s</sup> , 56 <sup>f</sup>	40	30 <sup>s</sup> , 10 <sup>f</sup>	35 <sup>s</sup> , 6 <sup>f</sup>
Wavelength (nm)	430	420	425 <sup>s</sup> , 420 <sup>f</sup>	420 <sup>s</sup> , 310 <sup>f</sup>
Refractive index at peak emission	1.85	1.82	2.20	1.95
Light yield (NaI(Tl) = 100)	3 <sup>s</sup> , 30 <sup>f</sup>	83	0.083 <sup>s</sup> , 0.29 <sup>f</sup>	3.6 <sup>s</sup> , 1.1 <sup>f</sup>
References	[77–80]	[81]	[82]	[81]

that it becomes close to the shape of the input signal. The peaking time of the output signal is about 15 ns, and the falling slope is exponential, with the decay time constant equal to that of the LYSO. In this way, noise levels are kept low and the signal pileup is minimized. These full-bandwidth differential signals are transported to EROS boards for sampling. The EROS board is similar to

**Table 8.** The characteristics of the APD, Hamamatsu S8664-1010 [83].

Type	S8664-1010
Active area ( $\text{mm}^2$ )	$10 \times 10$
Package size ( $\text{mm}^2$ )	$14.5 \times 13.7$
Spectral response range (nm)	320–1000
Peak sensitivity wavelength (nm)	600
Quantum efficiency at 420 nm (%)	70
Breakdown voltage (V)	400
Nominal gain	50
Typical dark current (nA)	10
Maximum dark current (nA)	100
Terminal capacitance (pF)	270

**Fig. 62.** A schematic of the ECAL readout electronics.

the ROESTI board (described in Sect. 6.2), but differential-to-single-ended signal converters are connected to the inputs. For the trigger, analogue signals from each block of  $2 \times 2$  crystals are summed up by an analogue adder (in the front-end cards), and the summed signal is then shaped. All summed signals are then fed to the pretrigger. The number of trigger cells in the full ECAL will be too large to be processed in one module; therefore, four identical pretrigger modules will be used, each of which will process the signals from one quarter of the crystal matrix. The latest prototype of the electronics is designed so that it has the same structure as above and improved noise performance, and has the appropriate form factor for the ECAL mechanical design. To confirm the expected performance, a beam test was carried out and the results are described in Sect. 6.3.3.

### 6.3.2. Module, readout, and mechanical structure

The basic unit of the ECAL is a  $2 \times 2$  crystal matrix module with 480 modules to cover the full cross section of the detector region.

A prototype module is shown in Fig. 63. The current design of the module structure for the ECAL is shown in Fig. 64 and the details of the one-crystal structure are shown in Fig. 65. A polished crystal is first wrapped by a reflector film (3M ESR) together with a silicone rubber optical interface (ELJEN Technology, EJ-560) and a PCB on which the APD (Hamamatsu S8664-55 APD, similar to but smaller than the S8664-1010) is attached. An LED with a wavelength similar to that of the LYSO scintillation photon (420 nm) is also placed on the PCB and is used to flash light for monitoring purposes. This one-crystal structure is then wrapped by a layer of Teflon tape from Saint-Gobain.

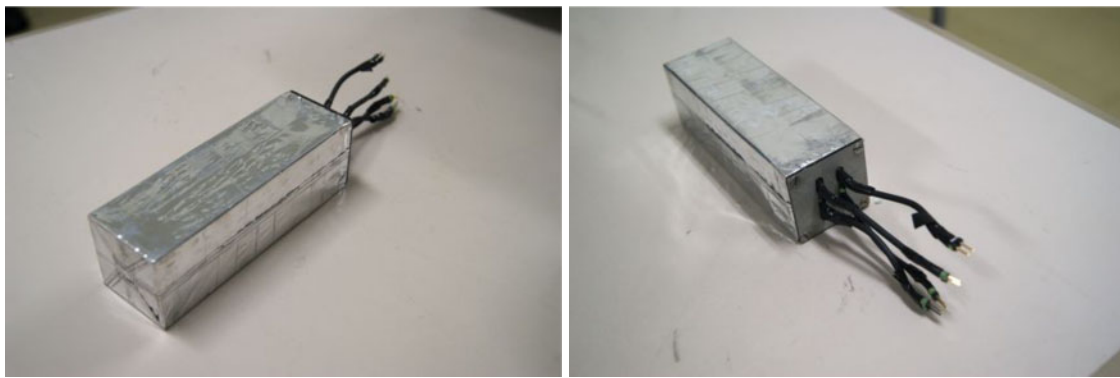


**Fig. 63.** A prototype of the  $2 \times 2$  crystal matrix module (without the preamplifier board).

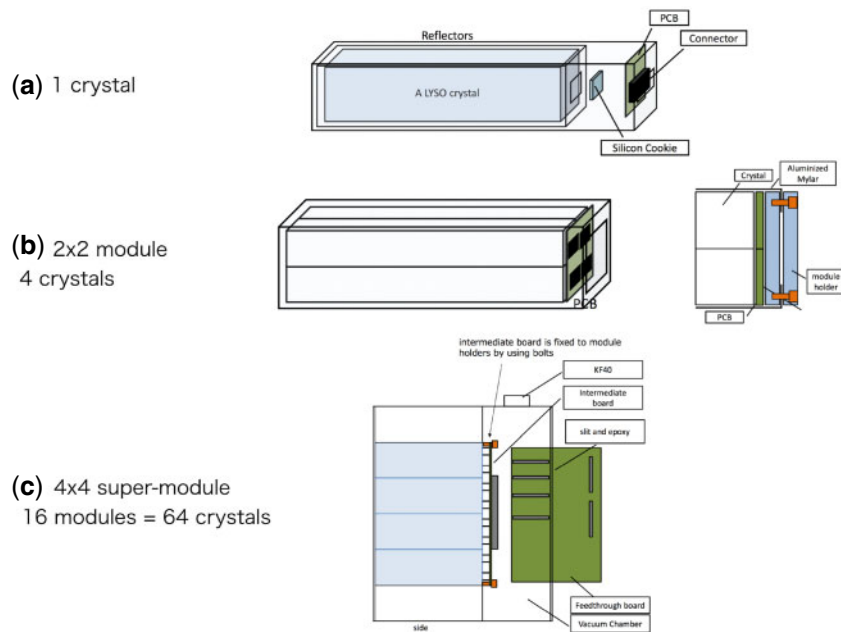


**Fig. 64.** The module structure in the ECAL. (a) 1 crystal + 1 APD on PCB, (b)  $2 \times 2$  crystal matrix module, (c) super-module consisting of  $4 \times 4$  modules (= 64 crystals) and feedthrough.

Four wrapped crystals are then used to construct the  $2 \times 2$  matrix module, which is wrapped by an aluminized Mylar film. The modules are further arranged to form a super-module (Fig. 64(c)).

### 6.3.3. Prototype studies

The first ECAL prototype was tested in a 65–145 MeV/c electron beam at Tohoku University. It consisted of  $7 \times 7$  crystals with 7 preamplifier boards and the prototype electronics but with the Hamamatsu S8664-55 APD with an active area of  $5 \times 5 \text{ mm}^2$  rather than the currently preferred S8664-1010. The resolution was obtained by converting the signal from each of the 49 crystals to an energy deposit and then the energy deposit for the prototype ECAL obtained with a simple clustering algorithm. Tests were conducted with both GSO and LYSO crystals.

Figure 66 shows the energy resolution as a function of beam energy. The resolution at 105 MeV was  $5.50 \pm 0.02 \text{ (stat)} \pm 0.04 \text{ (syst)\%}$  for GSO, and  $4.91 \pm 0.01 \text{ (stat)} \pm 0.07 \text{ (syst)\%}$  for LYSO. The LYSO crystals are found to meet the required energy resolution of better than 5% at 105 MeV.

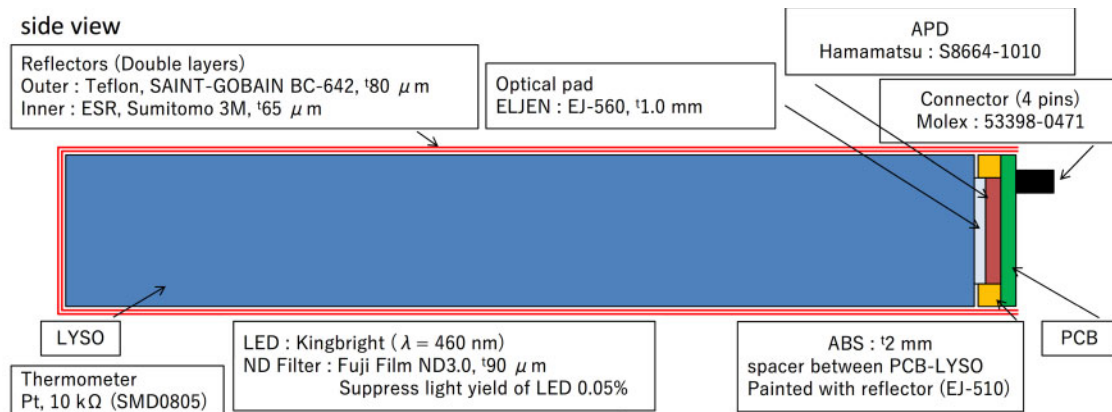


**Fig. 65.** Details of the one-crystal structure.

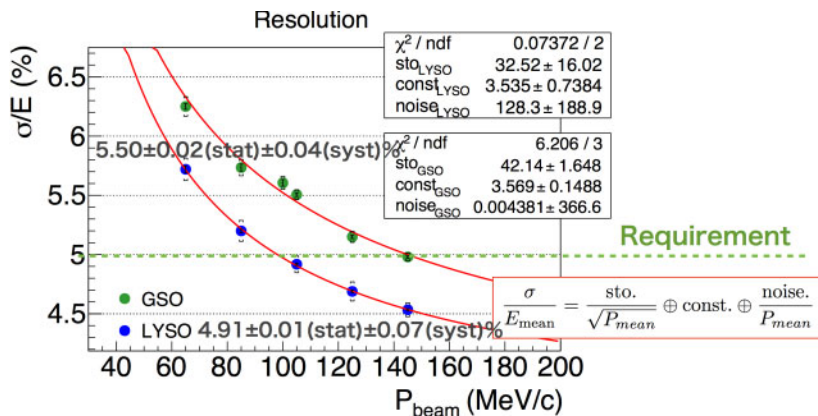


**Fig. 66.** The measured energy resolution as a function of beam momentum.

These preliminary tests also confirmed that both GSO and LYSO could meet the position resolution requirement of less than 1 cm.

Based on the prototype ECAL results in the test experiment, the cost-performance evaluation on GSO and LYSO has been made and our decision of the crystal choice for the ECAL is LYSO.

Achieving the energy resolution and position resolution requirements by using the LYSO crystal in the first ECAL prototype system, further performance improvements have been studied towards the determination of the final design. A second LYSO prototype has been constructed and tested at the GeV- $\gamma$  Experimental Hall in ELPH of Tohoku University. For this the APD used was the Hamamatsu S8664-1010, which has a larger active area of  $10 \times 10 \text{ mm}^2$ , and hence the capability to collect more scintillation photons.

A vacuum chamber was constructed to evaluate the prototype performance in a realistic environment. The prototype modules were installed inside the vacuum chamber together with the intermediate board and the feedthrough board. Figure 67 shows the vacuum chamber and the modules installed in the chamber.

The front-end preamplifier board was redesigned to match the form factor to the ECAL prototype and the noise performance optimized for the larger-area APD.

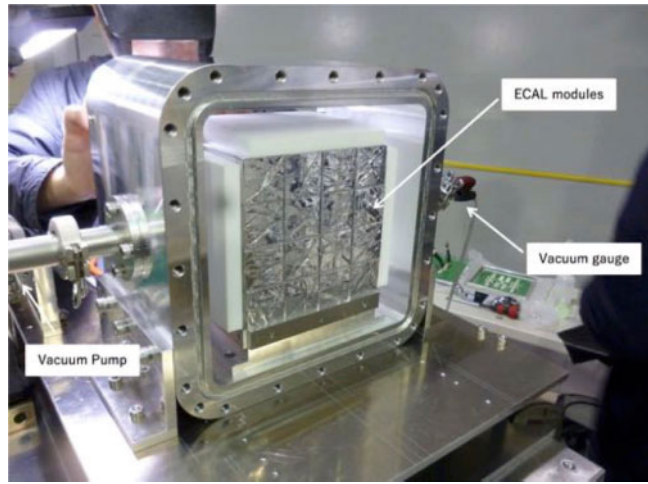


**Fig. 67.** A vacuum chamber for the prototype ECAL system.

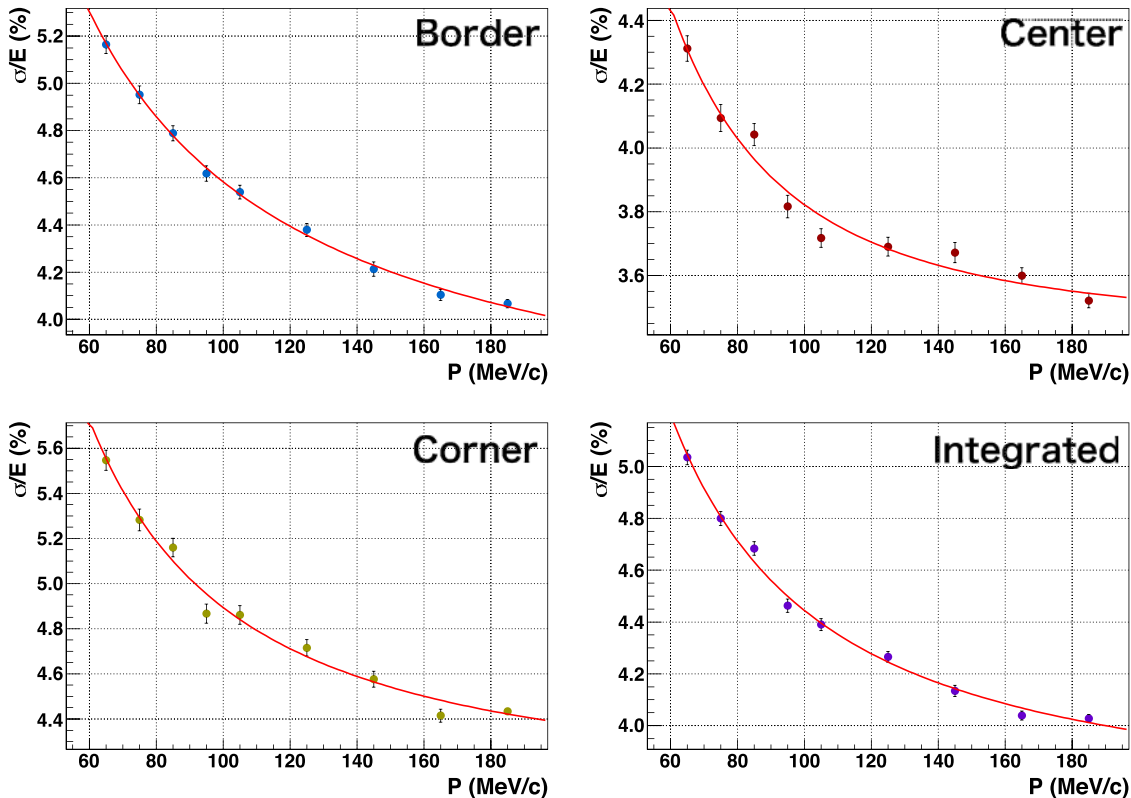


**Fig. 68.** A preliminary result for the measured energy resolution of ECAL as a function of beam momentum. The terms “border”, “corner” and “center” relate to the position of impact—the boundary between two and four crystals, and the center of a single crystal, respectively. (Bottom right) Energy resolution with the position dependence integrated.

The energy resolution and position resolution measurements are shown in Figs. 68 and 69, respectively. At 105 MeV/c, the resulting overall energy resolution is 4.4%, varying from 3.8% to 4.8% depending on where the electron impinges on the ECAL. The overall position resolution is found to be 5.8 mm.

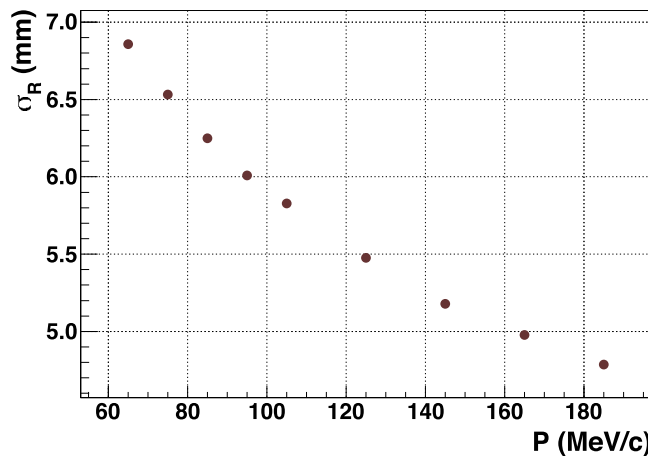


**Fig. 69.** A preliminary result of the measured position resolution of ECAL as a function of beam momentum. Position dependence was integrated in this result.

## 7. Cosmic-ray veto

### 7.1. Physics requirements and general layout

Cosmic-ray muons (CRM) can decay in flight or interact with the materials around the area of the muon stopping target and produce signal-like electrons in the detector region. In order to have control over this background, a cosmic-ray veto (CRV) system is required for COMET (see Sect. 10.5 for cosmic-ray-induced background). The CRV has to identify cosmic-ray muons with an average inefficiency that is lower than  $10^{-4}$ .

For COMET Phase-I, two types of cosmic-ray shielding will be used: passive and active. The passive shielding consists of concrete, polyethylene, and lead, as well as the iron yoke of the DS. The flux of low-angle cosmic particles is also attenuated by the surrounding sand as the detector is located underground.

The active shielding is provided by a CRM detection system covering the CyDet area. Detailed studies of CR-induced backgrounds in Sect. 10.5 indicate that the bridge solenoid (BS) area must also be covered by a CRV, because interactions of CRM in the BS could produce electrons that scatter off the BS and enter the CDC, hit the cylindrical trigger hodoscope (CTH) and mimic signal events. A suppression factor of  $10^4$  is needed for this CRM background and it is obtained by using—in the offline analysis—the signature left in the CRV by the CRM. The active veto system covering the CyDet is made of scintillator-based detectors, whereas glass resistive plate chambers (GRPC) are envisaged in the BS area.

### 7.2. Scintillator-based cosmic-ray veto design

The CyDet CRV has four layers of active material. Its basic element is a strip made of a polystyrene-based organic scintillator. This detector is called the scintillator-based cosmic-ray veto (SCRV).

*Scintillator and light transport* The principle for particle detection and the general design of a single SCRV channel are shown in Fig. 70. The single scintillator strip has a cross-sectional area of  $0.7 \times 4 \text{ cm}^2$  and a length up to 360 cm. It is made of polystyrene (Styron 143E) acting as ionization and photon carrier medium with 2% scintillating fluors (p-terphenyl) and 0.05% POPOP.

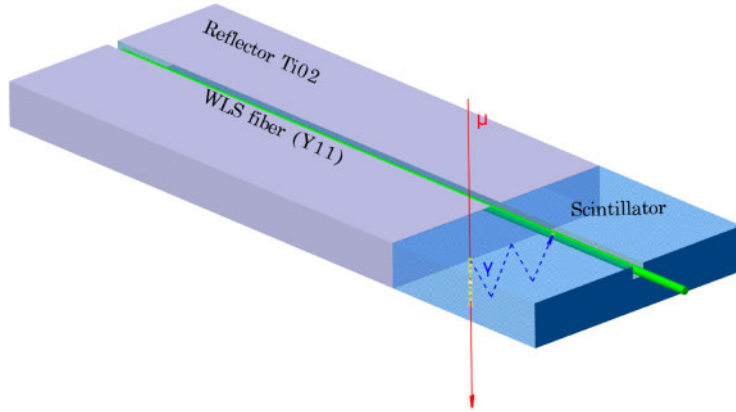


**Fig. 70.** A sketch of the design for a single channel and the principles of particle detection.

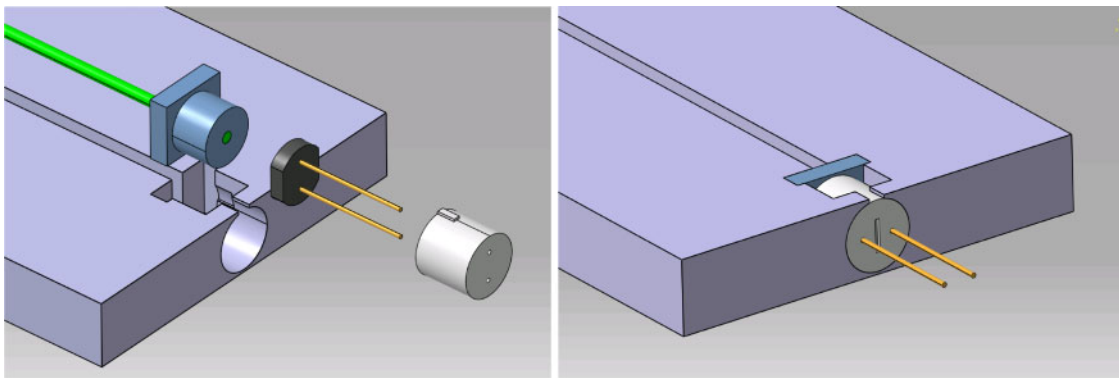


**Fig. 71.** One of the baseline designs for the coupling mechanism of SiPM to WLS fiber.

SCRV strips are read out by wavelength-shifting (WLS) fibers that transport light to the photodetectors. The use of WLS fibers is necessary in order to compensate for the short attenuation length of the scintillators and to optically connect the scintillators to the photodetectors. The WLS fiber is placed along the strip length in a surface groove (see Fig. 71) of a rectangular shape. Several different groove dimensions have been studied and the optimal one was determined to be  $1.5 \times 3.5 \text{ mm}^2$ . A good optical coupling between the scintillator strip and the WLS fiber is ensured by the use of a highly transparent optical glue, BC600 (Bicron optical cement).

Several different fiber types from Bicron and Kuraray have been investigated and the preliminary choice is the 1.2 mm diameter, multi-cladding fiber from Kuraray (Y11), which delivers a high photon yield to the photodetector. The fibers shift the blue scintillation light to wavelengths between 470 and 570 nm. This not only improves the attenuation length significantly, but also brings the light signal into the green range where the quantum efficiency of modern photodetectors is much larger with respect to blue light.

The WLS fibers are read out by silicon photomultiplier (SiPM) detectors at both ends. The double-ended readout design allows one to determine the muon impact point along the strip with an accuracy of a few cm, by measuring the time difference between the SiPM signals, or by measuring the difference in the light yield at both ends. Consequently, the required spatial accuracy of a few cm is achieved without introducing longitudinal segmentation. As CDC will be able to provide much better tracking of cosmic muons, this spatial CRV resolution is enough. Special plastic connectors

**Table 9.** Comparison of the light yields measured for the different samples considered in the R&D studies.

Sample design	Light yield (au)
1.5×1.6 mm <sup>2</sup> groove	194.5
1.5×3.6 mm <sup>2</sup> groove	220.1 (+13%)
1 WLS	194.5
2 WLS	243.3 (+25%)
3 WLS	267.3 (+10%)
BC408	194.5
UniPlast	124.6 (-46%)
TiO <sub>2</sub>	111.6%
AluMilar	124.4 (+11%)

**Fig. 72.** CRV strip layout.

housed in carefully designed receptacles at the ends of the strips (see Fig. 71) couple the SiPM to the WLS fiber.

The results of R&D measurements that were made for material selection are summarized in Table 9. In the baseline design, BC-600 optical cement will be used to glue Kuraray Y11 fibers in the grooves, with one fiber for each strip, which will have a TiO<sub>2</sub> reflective coating. During the design selection, two strip designs have been considered: the current one described above and a wider strip that is read out by several parallel WLS fibers. The narrow strip design with a single fiber was chosen since it has the following advantages:

- Light from a MIP is not shared between different SiPMs, resulting in a very high efficiency even with a high signal threshold.
- The efficiency of each strip can be measured using coincident signals recorded in other strips.
- In case of problems with one channel only a small part of the detector is affected.
- A time resolution of about 1 ns can be achieved.

*SCRV modules and layers* 15 strips form an SCRV module of dimension 0.7×60×300(360) cm<sup>3</sup>. The relatively low weight of the SCRV module of about 10 kg gives it good handling properties. Strips are accurately placed on a 0.6 mm thick aluminum sheet, which is covered with double-sided adhesive tape on the strip side. After placing the strips next to each other, they are tightly glued onto the aluminum sheet. The mechanical encapsulation of the module is obtained by using another sheet as a cover (see Fig. 73). The mechanical strength of the module is given both by the strips being glued together and by the aluminum sheets enveloping it.

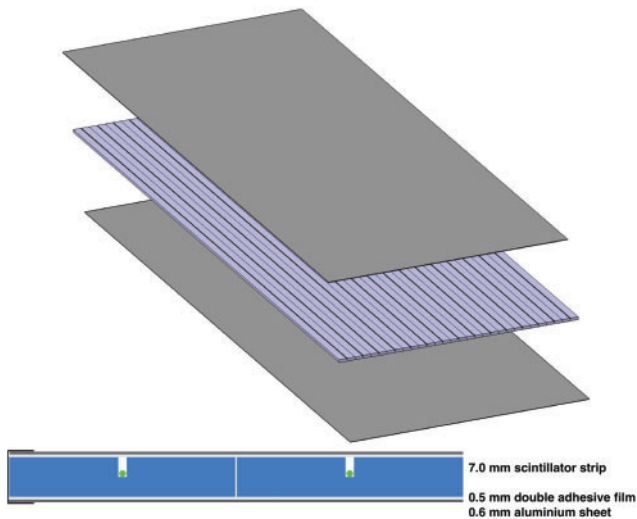


**Fig. 73.** Design of the SCRV module (top). SCRV module cross section (bottom).

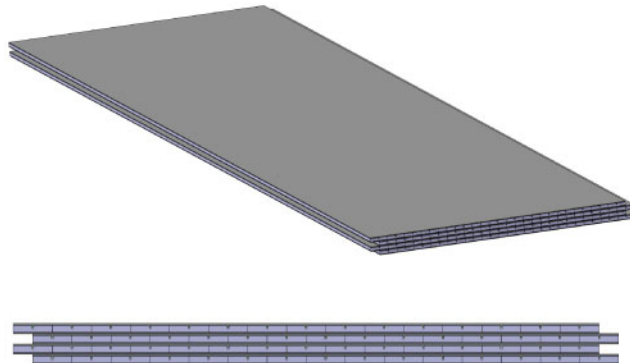


**Fig. 74.** SCRV layer (top) and its cross section (bottom).

The short sides that run along the module are physically protected by a thin, U-shaped, stainless-steel layer that is glued to the aluminum sheets on both sides. The steel mechanical envelope also shields the strips from external light sources.

Modules are placed side-by-side in order to form an SCRV layer. The cosmic-ray rejection power of the SCRV is ensured by deploying four successive detection layers. The modules are shifted by 2 cm from layer to layer in order to avoid the vertical alignment of gaps between strips, as well as between modules (see Fig. 74). 4600 strips are needed to cover the required space.

**Neutron shielding** The neutron flux in the experimental hall can cause problems for the cosmic veto system by inducing noise and causing radiation damage to the SiPMs. The neutrons originate from the pion production target (above 1 MeV) and the beam dump (below 1 MeV).

The dark current of the SiPM increases for irradiation above  $10^8$  neutrons/cm $^2$  [84]. However even after  $7 \times 10^{11}$  neutrons/cm $^2$  irradiation [84], the decrease in the SiPM gain does not exceed 50% and the overall detector efficiency can be retained by adjusting the threshold. It has been shown that operating with a threshold level above seven pixels maintains the fraction of deadtime at the few-% level. At the same time, the muon detection efficiency is still 99.99% when operating with an

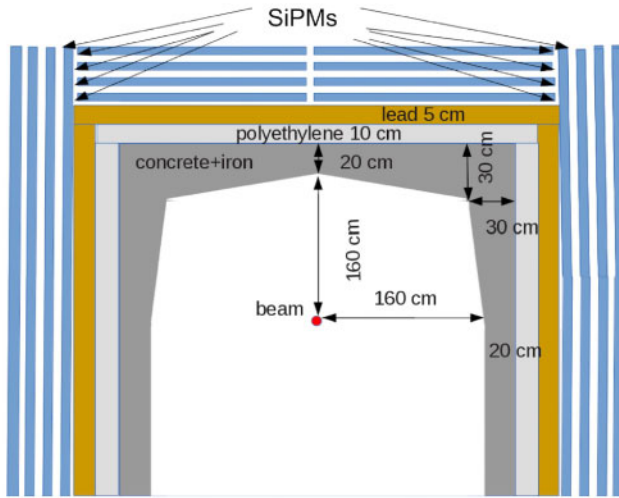


**Fig. 75.** CR veto inner shield with an arched shape (not to scale) showing the readout (in this case SiPM) locations.

11-pixel threshold. The noise and the neutron detection efficiency are both lower when operating at high thresholds, resulting in a smaller deadtime.

To reduce the neutron flux in the scintillator and the damage they induce on the SiPMs, an inner shield will be employed using layers of iron, polyethylene, and lead. The baseline configuration of the shield is an arched shape as shown in Fig. 75, consists of 20 to 30 cm of an iron–concrete mix, 10 cm of polyethylene, and 5 cm of lead, and will reduce the flux of fast and more energetic neutrons at the photodetectors by two orders of magnitude.

The fraction of fast neutrons ( $E \geq 1$  MeV) in the spectrum is larger for the back and front sides, at 44.8% and 24.6% respectively. Optimization of the shielding is ongoing to reduce the fluxes and the fraction of fast neutrons to avoid worsening photodetector efficiencies over the full period of data taking.

### 7.3. BS-area CRV

The region around the BS that requires active shielding has a surface of  $3 \times 1900 \times 600$  mm<sup>2</sup>. Simulations indicate that this area suffers from a larger neutron contamination compared with that affecting the CyDet CRV.

GRPCs are a natural candidate for operating in such high neutron flux areas; they can be built to the required size and provide a uniform tracker, without dead areas between adjacent active volumes. Moreover, their segmentation can be easily modulated to fit the required tracking performance on muons. The baseline design is based on single-gap (1.2 mm thick) chambers (Fig. 76), operated in avalanche mode. These are thin detectors of less than 3.6 mm, with nanosecond time resolution, operated at average efficiencies of 95% and with an intrinsic position resolution of a few mm. The design envisaged for COMET is based on R&D performed for the detectors for the International Linear Collider [85] and used since 2012 for muography studies [86].

The BS CRV is based on three trackers to be deployed on the top and the sides of the BS respectively. Each tracker is made of six GRPC modules as represented in Fig. 77. Two single-gap GRPCs housed in an aluminum honeycomb structure share a centrally placed readout layer. The readout layer is made of two adjacent PCBs, double-layered, with  $X$  strips on the upper layer and  $Y$  strips on the lower layer.



**Fig. 76.** Single-gap GEM made of two layers of float glass, glued together using 1.2 mm PEEK spacers. On the outer part of the glass sheets, resistive paint (graphite-based) is used to apply an electric field of about 6.5 kV/mm across the gap. A mixture of a gas with high fluor content (forane) and a quencher ( $SF_6$ ) at a ratio of around 98:2 is flushed permanently through the chamber at a low rate of about 15 cc/min.

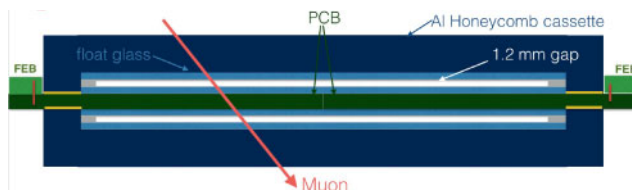


**Fig. 77.** A GRPC module made of two single-gap GEMs housed in a unique aluminum honeycomb cassette and sharing an XY readout layer. To make possible its outsourcing, the readout layer is made of two individual  $60 \times 95 \text{ cm}^2$  PCBs; these are double-layered and have orthogonal readout strips on the outer faces. Each GEM-resistive layer closest to the readout layer is grounded and the second one is used to apply the polarization high voltage. The strip signals are read on one side using mezzanine boards labeled FEB in the figure. The figure is not to scale horizontally.



**Fig. 78.** A front-end board, developed for ALICE, housing the FEERIC ASIC in the center of the board. At the top, the eight pins connecting the readout strips (designed for 4.5 cm readout strips in this case) are visible. The four pins on the bottom of the picture are for grounding. The board shown is 32.5 cm long and 5 cm wide, but the final dimensions will be determined by the optimal BS-CRV segmentation.

This leads to 60 cm-long strips in one direction and  $\sim 95$  cm in the other, with single-end readouts. This design of two single-gap GEMs is commonly used in high-energy physics experiments and increases the efficiency of each module from 95% to 98%.

The readout chip in the baseline design is the FEERIC, developed for the ALICE experiment at the LHC [87]. It is an eight-channel, double-polarity chip with a LVDS output that can handle charges varying from 20 fC to a few pC. The chip is housed on a front-end board (FEB) developed for ALICE and mounted as a mezzanine on the readout PCBs (Fig. 77). One such FEB, designed for 4.5 cm readout strips, is shown in Fig. 78. It allows the remote setting of the data-acquisition thresholds for the ASIC through an I<sub>2</sub>C connection, and testing and calibration of the electronics using a charge injection mechanism. The output signals, in LVDS format, are fed into a local DAQ board that communicates with the COMET clock and trigger system. It also implements a local trigger, based on coincident signals recorded in several GEM modules.

Depending on the optimal segmentation for the BS CRV, which is still under study, the total number of FEERIC chips per GEM module will be between 78 (4.97 mm readout strips) and 8 (48.44 mm readout strips).

As in the case of the scintillator CRV, an inner shield will be deployed to reduce the beam-induced radiation on GEMs.



**Fig. 79.** (Left) FC7 board developed for the CMS experiment and adopted as the central trigger processor board in the COMET trigger system. An FPGA for trigger processing and board control is located at the center, and two commercial mezzanine cards for connecting subdetector trigger system are mounted on the right side of the board. (Right) Custom-designed FCT board for interfacing with the FC7 board.

## 8. Trigger and DAQ

Phase-I will have two distinct running modes, one with the StrECAL as main detector to measure backgrounds and characterize the beam and the other with the CyDet as main detector to search for  $\mu^- N \rightarrow e^- N$ . There will be distinct but similar DAQ and trigger systems for the two modes. Detectors such as a beam monitor and an X-ray monitor (to determine the muon beam profile and number of muons captured in the target, respectively) will be employed for both modes. Similarly, the CRV will provide a veto whilst running with beam (which can be applied offline), but can also provide a calibration trigger.

Each system consists of six main parts:

- The fast control system, which distributes a common 40 MHz clock and all the time-critical signals, such as triggers, to the detectors in each system.
- The trigger system, which determines when to read out the detectors. This is distributed with a fixed latency.
- The readout system, which transfers the event data from the detectors to disk when a trigger occurs.
- The configuration system, which transfers data to the detectors to set parameters to control their performance.
- The online software, to operate the system.
- The slow control and monitor system.

### 8.1. Trigger systems

The fast control and trigger systems are composed of: the FC7 board (left figure of Fig. 79) developed for the CMS experiment at the LHC [88] as a central trigger processor; the FCT (fast control and trigger) custom-designed board (right figure of Fig. 79) to interface between the central systems and the subdetector trigger or readout components; and a custom multi-gigabit transceiver (MGT) protocol connecting these systems. While the subdetector trigger system for CyDet and StrECAL are different, the core parts share the same system mastered by the FC7 board.

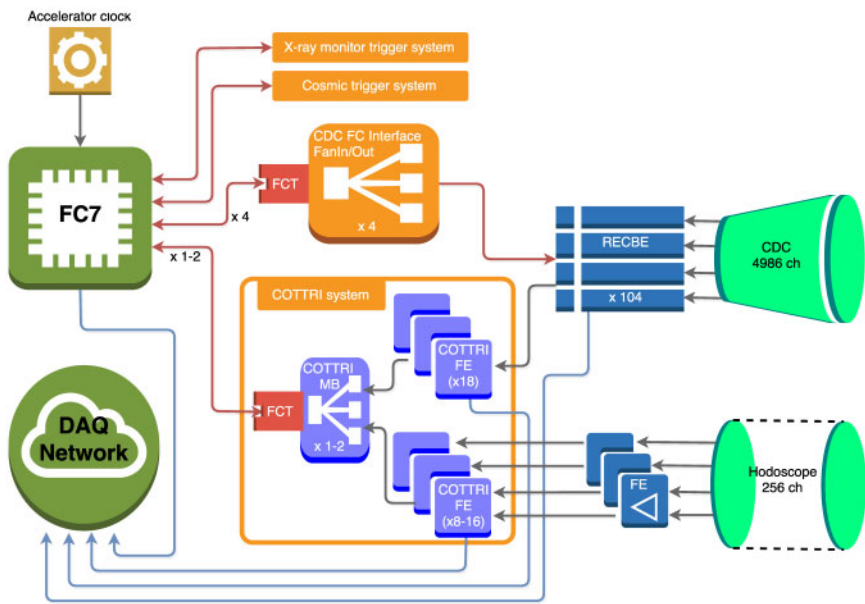


**Fig. 80.** Block diagram of the CyDet fast control and trigger systems.

#### 8.1.1. The CyDet trigger

A schematic of the CyDet fast control and trigger systems is shown in Fig. 80. The main trigger when operating in CyDet mode is provided by requiring four-fold coincidence on neighboring counters from the CTH detector. This is supplemented by using the track patterns from the CDC hits as these are quite different for high-momentum electrons (signal or DIO) than the low-momentum particle noise hits. For the CyDet component a simple combination of hit pattern and energy deposition can yield a sufficiently fast trigger with high efficiency and background rejection power, resulting in an overall trigger rate of a few kHz.

*The COTTRI system* The COTTRI system provides the main logic for the CyDet trigger. It is divided into front-end boards (COTTRI FE) and a mother board (COTTRI MB), as shown in Fig. 81. The COTTRI FE boards perform the initial processing of the analogue or digital inputs and then the COTTRI MB combines the signals to generate the higher-level trigger that is sent to the central trigger system and distributed to the detector readout system. The logic for the combination algorithm resides in the FPGA on the COTTRI MB.

12 COTTRI FE boards will be required to process the CTH signals. The analogue signals are first amplified and digitized and then the FPGA discriminates them and sends a digital trigger signal to the MB. They will be located inside the CTH support structure and, therefore, a radiation hard design is necessary.

For the CDC application 18 FE boards will be required to process the 104 RECBE board trigger signals where the digitized hit information will be multiplexed and sent to the MB. These boards will be located inside the CDC readout box.

The proposed trigger algorithm using COTTRI will use the CTH-provided trigger to search for CDC wire hits near the CTH hit and count the number of CDC hits in that region. A simple track reconstruction can also be performed using these CDC hits. Based on these features, the COTTRI system makes the trigger decision and sends it to the central trigger system with the relevant CTH and CDC hit information.

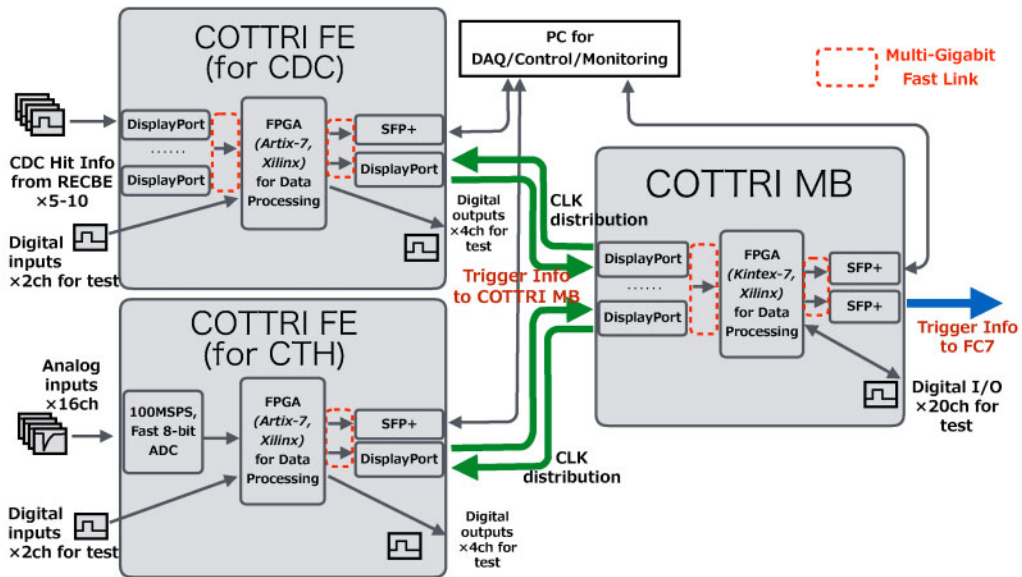


**Fig. 81.** Conceptual drawing of the COTTRI system.

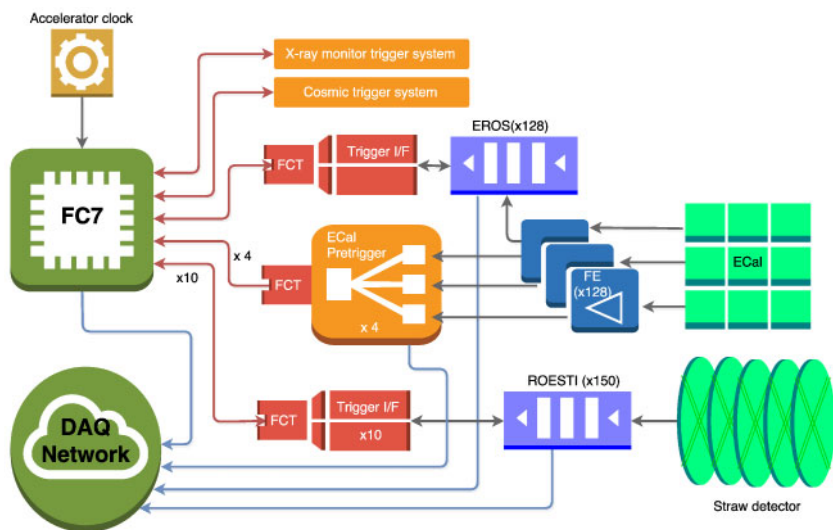


**Fig. 82.** Block diagram of the StrECAL fast control and trigger systems. Note that, in the Phase-I experiment, the number of channels of ECAL will be smaller than Phase-II; therefore, the number of pretrigger boards is also smaller than this diagram.

### 8.1.2. StrECAL trigger

In the StrECAL mode (right figure of Fig. 82), the trigger is provided by the ECAL. The energy deposition from a single track can be divided among several crystals and so a summation is necessary to reconstruct the full energy. The summed energy over crystals that form a  $4 \times 4$  square can effectively include almost all the energy deposited by electrons with energies of about 100 MeV. The basic trigger unit (cell) will therefore be a group of  $2 \times 2$  crystals (one ECAL crystal module), and the total energy is determined by using the sum of an array of  $2 \times 2$  trigger cells, referred to as a trigger group. The effectiveness from simulation is shown in Fig. 83 with at least a  $10^6$  DIO rejection for around a 90% conversion electron detection efficiency.

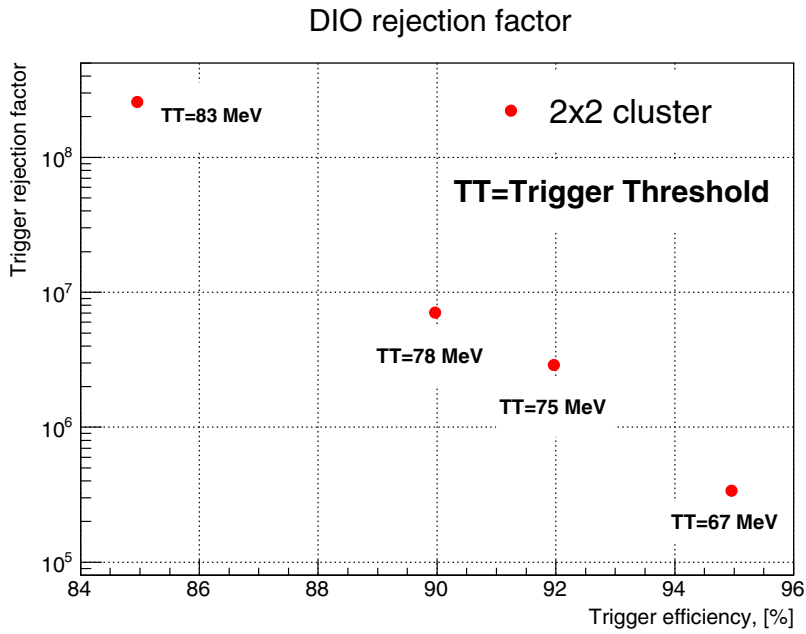


**Fig. 83.** DIO rejection versus CE trigger efficiency on various energy thresholds or ECAL pretrigger energy summations.

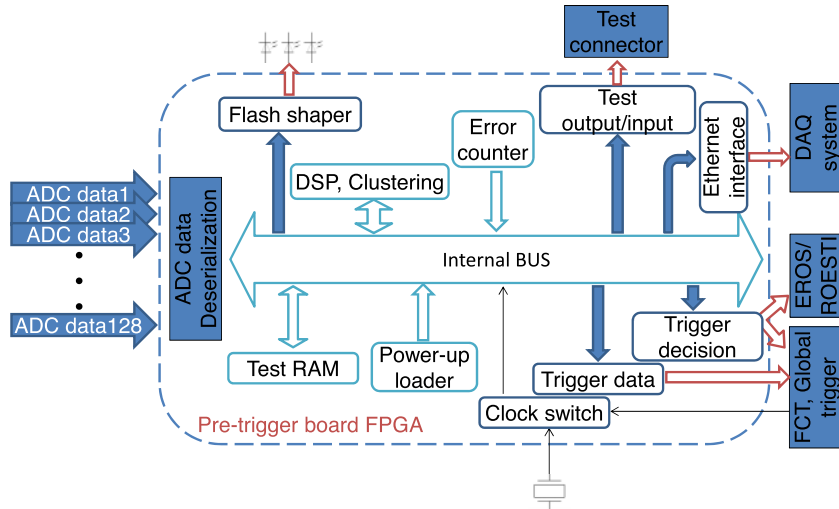


**Fig. 84.** A conceptual drawing of the FPGA functionalities of the ECAL pretrigger board.

The structure of the ECAL electronics system is shown in Fig. 62. The signal from each trigger cell is formed by analogue-summing the preamplifier outputs and hence 16 signals going to the digitizing readout and 4 signals to a dedicated pretrigger board.

**ECAL pretrigger board** The ECAL pretrigger boards digitize the analogue signals from the trigger cells and pass the resulting waveforms through filters in an FPGA. The conceptual design of the FPGA logic is shown in Fig. 84.

Four trigger cells are summed in all possible combinations of such trigger groups. From these possible combination of pretriggers, the group with the largest energy is found, and the size of this signal is sent, together with the group number, to the FC7 for a final decision to be made.

The energy resolution of the ECAL pretrigger system is measured as 4.5 MeV for 105 MeV electrons, which is sufficient for trigger performance.

To avoid any inefficiency at the edges of crystal coverage (a quarter of ECAL), digitized data of 12 trigger cell located at one edge of a quarter of ECAL are transmitted to the next board. The pretrigger board also contains an Ethernet connection to control a PC, so that the board can be controlled and monitored independently, along with control and monitoring through the fast control and timing system.

The ECAL pretrigger boards provide a fast trigger signal but the final decision whether or not to record a particular event is made by the central trigger system. The fast trigger decision is based on energy windows, which can be individually prescaled; e.g., for the signal region there is no prescaling, whereas for the side bands it depends upon the expected background. These are set in the FPGA. If necessary the number of energy windows can be enlarged.

*Other trigger systems in StrECAL* A StrECAL cosmic trigger is also required for tests and calibrations when not running with a beam. It will be based on the cosmic veto system with simple coincidences of hits in different layers of bars close to each other.

#### 8.1.3. Trigger performances

During the prototyping of trigger boards, the maximal trigger rate capacity and the trigger latency are estimated. The final production of those boards and integrated tests with detectors are ongoing.

*Trigger rate* Given a bunch separation of  $1.17\mu\text{s}$ , the maximum rate of interesting events is around 850 kHz. However, the serial data width of the trigger information is 50 bits, and this is returned over the 40 MHz MGT, so the trigger system is essentially dead for  $1.25\mu\text{s}$  when a trigger is taken.

For the CyDet trigger the deadtime introduced by the RECBE board is less than  $1\mu\text{s}$  and hence the actual maximum trigger rate in CyDet mode is 440 kHz, whereas for the StrECAL trigger the ROESTI and EROS introduce a  $36.7\mu\text{s}$  deadtime leading to a maximum trigger rate of 26 kHz. The effective trigger rate is, however, dictated by the DAQ system, which is not greater than 20 kHz.

*Trigger latency* When operating in CyDet mode the required trigger latency is around  $5\mu\text{s}$ , due to the buffer size of RECBE ( $8\mu\text{s}$ ). Currently the processing time in the COTTRI MB is not known; however, the latency from the other components is estimated to be  $1.1\mu\text{s}$  and so the requirement should be comfortably met. In StrECAL mode the limit is set by the EROS board and a conservative target would be 700 ns. However,  $1\mu\text{s}$  latency was measured in the current design, where the main bottleneck was signal encoding and decoding for MGT. It was possible to decrease the latency down to 700 ns by employing a separate faster trigger line from the ECAL pretrigger to EROS, which avoids the MGT encoding and decoding bottleneck.

### 8.2. DAQ system

The DAQ system covers the data transfer from the front-end readout electronics to the data storage, through the event builder. The system mostly relies on off-the-shelf equipment, so the selection of proper equipment meeting the requirement of the COMET DAQ described here is in progress. The DAQ software will be based on the MIDAS framework.

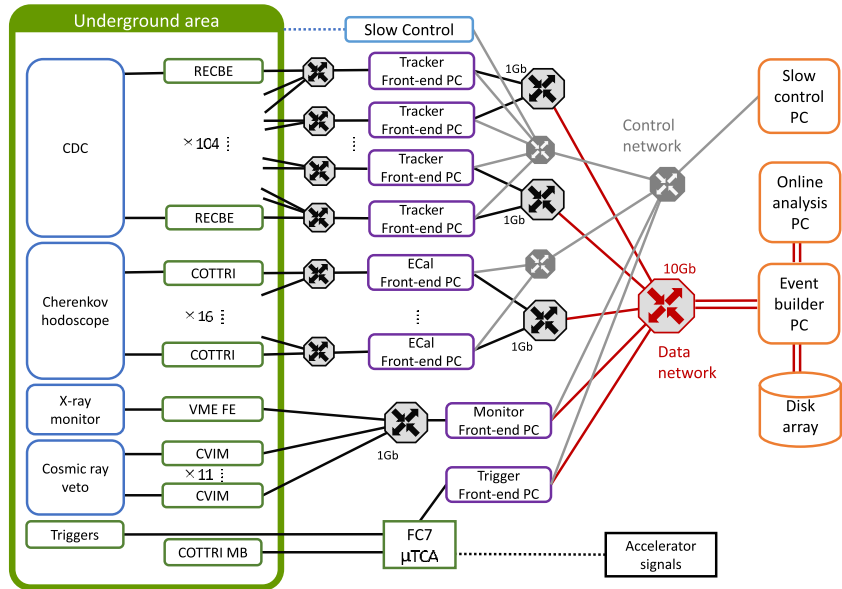


**Fig. 85.** Block diagram of the CyDet readout and configuration system.

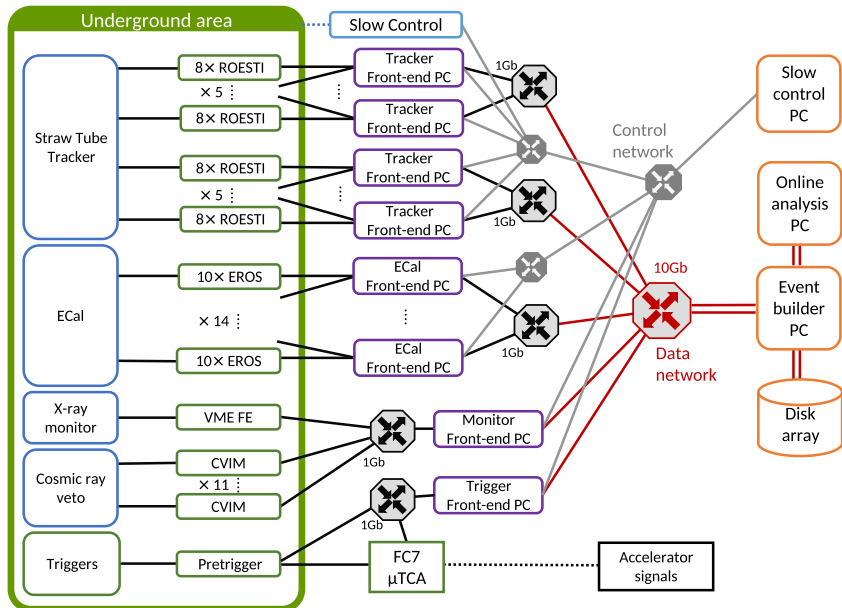


**Fig. 86.** Block diagram of the StrECAL readout and configuration system.

The readout systems for both CyDet and StrECAL modes are similar, employing standard Ethernet networking with commercially available components. The readout and control networks for the CyDet are shown in Fig. 85 and for the StrECAL in Fig. 86.

An event builder PC acts as the run controller and sends commands to start and stop runs, etc. using MIDAS [89] DAQ software control protocols. These commands are distributed via network switches to a set of PCs dedicated to the readout of particular parts of the detectors. Data are transferred on the network using standard protocols (Ethernet, UDP, TCP/IP).

When a trigger occurs, the event data are stored in buffers in the front-end electronics and when the buffer has a whole event it will be sent as a packet (or packets) of data to a PC. Event packing

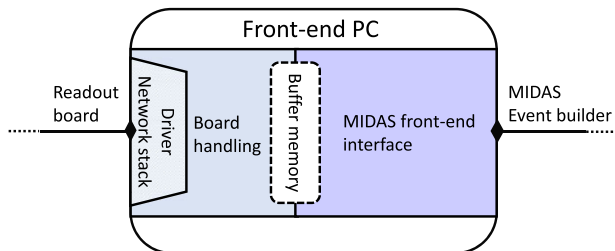


**Fig. 87.** Schematic of a processes running on a front-end PC.

will be conducted in such a way that minimal translation is required. As an illustration, a PC will assert (i.e., send a message to the front-end electronics) “ready for a packet”, meaning it has enough resources available to receive the largest possible packet (and one more). While receiving the packet it can assert/send a “not ready for packet” signal/message and the front-end will continue and finish the current packet, but then wait for an update from the PC. Once the data are collected on a PC all further transmissions are over standard computer networking.

#### 8.2.1. MIDAS front-ends and back-end

The basic unit of readout for the MIDAS DAQ is a single piece of “equipment” that wraps all the activity of a subset of the readout electronics and communicates it back to MIDAS in standard MIDAS format. It also acts as the receiver for MIDAS commands. For the main detectors (CDC, ECAL, and straw tracker) this is accomplished using intermediate PCs designated *front-end PCs*.

Both the ROESTI and the RECBE will communicate with the front-end PCs using SiTCP, an FPGA-based implementation of TCP<sup>11</sup>. The data content of the TCP packets has no special restrictions, and is assembled into an appropriate format by the SiTCP firmware. The front-end PCs can handle multiple boards, receiving data packets from the electronics and decoding them.

The front-end PCs also communicate with MIDAS, responding to commands sent by the DAQ and transmitting readout data to the central event builder PC. These two roles are executed concurrently as threads of the same process on the PC. The non-synchronous devices, such as the X-ray monitor, also can be read in the same structure front-end process, because of the supporting multiple type trigger by MIDAS. A schematic of a basic front-end process running on a front-end PC is shown in Fig. 87.

For the main detectors, the front-end PC also performs a partial event building to reduce the load on the back-end event building and hence increase the performance of the DAQ. This front-end partial event building is a generalization of the basic front-end using several threads.

- Reader. The reader handles the front-end electronics, reads the data, and writes them to an internal buffer.
- Partial event builder. This manages the event fragments from the reader threads with the same trigger number and writes them to a back-side buffer
- Sender. This sends the built event fragments to a MIDAS server on the back-end PC using the MIDAS remote protocol.

A schematic of the partial event building front-end process is shown in Fig. 88.

<sup>11</sup> In addition the COTTRI-FE boards will also use a firmware-based TCP implementation

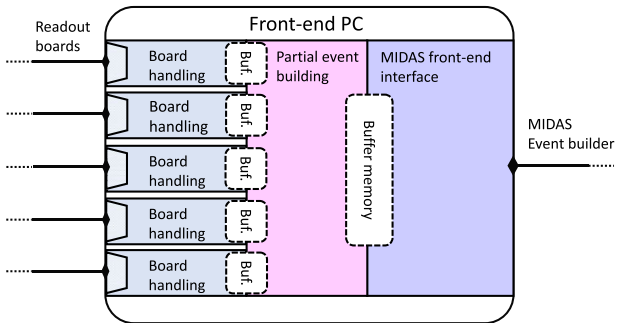


**Fig. 88.** Schematic of the event building front-end processes running on a front-end PC.

**Table 10.** Experiment operating parameters assumed in this section. In most cases these are not fixed and will be optimized. In tests of 8 GeV Slow eXtraction (SX), the accelerator cycle time is 2.38 s, during which each spill lasts around 0.5 s.

Accelerator cycle time	$\mathcal{O}(1)$ s	
Slow extraction duty factor	0.5	
	4 bunch	3 bunch
During slow extraction:		
Normal bunch spacing	1170 ns	1755 ns
Signal window	800 ns	1300 ns
Signal window active fraction	0.68	0.74
Number of bunches extracted	$\mathcal{O}(10^6)$	

The backbone of the data network will be 10 Gigabit Ethernet as it needs to channel data from all of the front-end PCs. The central element of the MIDAS back-end is a PC that runs the event builder process. This requests and collects “fragments” directly from all the front-end systems to a memory buffer, and when all expected fragment are received, it sends the completed event to a logger that is responsible for writing the event to disk. The PCs for the online analysis copy the event data from the event building PC via a direct connection and distribute them to several types of analytical processes. There will be 100 TB class storage on the local site and then the experimental data will be transferred to the primary data archive provided by KEK computing in Tsukuba using the 10 Gbps Tsukuba–Tokai network.

### 8.2.2. Data rates

Both detector systems need to operate assuming the accelerator is operating continuously for an indefinite period of time. However, as the beam is not continuous, peak rates are higher than the time-averaged rates. While the electronics needs to operate at the peak rate, buffering allows the higher levels of the DAQ to operate at a lower average rate. The operating parameters assumed in the following section are shown in Table 10. At present the four-bucket mode is used for data rate estimates.

*For the CyDet* The basic trigger rate for the CTH is about 26 kHz. Even with the shielding the rate is still mostly due to low-energy particles. Using the CDC hit information, this can be reduced to a more manageable 1.3 kHz.

Signal-like triggers (from the high-energy tail of DIO) should pass the high-level trigger with probability close to 1, and as such represent a minimum floor for the online readout rate. Older simulations that do not incorporate the latest software developments suggest a rate of a few hundred per second. The CDC imposes a minimum threshold momentum for electron tracks to be observed of at least  $70 \text{ MeV}/c$ , and the rate of DIO electrons above  $70 \text{ MeV}/c$  is around 600 Hz. Summing both triggers from background and signal-like electrons, an overall trigger rate of around 2 kHz is estimated.

The event sizes for the CyDet are calculated assuming the existing *Suppress[ed]* readout of the RECBE boards (including a high-charge cut-off) is used. This is based on a Belle-II mode that essentially corresponds to reading out an integrated ADC value and time stamp for channels above some zero-suppression threshold.

The data volume per trigger assumes an occupancy of 20% out of around 5000 sense wires, corresponding to  $\sim 1000$  hits in a signal window. However, the majority of these hits will be eliminated by the high-charge cut leading to an estimate of around 3.5% channels to be read out and consequently about 200 hits in the signal window. Because the drift time in the CDC is projected to be around  $0.4 \mu\text{s}$ , it is necessary to consider a coincidence timing about as large as the signal window, so there can be no significant reduction from applying a trigger window. Overall, in the Suppressed mode, it is estimated that the CDC gives 1.7 KiB per trigger.

For the trigger hodoscope readout the readout window does not need to be as wide as for the CDC, as there is no drift delay; however, in initial running it will be useful to retain the CTH information from the entire readout period, which is approximately  $1 \mu\text{s}$ . In this case, the most efficient readout format is fixed ordering. The data for each counter would consist of a one-byte “header” indicating how many hits were recorded followed by the same number of TDC–ADC pairs. In this scheme, the total data readout would be approximately 2.5 KiB ( $= 256 \times 1$  header bytes +  $800 \times 3$  TDC–ADC bytes), which is a substantial contribution to the overall event size. Once experience is gained the CTH readout window could probably be reduced to a few tens of nanoseconds around the trigger time, which would reduce its contribution below 1 KiB.

*For the StrECAL* The event sizes are larger but the trigger rate is lower, and it can be more easily tuned in the run configuration by adjusting the energy threshold of the trigger logic.

For both detector configurations, a variable trigger prescale will also be implemented, allowing some fine tuning of the rates and a busy mechanism will provide the ultimate guarantee of a maximum data rate.

#### 8.2.3. Online software

MIDAS [89] will be used for the DAQ software, which will be made of several distinct parts. Front-end PCs will run detector-specific programs to read directly from the hardware and asynchronously send packed data to the back-end PC using MIDAS RPCs (remote procedure calls) to store the data in the form of MIDAS banks.

The back-end PCs will run the following:

- An event builder to combine the MIDAS banks from several front-ends into a single MIDAS file.
- An “online converter and monitor” to convert the data into ROOT format and produce histograms for live monitoring and offline analysis.

- A “logger” to write the MIDAS data to disk.
- A “run control” program to start, stop, and monitor runs.

Most of these programs will be implemented within COMET’s ICEDUST software framework that has the benefit of being based on the T2K-ND280 framework, which also uses MIDAS, and as such already has libraries to perform these transformations.

Data monitoring will take place on a separate dedicated PC that will run the online conversion and monitor program to read the data on disk (in MIDAS format), convert to ROOT format, and produce standardized plots for detector status monitoring. This incorporates libraries that allow access to the information in the files directly from ROOT. The offline event display (albeit with preliminary alignment and calibration constants) will also be used for online monitoring through this mechanism.

#### 8.2.4. *The radiation environment*

The RECBE board for CDC readout will be located inside the detector solenoid and be affected by the radiation, especially neutron radiation. Therefore, understanding the radiation environment around the RECBE board and preparing for the possible DAQ situation that may arise due to the radiation effect is very important.

The effect of neutron radiation on the FPGA and its firmware and mitigation efforts in the COMET Phase-I experiment are reported in Ref. [62]. Most single-event upsets due to radiation will affect the transient data that can be isolated in the offline process, while they may sometimes lead to FPGA firmware malfunctions. In this FPGA malfunctioning case, the DAQ and front-end hardware can be restarted, which will result in a long deadtime when it happens with a high rate.

*Gaps in the data stream* The RECBE FPGA firmware and DAQ are designed so that they can be reloaded in the case in which the FPGA is not recovered automatically from the effect of radiation. Again, this reloading is triggered automatically by DAQ; however, a few seconds of gap in the data stream are unavoidable. This will be handled in the central event builder process, so that the event building will be completed without a missing fragment of data stream when the fragment buffer remains empty for a specific timeout period. When the RECBE board is rebooted and resumes the sending of event data, the event builder will realign this buffer with the remainder of the detector using the trigger number.

*Loading of runtime parameters* It is likely that the RECBE will need to reload various configurable parameters after a firmware upset. To reinitialize the run, the parameters will be cached on the front-end PC at the run start, and the relevant parameters will be provided when requested by the RECBE.

## 9. Offline software and physics analysis

The main software suite that is in use by COMET is called ICEDUST (Integrated Comet Experimental Data User Software Toolkit). Below we describe ICEDUST and its use in analysis work in preparation for Phase-I.

### 9.1. *ICEDUST framework*

For the calibration, reconstruction, and analysis of data from COMET Phase-I, it is essential to have an offline software framework that treats this data in the same way as for simulated data. Since the

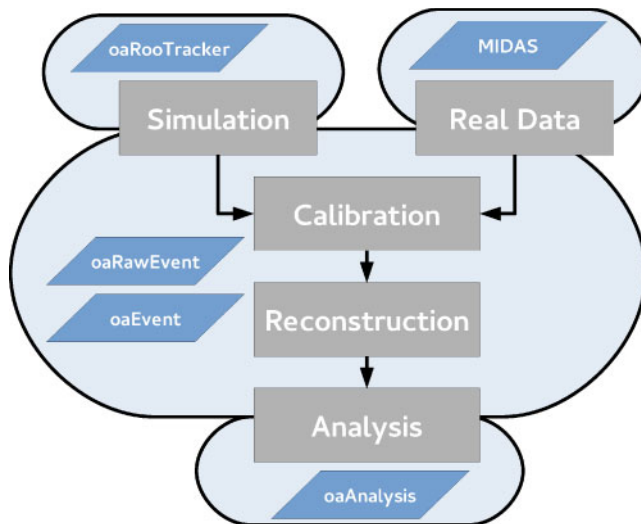


**Fig. 89.** An outline of the ICEDUST framework. The larger blue regions represent parts of the framework that share a common data format, which is specified in the parallelogram.

development and testing of a new framework is a significant undertaking, it was decided that the COMET framework should be based upon an existing framework that has been well tested in a real data-taking scenario.

A number of existing frameworks were compared against the requirements of COMET. The framework used for the near detector for the T2K experiment [90] at J-PARC, known as ND280, would be the best choice upon which to develop ICEDUST, as it has already seen several years of data taking and debugging and use in published physics analyses. It also includes a novel interface with the MIDAS online data acquisition system.

The structure and the data flow of ICEDUST are illustrated in Fig. 89. Notably, data from the experiment and the simulation are processed in the same way, following the same steps through the chain. The important components of ICEDUST are as follows:

- Data formatting: The `oaEvent` package provides the event data format both for simulated and real data, as well as the geometry information. The experimental data in MIDAS data format are unpacked to `oaEvent` format.
- Simulation: While Geant4 plays the central role in simulation, any other package can be used cooperatively in generating and simulating events. The simulated data of each proton are collected into a proton-bunch event. The detector responses are applied afterwards.
- Reconstruction: A global reconstruction includes the signal track finding and fitting, and subsequent analysis. This generates simpler event data with the format provided by the `oaAnalysis` package.

The details are described in the following sections.

Significant improvements have been made to the software in recent years, and the physics content of the software is essentially independent between the experiments, given the differences between COMET and T2K ND280. Many of these improvements are now being fed back into the ND280 software.

To ensure that software developed for ICEDUST is done in a consistent way across the collaboration, naming and coding conventions have been defined and followed.

## 9.2. Data formats

The key strength of the approach used is the ability to treat experimental data on such an equal footing as the simulated data. This is achieved in two ways:

- An unpacking mechanism that converts the raw MIDAS data into offline root files.
- A wrapping package that can provide a semi-transparent method to process raw data.

The core event structure of ICEDUST is provided by the `oaEvent` package. Data in the `oaEvent` format are built by a hierarchical structure of objects from the `TNamed` class of ROOT, which provides a stronger memory management policy and avoids the need for global pointers to access the output data hierarchy. Collections of data are stored in a similar manner with the `map` class of the standard template library (STL) of C++.

The description of the geometry is stored alongside the data, either in the form of a hash-tag pointing to a particular archived geometry that is automatically retrieved as needed, or else as a persisted ROOT object. The ROOT format uses the various `TGeo` classes that implement all geometry needs such as navigation, mass calculations, material descriptions, and visualization. This means that all packages throughout the framework use a common geometry description as well as providing an easy book-keeping mechanism.

## 9.3. Simulation

The simulation of COMET has been sub-divided into smaller tasks. The standard simulation chain for production Monte Carlo data is:

- (1) Simulate production target. This is done separately so we can use packages that include different hadron production models.
- (2) Particle tracking in Geant4 (SimG4). Geant4 has a highly optimized tracking algorithm as well as many well tested experiment-based physics models. This package tracks particles from the production target to the various detectors and produces simulated energy deposits.
- (3) Detector response simulation. Energy deposits produced by SimG4 are converted into realistic detector outputs such as ECAL crystal waveforms or CyDet wire hits. Various detector effects such as finite resolution, cross-talk, and random noise can be added here.
- (4) Rare-process selection. Occasionally we may wish to focus a study on one of the rarer signal or background processes. Since this would normally require the simulation of a lot of unimportant processes, a package is being developed to merge hits from rarer processes together to artificially increase their statistics.

Up to truth information, steps 1 and 2 can be done by any of the various external Monte Carlo packages that have been incorporated into ICEDUST. These include Geant4 [55], MARS15 [56], PHITS [91], and FLUKA [92,93]. Figure 90 shows the implementation of this simulation procedure in ICEDUST.

### 9.3.1. Geometry definition

SimG4 is the package tasked with running Geant4 tracking and producing geometry files that all other packages use through the ROOT format described above. This task is made non-trivial by the need for a highly detailed description of the geometry in order to check all possible sources of

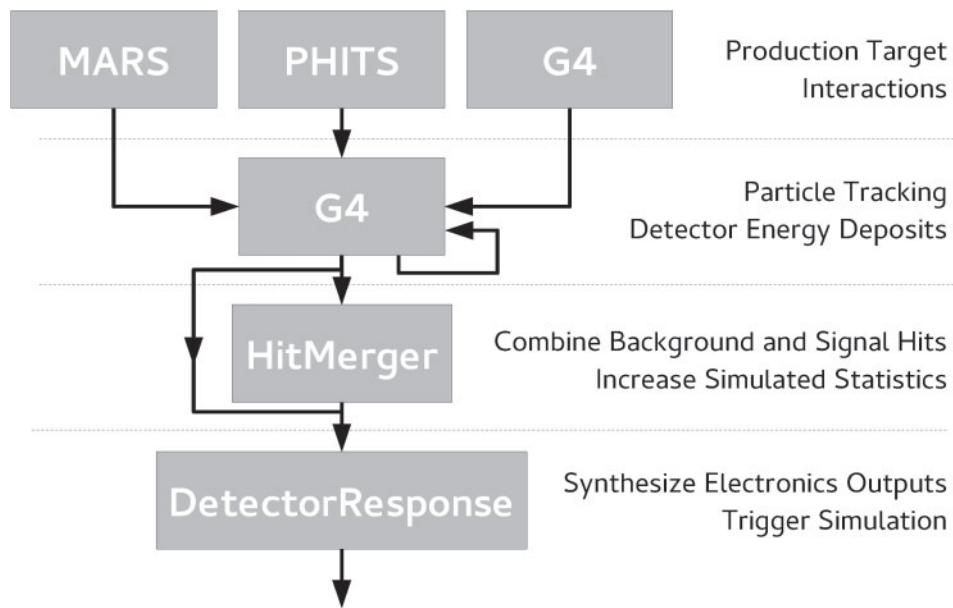


**Fig. 90.** The package structure of the simulation of ICEDUST.

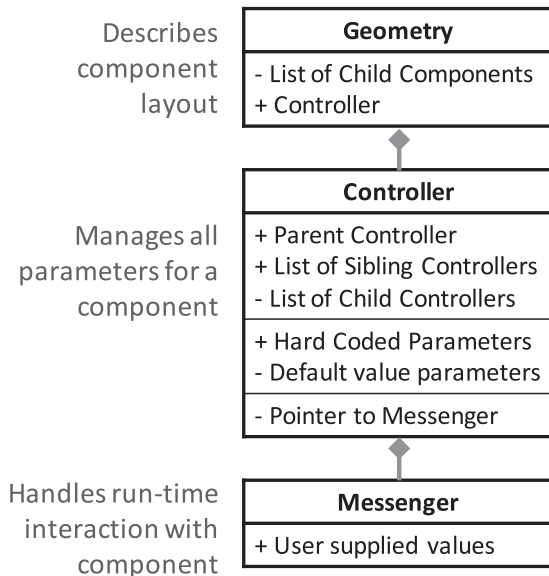


**Fig. 91.** Class structure of the geometry–controller–messenger model.

backgrounds combined with COMET’s staged approach, meaning that the experiment is likely to change quite drastically throughout its lifetime.

In practice, a user writes the geometry in C++ code, then defines all the parameters in a Geant4 macro that is processed by a “messenger” and “controller”, as shown in Fig. 91. These parameters can be defined using complex expressions involving other parameters, which provides a flexible way to build the geometry.

### 9.3.2. Custom Geant4 processes

Custom modeling of physics processes has been developed within the Geant4-based simulation to provide models that match experimental data and models that include the latest theoretical updates. In particular, modeling for negative muons stopping in aluminum has been implemented into ICEDUST. A custom class for physic processes is defined by inheriting the G4HadronicInteraction class, to describe the muon bound or capture process in an aluminum atom. The AlCap data and DIO spectrum estimation [49] are implemented in the class. This implementation of the modeling should be robust to future Geant4 updates, but also allows new spectra to be included easily as they become available.

### 9.3.3. Hadron production models

There is a large variation in the pion and muon yield predicted by different hadron production codes. It is therefore essential that the simulation has the ability to use different hadron production codes. Currently, simulations have been done using FLUKA [92], Geant4, MARS, and PHITS and these codes have all been integrated into the ICEDUST framework. Ensuring the consistency of the geometry requires careful consideration when using FLUKA and PHITS as they do not have native support for the ROOT geometry.

Since these packages contain very detailed, experimentally supported hadron interaction models, they are particularly useful for studying and simulating the pion production target and running shielding calculations.

### 9.3.4. Refining simulation against experimental data

In order to achieve the single-event sensitivity of Phase-I, it will be necessary to fully understand all sources of particles that could mimic an electron produced by muon-to-electron conversion. This requires accurate simulation of the experimental apparatus as well as understanding the production mechanisms of rare processes that produce signal-like electrons and ensuring that these are well modeled in the simulation.

It is important to make use of Phase-I to characterize the beam line and thus understand the transport characteristics of the curved solenoid channel in order to understand the background rates and validate the simulation. This can be done using a relatively simple detector to make flux measurements in the Phase-I beam line and by varying the magnetic fields and placing absorbers in the beam. Preliminary studies to show what sort of measurements can be done with Phase-I are presented in Ref. [94]. These results show that it is possible to alter the composition of the beam, by making simple changes to the magnetic field or using absorbers, and therefore understand the transport properties of the beam line better; this will provide a way to ensure that the simulation accurately models the experiment.

Important information will be provided by other experiments (e.g., AlCap) and beam tests (e.g., calorimeter resolution tests). The information from these will be fed back to improve the physics and detector descriptions in the offline software.

## 9.4. Reconstruction

The aim of the reconstruction software is to take a collection of hits stored in a ROOT file, either from simulation or experimental data, and produce a collection of reconstructed objects such as tracks and clusters. This requires track or cluster finding and fitting code specific to each detector system.

GENFIT [95] is integrated into ICEDUST, which provides:

- integration with SimG4;
- the ability to run on experimental data;
- integration with analysis codes;
- a simple interface to validate geometries and magnetic fields.

One important requirement of the ICEDUST framework is to provide a full audit trail that allows an exact recreation of an analysis plot. This requires persisting the precise process used by the reconstruction to create the reconstruction objects. This will obviously be different depending on which code is used, e.g., for track reconstruction. Thus, the minimal set of information required to fully specify the reconstruction process needs to be defined for each code. This can then be persisted in a database and used to tag the simulated data that are produced.

### 9.5. MC data production and distribution

With each major software release, there will also be the generation of large-scale MC data. This will be needed to debug the offline software as well as improve the experimental details of Phase-I, reconstruction algorithms, and analysis code. In addition to producing data that will mimic the data from Phase-I, specific background modes will be simulated so that very rare processes can be studied in a resource-efficient way. The first of these MC production runs has been done and was used to debug the software and provide estimates of the computing resources required for future MC data production. These data sets will be used to develop reconstruction algorithms and analysis code and will provide estimates of the resources needed to process data from Phase-I, where the data rate is currently estimated to be 7 Tb/day for continuous running.

Grid computing resources will be used to distribute data. A similar production and distribution plan to that of the ND280 experiment will be used.

## 10. Physics sensitivity and background estimation

COMET will operate in CyDet mode to search for  $\mu-e$  conversion in Phase-I. The single-event sensitivity (SES) is determined for a given number of stopped muons, as described below. The different sources of backgrounds are identified in Table 11.

### 10.1. Signal sensitivity

The signal acceptance is determined by the geometrical acceptance of the CyDet, the track quality cuts, and the acceptances of momentum and time windows of measurements.

*Geometrical acceptance* The geometrical acceptance is determined by the dimensions and positions of both the CDC and the CTH systems and the configuration of the magnetic field. Figure 92 shows the longitudinal momenta ( $P_L$ ) distributions for the tracks that enter the CDC (open histogram), and in addition those that make two-fold (blue histogram) and four-fold (magenta histogram) coincidence in the CTH. The tracks are generated isotropically at the muon stopping target. The acceptance of tracks reaching the CTH after a single turn (shown in Fig. 92 (left)) and after multiple turns (shown in Fig. 92 (right)) are 0.21 and 0.13, respectively. If a coincidence of hits in the CTH is required, the acceptance is further reduced. For a four-fold coincidence the acceptance of single-turn tracks and multiple-turn tracks becomes 0.16 and 0.10 respectively, giving an overall value of 0.26.

**Table 11.** A list of potential backgrounds for the search for the  $\mu^-N \rightarrow e^-N$  conversion at the COMET experiment. The items with \* would not produce 100 MeV/c electrons but noise hits in the CyDet.

Intrinsic physics backgrounds		
1	Muon decays in orbit (DIO)	Bound muons decay in a muonic atom
2	Radiative muon capture (external)	$\mu^-A \rightarrow \nu_\mu A'\gamma$ , followed by $\gamma \rightarrow e^-e^+$
3	Radiative muon capture (internal)	$\mu^-A \rightarrow \nu_\mu e^+e^-A'$ ,
4*	Neutron emission after muon capture	$\mu^-A \rightarrow \nu_\mu A'n$ , and neutrons produce $e^-$
5*	Charged particle emission after muon capture	$\mu^-A \rightarrow \nu_\mu A'p$ (or $d$ or $\alpha$ ), followed by charged particles producing $e^-$
Beam-related prompt/delayed backgrounds		
6	Radiative pion capture (external)	$\pi^-A \rightarrow \gamma A'$ , $\gamma \rightarrow e^-e^+$
7	Radiative pion capture (internal)	$\pi^-A \rightarrow e^+e^-A'$
8	Beam electrons	$e^-$ scattering off a muon stopping target
9	Muon decay in flight	$\mu^-$ decays in flight to produce $e^-$
10	Pion decay in flight	$\pi^-$ decays in flight to produce $e^-$
11	Neutron-induced backgrounds	neutrons hit material to produce $e^-$
12	$\bar{p}$ -induced backgrounds	$\bar{p}$ hits material to produce $e^-$
Other backgrounds		
14	Cosmic-ray-induced backgrounds	
15	Room neutron-induced backgrounds	
16	False tracking	

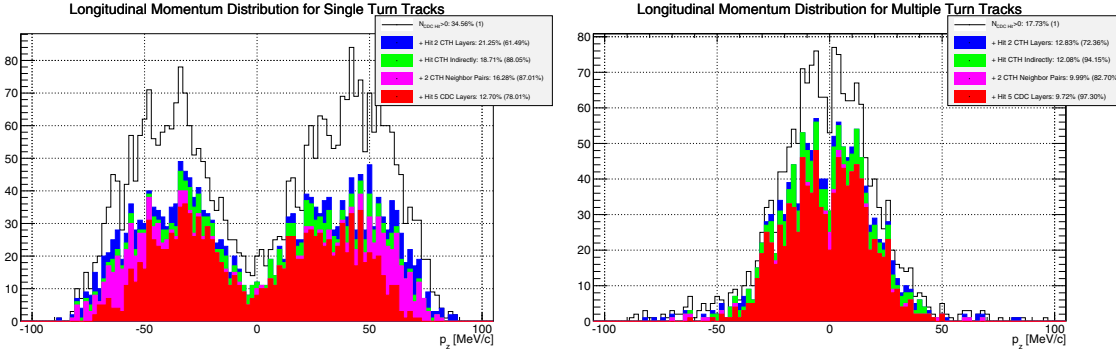


**Fig. 92.** (Left) Distribution of longitudinal momentum ( $P_z$ ) of single-turn tracks. Blue histogram is the tracks with two-fold coincidence of CTH, and magenta histogram is those with four-fold coincidence of CTH. (Right) The same for multiple-turn tracks.

**Track quality cuts** In the tracking, the following requirements are made to ensure that only high-quality tracks are considered:

- tracks must reach the fifth sense layer (NL5),
- at least one whole turn in the CDC is required (NHIT),
- the number of degrees of freedom must be greater than 30 (NDF30),
- the normalized  $\chi^2$  must be less than two ( $\chi^2$ ), and
- hits are required in more than three consecutive layers at both the entrance and exit points of the tracks (CL3).

**Table 12.** Breakdown of the tracking quality cuts, together with the geometrical acceptance, separately for single-turn and multiple-turn tracks. The acceptance is normalized to all the signal tracks generated and emitted isotropically from the muon stopping target.

	single-turn tracks	multiple-turn tracks	single + multiple
Geometrical	0.16	0.10	0.26
NL5	0.78	0.98	
NHIT + NDF30 + $\chi^2$ + CL3	0.91	0.73	
total	0.11	0.072	0.18

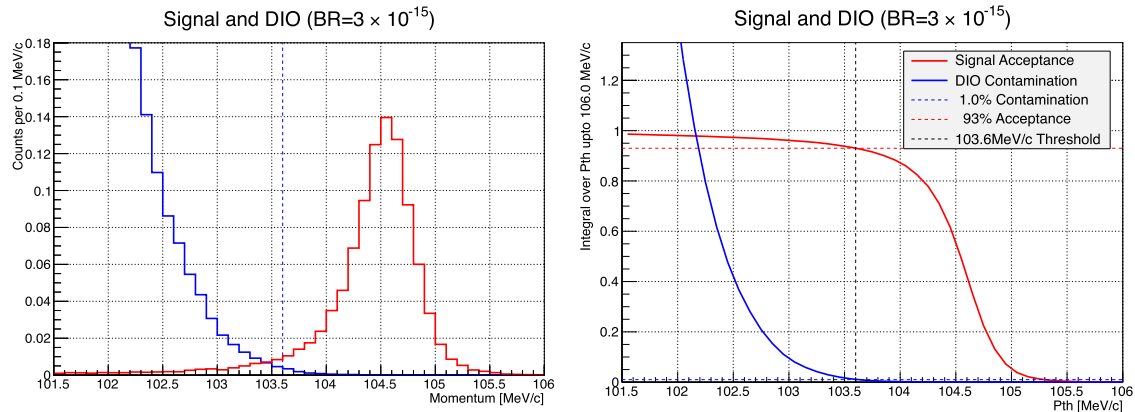


**Fig. 93.** (Left) The momentum distributions for the reconstructed  $\mu-e$  conversion signals and reconstructed DIO events. The vertical scale is normalized such that the integral of the signal curve is equal to one event. This assumes a branching ratio of  $B(\mu N \rightarrow e N) = 3.1 \times 10^{-15}$ . (Right) The integrated fractions of the  $\mu-e$  conversion signals and DIO events as a function of the lower bound of the integration range. The momentum window for signals is selected to be from 103.6 MeV/c to 106 MeV/c, yielding a signal acceptance of 0.93.

Breakdowns of the tracking quality cuts are given separately for single-turn tracks and multiple-turn tracks in Table 12.

**Signal momentum window** A momentum cut is used to reduce contamination from background events such as DIO electrons. Figure 93 shows the simulated momentum spectra for the  $\mu-e$  conversion signal events and DIO electrons. In Fig. 93, the vertical scale is normalized so that the integral of the signal event curve is one event at a branching ratio of  $B(\mu N \rightarrow e N) = 3.1 \times 10^{-15}$ . Using a momentum window of  $103.6 \text{ MeV}/c < P_e < 106.0 \text{ MeV}/c$ , as shown in Fig. 93, results in a signal acceptance of  $\epsilon_{\text{mom}} = 0.93$  being obtained for an SES of  $3.1 \times 10^{-15}$ . An estimate of the contamination from DIO electrons is presented in Sect. 10.2.

**Signal time window** Muons stopped in aluminum have a mean lifetime of 864 ns and so  $\mu-e$  conversion electrons are detected between the proton pulses to avoid the beam-related backgrounds. The time window is currently chosen to start at 700 ns after the prompt timing but will be subsequently optimized.

The acceptance due to the time window cut is shown in Fig. 94 for a varying start time  $T_1$  and a fixed stop time of  $T_2 = 1170$  ns (left) and for a fixed  $T_1 = 700$  ns and a variable  $T_2$  (right). Both assume a pulse separation  $T_{\text{sep}}$  of 1170 ns. Currently, the baseline design is that  $T_1 = 700$  ns

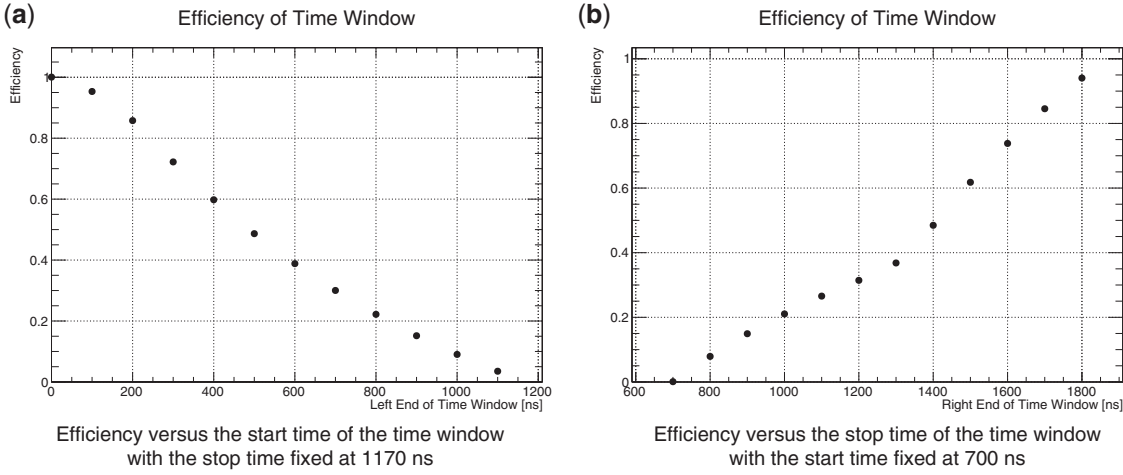


**Fig. 94.** Acceptances of the time window of measurement of the time window as a function of (a) start time and (b) stop time. The width of the proton pulses of 100 ns is included. The periodic time structure is considered with bunch separation time  $T_{\text{sep}} = 1170$  ns.

**Table 13.** Factors contributing to the  $\mu-e$  conversion signal acceptance value.

Event selection	Value	Comments
Online event selection efficiency	0.9	Sect. 8.1.1
DAQ efficiency	0.9	
Track finding efficiency	0.99	Sect. 5.4
Geometrical acceptance + Track quality cuts	0.18	
Momentum window ( $\varepsilon_{\text{mom}}$ )	0.93	103.6 MeV/c < $P_e$ < 106.0 MeV/c
Timing window ( $\varepsilon_{\text{time}}$ )	0.3	700 ns < $t$ < 1170 ns
Total	0.041	

and  $T_2 = 1170$  ns, and  $T_{\text{sep}}$  is 1170 ns. The signal acceptance resulting from the time window is  $\varepsilon_{\text{time}} = 0.30$ .

*Net signal acceptance and single-event sensitivity* The SES is given by:

$$B(\mu^- + \text{Al} \rightarrow e^- + \text{Al}) = \frac{1}{N_\mu \cdot f_{\text{cap}} \cdot f_{\text{gnd}} \cdot A_{\mu-e}}, \quad (21)$$

where  $N_\mu$  is the number of muons stopped in the target. The fraction of captured muons to total muons on target  $f_{\text{cap}} = 0.61$  is taken, while the fraction of  $\mu-e$  conversion to the ground state in the final state of  $f_{\text{gnd}} = 0.9$  is taken [96].  $A_{\mu-e} = 0.041$  is the net signal acceptance. The contributing factors to the overall acceptance are shown in Table 13. To achieve SES of  $3 \times 10^{-15}$ ,  $N_\mu = 1.5 \times 10^{16}$  is needed. By using the muon yield per proton of  $4.7 \times 10^{-4}$ , a total number of protons on target (POT) of  $3.2 \times 10^{19}$  is needed. With a proton beam current of  $0.4 \mu\text{A}$ , the measurement requires about 146 days although there are considerable uncertainties such as the pion production yield.

## 10.2. Intrinsic physics backgrounds

Negative muons stopped in material form a muonic atom and then cascade down to the 1s orbit. From there the fate of the bound  $\mu^-$  is dominated by two (Standard Model) allowed processes, muon decay in orbit (DIO), and nuclear muon capture (NMC).

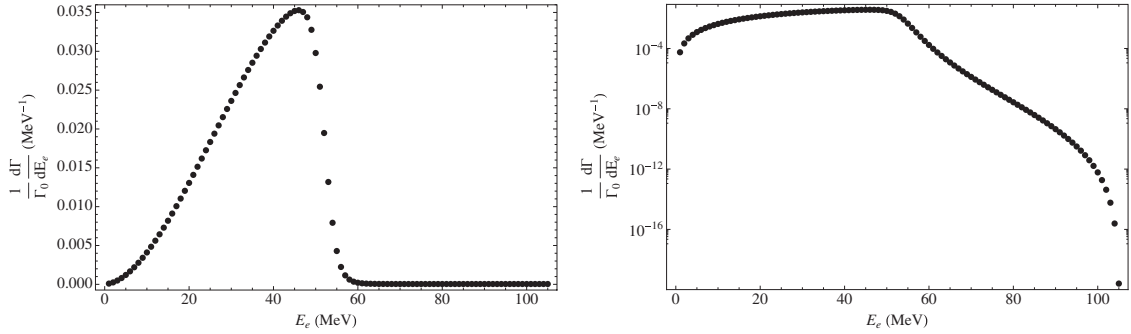


**Fig. 95.** DIO electron spectrum for aluminum. The left has a linear scale and the right a logarithmic scale. From Ref. [49].

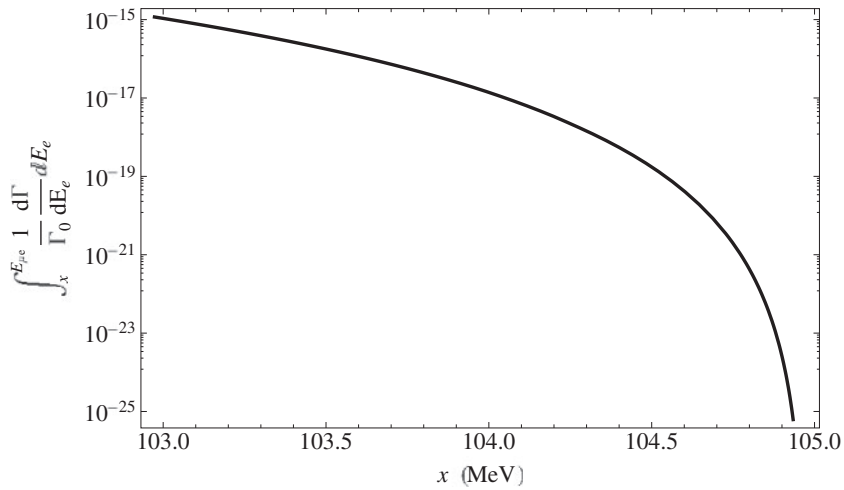


**Fig. 96.** Total rate of DIO for aluminum above the electron energy  $x = E_e$  (MeV) value, normalized by the free muon decay rate from Ref. [49].

**Muon decays in orbit (DIO)** In a free muon decay the electron momentum must be balanced against that of the neutrinos but in DIO the nuclear recoil from the Michel decay allows the electron to carry much more energy. This causes the maximum energy of the  $e^-$  to exceed the endpoint energy of the free Michel decay at rest (52.8 MeV), extending it to the momentum range of the  $\mu-e$  conversion signal. The endpoint energy of DIO occurs when the neutrinos are produced at rest and can be very close to the  $\mu-e$  conversion signal energy  $E_{\mu e}$ .

The momentum spectrum of DIO electrons for aluminum has been calculated based on the model described in Refs. [49–52]. Figure 95 shows the momentum spectrum of DIO electrons from aluminum and Fig. 96 shows the proportion of the aluminum DIO spectrum with energy above  $x$  (MeV) [49]. Hence, to reduce the DIO contribution down to  $\mathcal{O}(10^{-16})$ , the lower side of the momentum region for  $\mu-e$  conversion signals should be above about 103.6 MeV.

In Fig. 97, the reconstructed momentum spectrum of DIO electrons is shown (blue line), normalized to the rate of a single  $\mu-e$  conversion event at a branching fraction of  $3 \times 10^{-15}$ . For a momentum window of  $103.6 \text{ MeV}/c < P_e < 106 \text{ MeV}/c$  for the  $\mu-e$  conversion signals the fraction of DIO electrons in the signal region is 0.01 events for an SES of  $3 \times 10^{-15}$ .

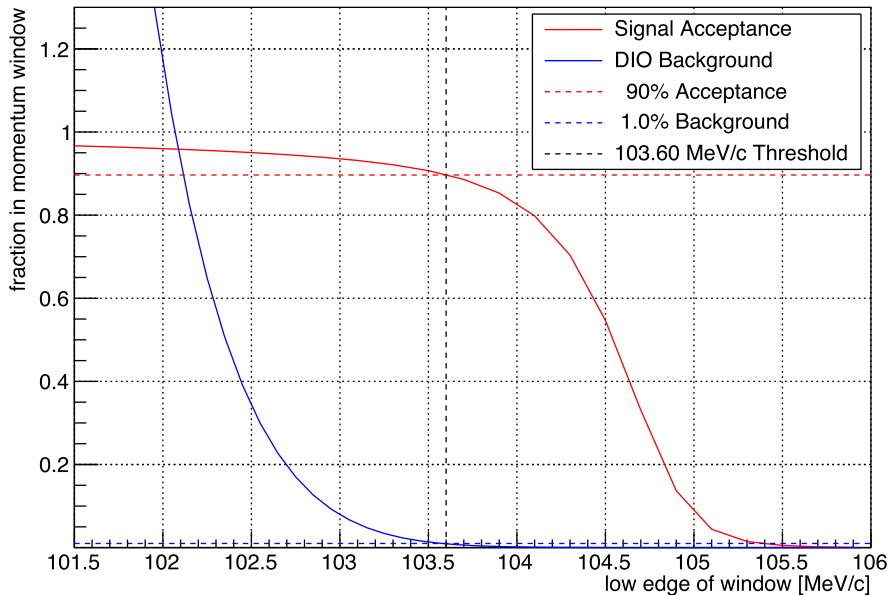


**Fig. 97.** Reconstructed DIO spectrum for aluminum, normalized to one single event of  $\mu-e$  conversion with  $3 \times 10^{-15}$ . The red line shows the integrated event rate above the energy given. The lower edge of the momentum window of the signal is set to be 103.6 MeV.

*Radiative muon capture (RMC)* Radiative muon capture is given by

$$\mu^- + N(A, Z) \rightarrow \nu_\mu + N(A, Z - 1) + \gamma. \quad (22)$$

If the emitted  $\gamma$ -ray is followed by asymmetric  $e^+e^-$  conversion, or Compton scattering of the photon, it forms an important source of intrinsic background. This is referred to as “external” RMC. There is also “internal” conversion of the (virtual) photon:

$$\mu^- + N(A, Z) \rightarrow \nu_\mu + N(A, Z - 1) + e^+ + e^-, \quad (23)$$

which can make a similar contribution to the background when the  $e^+e^-$  are asymmetric. As is the case with DIO, energy measurement is the only means to combat RMC; hence understanding the spectrum shape towards the endpoint is most important.

For the external process, the kinematic endpoint ( $E_{\text{RMC}}^{\text{end}}$ ) of the emitted photon from RMC is given by

$$E_{\text{RMC}}^{\text{end}} \approx m_\mu - B_\mu - \Delta_{Z-1} - E_{\text{recoil}} = E_{\mu e} - \Delta_{Z-1}, \quad (24)$$

where  $m_\mu$  is the muon mass,  $B_\mu$  is the muon binding energy in a muonic atom, and  $E_{\text{recoil}}$  is the recoiling energy of the final nucleus.  $\Delta_{Z-1}$  is the difference in the mass of the initial ( $A, Z$ ) and final ( $A, Z - 1$ ) nucleus involved in RMC. In aluminum the nuclear mass difference  $\Delta_{Z-1} = +3.12$  MeV and the RMC photon endpoint energy is 101.85 MeV.

If the photon from RMC produces an electron by Compton scattering, the maximum momentum of the emitted electron is  $m_e/2 = 0.255$  MeV larger than the original photon momentum. For pair production the maximum momentum of the electron is about  $m_e$  smaller than the original photon momentum. Therefore, Compton scattering is more important than external pair production or RMC with internal conversion.

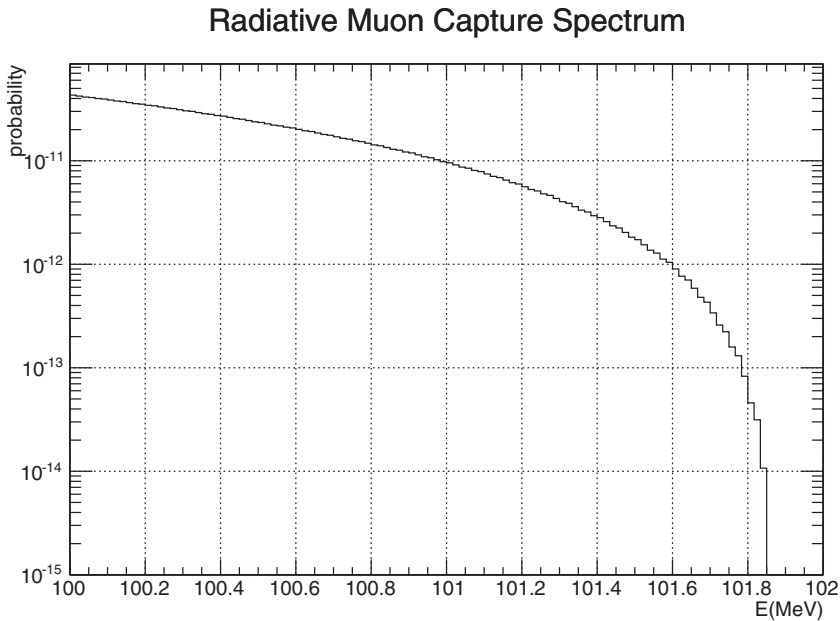


**Fig. 98.** Extrapolated momentum distribution of photons from RMC, based on theoretical prediction [97].

The total background contribution from RMC for a single signal event is given by

$$N_{\text{RMC}} = N_{\text{proton}} \times R_{\mu-\text{stop}/p} \times B_{\text{RMC93}} \\ \times P_{\gamma-e} \times A_{\text{geo}} \times A_{\text{mom}} \times A_{\text{time}} \times \varepsilon_{\text{tracking}}, \quad (25)$$

where  $N_{\text{proton}}$  is the total number of protons on the pion production target;  $R_{\mu-\text{stop}/p}$  is the number of  $\mu^-$  arriving at the muon stopping target per proton;  $B_{\text{RMC93}}$  is the branching ratio of RMC producing a photon with more than 93 MeV;  $P_{\gamma-e}$  is the probability of conversion of the RMC photon to an electron in the signal region;  $A_{\text{geo}}$  is the detector acceptance of the RMC-originated electrons in the signal region;  $A_{\text{mom}}$  and  $A_{\text{time}}$  are the acceptances of momentum cut and timing cut, respectively; and  $\varepsilon_{\text{tracking}}$  is the tracking efficiency.

No experimental data for the photon spectrum from RMC on aluminum near the endpoint are available and so theoretical predictions must be used to extrapolate to the endpoint. Following Hwang [97], the spectrum based on Hwang–Primakoff theory is given by

$$R(x) = C(1 - 2x + 2x^2)x(1 - x)^2, \quad (26)$$

where  $x = k/k_{\text{max}}$ ,  $k$  is the photon energy, and  $C$  is a constant. For the overall normalization,  $C$ , we make use of the measured rates of RMC on aluminum from Ref. [98]. The result of this extrapolation is shown in Fig. 98. From this, the probability per muon capture of producing a photon with energy exceeding 93 MeV is estimated to be  $B_{\text{RMC93}} = 2.97 \times 10^{-7}$ . One aim of COMET Phase-I will be to measure the RMC photon spectrum on aluminum. The prediction of the electron spectrum resulting from RMC is shown in Fig. 99, along with the DIO spectrum. This gives the number of RMC backgrounds,  $N_{\text{RMC}} = 0.0019$ , in the momentum window of the signal

### 10.3. Beam-related prompt backgrounds

The beam-induced prompt backgrounds arise from protons circulating in the MR buckets between the intended beam pulses. They are suppressed by the proton beam extinction factor,  $R_{\text{extinction}}$ , which,

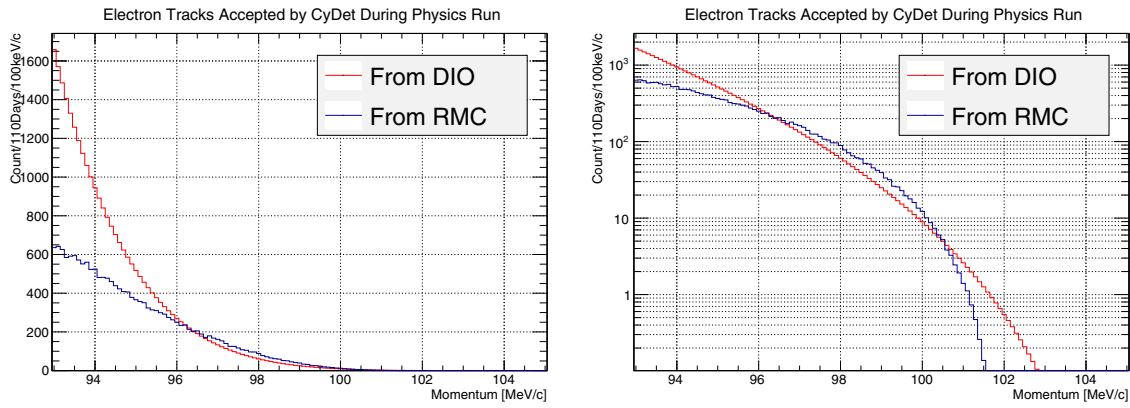


**Fig. 99.** Comparison of the rates and spectra between RMC and DIO, on linear (left) and log (right) scales.

in this background estimation, is assumed to be  $3 \times 10^{-11}$  from recent experimental measurements, as given in Sect. 4.1.1.

*Radiative pion capture (RPC)* Pions contaminating the muon beam can be captured by an aluminum nucleus in the target to form an excited state of the daughter nucleus. As with RMC, there are both external and internal conversion mechanisms that can produce the background electron events.

According to Ref. [99], the probability of  $\gamma$  emission has a very small  $Z$  dependence, being about 2% for C, O, and Ca, with the energy of the  $\gamma$  ranging from 50 MeV to 140 MeV. The overall shapes of the spectra are also very similar and so the experimentally obtained spectrum from Ca was used for the RPC simulation.

The number of RPC backgrounds is expressed as

$$N_{\text{RPC}} = N_{\text{proton}} \times R_{\text{extinction}} \times R_{\pi-\text{stop}/p} \times B_{\text{RPC}} \times P_{\gamma-e} \times A_{\text{geo}} \times A_{\text{mom}} \times A_{\text{time}} \times \varepsilon_{\text{tracking}}, \quad (27)$$

where  $N_{\text{proton}}$  is the total number of protons on the pion production target;  $R_{\text{extinction}}$  is the proton beam extinction factor;  $R_{\pi-\text{stop}/p}$  is the number of  $\pi^-$  arriving at the muon stopping target per proton;  $B_{\text{RPC}}$  is the branching ratio of radiative pion capture;  $P_{\gamma-e}$  is the probability of conversion of the RPC photon to an electron of 105 MeV/c;  $A_{\text{geo}}$  is the detector acceptance of the RPC-originated electrons of 105 MeV/c;  $A_{\text{mom}}$  and  $A_{\text{time}}$  are the acceptances of momentum cut and timing cut, respectively; and  $\varepsilon_{\text{tracking}}$  is the tracking efficiency.

With  $3 \times 10^{19}$  protons on target, a total of  $1.4 \times 10^{-3}$  background events from the external conversion of radiative pion capture is predicted. The contribution from internal conversion is about the same and therefore an expectation of  $2.8 \times 10^{-3}$  RPC events is estimated with a proton beam extinction factor of  $3 \times 10^{-11}$ .

*Beam electrons, electrons from muon and pion decays in flight* Electron contamination of the muon beam can arise from  $\gamma$  conversion following  $\pi^0$  decays and the decays of muons and pions in flight. For the decay electrons to have  $p_{\text{total}} > 102$  MeV/c, the muon momentum ( $p_\mu$ ) must exceed 77 MeV/c and the  $\pi$  momentum must exceed 60 MeV/c.

From simulations, the total number of electrons with momenta greater than 80 MeV/c after the beam collimator is  $R_{e-\text{beam}/p} = 1.7 \times 10^{-5}$  per proton, as the electron also needs the transverse

momentum,  $P_T$ , to be greater than 70 MeV/c to reach the CDC. Out of 40 000 electrons in the simulation none reached the CDC, and therefore an upper limit estimate of the background from beam electrons is less than  $3.8 \times 10^{-3}$ .

*Background induced by beam neutrons* Background events could be induced by high-energy beam neutrons that pass through the muon beam line by continuously reflecting from the inner sides of the beam duct. Simulations predict that the average transit time of the neutrons that arrive at the stopping target is around 300 ns, with far fewer arriving at the signal window start time of 700 ns. Therefore, this background is regarded as a prompt background.

The dominant process to produce a 100 MeV electron is  $\pi^0$  production from energetic neutrons, followed by  $\pi^0$  decay and photon conversion.

The prompt background rate  $N_{\text{neutron}}$  can be estimated by

$$N_{\text{neutron}} = N_{\text{proton}} \times R_{\text{extinction}} \times R_{n/p} \times R_{\pi^0/n} \times R_{e/\pi^0} \quad (28)$$

and the ICEDUST simulation yields  $1 \times 10^{-9}$ , so the neutron background through  $\pi^0$  is expected to be negligible.

#### 10.4. Beam-related delayed backgrounds

The beam-related delayed backgrounds arise from slowly arriving particles in the muon beam line. In general they traverse through the solenoids with a small pitch angle in their helical trajectories (namely a small  $P_L$ ), and thereby arrive late. They have specific time distribution to their arrival and they are suppressed by the use of the delayed time window for measurement.

*Beam-related delayed pion backgrounds* It is critical to avoid delayed pions in the beam, since pion decays can easily produce 100 MeV/c electrons.

Figure 100 (left) shows the distribution of pion arrival times relative to the time of the primary proton, and Fig. 100 (middle) is the distribution when the primary proton time profile is assumed to be a square pulse of 100 ns duration. Figure 100 (right) shows the integrated pion survival rate as a function of the starting time of the signal window. When the starting time is set to 700 ns, a pion survival rate of  $10^{-21}$  pions/proton is achieved, which is lower than the proton extinction rate  $R_{\text{extinction}} = 3 \times 10^{-11}$ . Therefore, the beam-related delayed backgrounds are expected to be below the level of the prompt backgrounds. The best signal time window will be determined after some initial running to measure the time distribution of pion arrival.

*Antiproton-induced delayed backgrounds* Low-energy antiprotons produced in the proton target can pass through the muon beam line and annihilate on materials in the detector region, producing other energetic particles, leading directly or indirectly to 100 MeV/c electrons. These antiprotons have very low kinetic energy and low velocity and are therefore not suppressed by the delayed time window of measurement.

Two ways to suppress the antiproton-induced backgrounds are

- decreasing the proton beam energy;
- adding a thin absorber material in the muon beam line.

The choice of 8 GeV proton energy is specifically to reduce the production rate of antiprotons, with keeping reasonably high rates of pion production. However, the yield of antiprotons in the backward

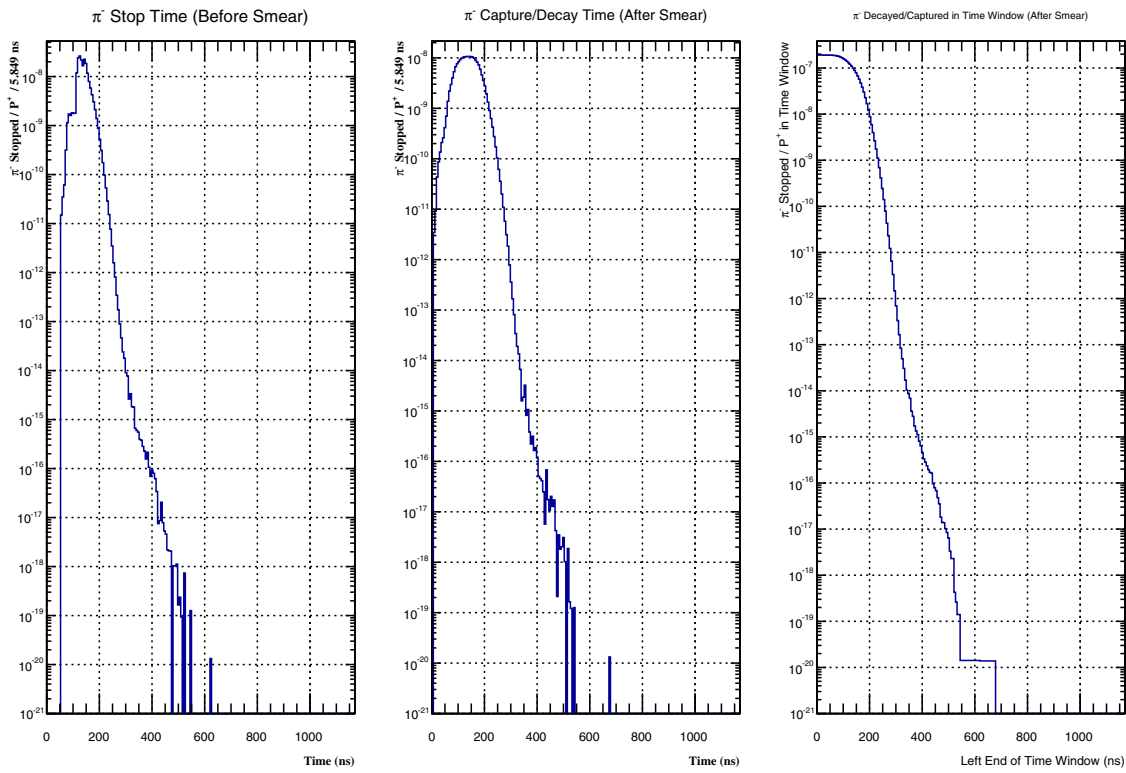


**Fig. 100.** (Left) Pion arrival times when the incoming proton is at time 0. (Middle) Pion arrival times when the incoming proton pulse is assumed to have a 100 ns square time distribution. (Right) Pion survival rate as a function of the starting time of the time window of measurement.

direction from an 8 GeV proton beam is not known, so an estimate has been made from predictions made by the MECO experiment using MARS. This yields a rate of antiproton production per proton of  $4 \times 10^{-5}$ .

Consideration is also being given to installing two absorber foils in the muon beam line. One would be a 500  $\mu\text{m}$  thick titanium foil with a diameter of 360 mm, placed at the entrance of the curved muon-transport solenoid. It would also serve as a vacuum window to separate the muon beam line (in vacuum) and the proton beam line. The thickness of the titanium is sufficient to maintain a pressure difference of one atmosphere. The second absorber foil would be 500  $\mu\text{m}$  thick titanium with a diameter of 255 mm, and placed at the front part of the bridge solenoid (BS). It would also serve as a vacuum window between the muon beam line and the detector region, which contains helium at atmospheric pressure.

From simulations, antiproton background contributions of  $1.2 \times 10^{-3}$  ( $3.5 \times 10^{-3}$ ) are obtained for measurement time windows from 700 (500) ns to 1170 ns.

### 10.5. Cosmic-ray-induced backgrounds

Cosmic-ray-induced backgrounds are one of the most important backgrounds. They can be divided into two categories:

- cosmic-ray muons that produce an electron that enters the detector, and
- cosmic-ray muons that enter the detector and are misidentified as an electron.

To veto and eliminate cosmic-ray-induced backgrounds, the cosmic-ray veto (CRV) system is installed to cover a large portion of the solid angle around the detector solenoid (DS). The CRV detector works as a veto with a very small inefficiency of  $10^{-4}$ , in an environment that has a large flux of neutrons. The COMET Phase-I detector also has good particle identification to discriminate electrons from cosmic-ray muons. Signal tracks are required to hit the CTH, with the Cherenkov counters serving to actively identify electrons.

In order to study cosmic-ray-induced backgrounds, two kinds of simulation studies are being considered. One is a general approach in which cosmic rays are generated widely around the COMET experimental hall. This is useful to examine the overall performance of the CRV and characteristics of cosmic-ray-induced backgrounds. The second is a focused approach, in which some specific combinations of location and direction are chosen and cosmic rays are generated in these areas. In particular, the second method will be used for the locations where the cosmic-ray veto is weak or does not provide complete coverage.

Geant4 simulations are used to estimate cosmic-ray-induced backgrounds. The data set of cosmic rays is based on a CERN input file<sup>12</sup> that contains about 23 million  $\mu^\pm$  events. A full air shower simulation code based on CORSIKA was used. 23 million cosmic-ray events were generated over a  $50 \times 50 \text{ m}^2$  plane. Among this sample, there were no events containing electrons of about 100 MeV in the CDC without being detectable by the CRV. In one event, a cosmic-ray muon produced a shower and one of the shower electrons scattered off the BS, entered the CDC, and hit the CTH. However, the electron lost much of its energy and it would not have been mistaken for a signal electron.

Additionally in the DS area, the CDC also serves as an active volume to detect cosmic-ray muons, complementing the CRV. Overall the net veto inefficiency to identify cosmic rays and/or an associated shower should be much better than  $10^{-4}$ .

Additional simulations in the BS area have found 35 events in which an electron of  $85\text{--}110 \text{ MeV}/c$  reached the CDC from 100 million generated cosmic-ray events. None of them met the CTH trigger requirements and the track quality cuts. Nevertheless, an additional veto system close to the BS is under consideration. With the veto system at BS in place, an upper limit of the cosmic background contribution is obtained to be  $\leq 0.01$  for the COMET Phase-I physics run.

### 10.6. Summary of background estimations

Table 14 shows a summary of the estimated backgrounds. The total estimated background is about 0.032 events for a single-event sensitivity of  $3 \times 10^{-15}$  with a proton extinction factor of  $3 \times 10^{-11}$ . If the proton extinction factor is improved, the expected background events will be further reduced.

## 11. Run programs

The COMET Phase-I experiment is a search for  $\mu\text{--}e$  conversion, but at the same time it is an intermediate stage before the Phase-II experiment. Two special experimental runs will be carried out during the Phase-I experiment, beam measurement and background assessment, which will be dedicated measurements aiming for the preparation of the Phase-II experiment, and for a better understanding of the  $\mu\text{--}e$  conversion data from the Phase-I experiment. Both run programs will use the StrECAL detector with augmented configurations.

---

<sup>12</sup> More recently, CORSIKA simulations of cosmic rays above J-PARC have been obtained from the T2K experiment, but were not available in time for this study.

**Table 14.** Summary of the estimated background events for a single-event sensitivity of  $3 \times 10^{-15}$  in COMET Phase-I with a proton extinction factor of  $3 \times 10^{-11}$ .

Type	Background	Estimated events
Physics	Muon decay in orbit	0.01
	Radiative muon capture	0.0019
	Neutron emission after muon capture	< 0.001
	Charged particle emission after muon capture	< 0.001
Prompt beam	* Beam electrons	
	* Muon decay in flight	
	* Pion decay in flight	
	* Other beam particles	
	All (*) combined	$\leq 0.0038$
Delayed beam	Radiative pion capture	0.0028
	Neutrons	$\sim 10^{-9}$
	Beam electrons	$\sim 0$
Others	Muon decay in flight	$\sim 0$
	Pion decay in flight	$\sim 0$
	Radiative pion capture	$\sim 0$
	Antiproton-induced backgrounds	0.0012
Others	Cosmic rays <sup>†</sup>	< 0.01
Total		0.032

† This estimate is currently limited by computing resources.

### 11.1. Beam measurement programs

There is no measurement on the backward pion production rate with 8 GeV protons. Simulation studies of various hadron production codes such as MARS and Geant4 QGSP (BERT/BIC) estimate a rate that is more than two times different, as described in Sect. 4.3. In order to understand the pion production rate, in the COMET Phase-I experiment, it is planned to measure the muons, pions, antiprotons, and electrons in the beam, with the StrECAL placed downstream of the muon transport.

During the beam measurement, (1) the momentum and profile of the beam, and (2) the beam timing should be measured. For the momentum and profile measurement, track reconstruction and particle identification (PID) are necessary. This also requires a lower hit rate and thus lower beam power. For the beam timing measurement, the goal is to reproduce the timing distribution of particles after the initial beam pulse, which does not require track reconstruction and momentum information. This measurement can be made without the detector solenoid and straw detector; therefore the beam can be operated at full power.

#### 11.1.1. Particle identification by StrECAL

While there is no detector dedicated to PID in COMET, a special StrECAL configuration may be designed to optimize the PID capability, by placing a scintillating fiber (Sci-Fi) detector at the end of the muon beam line. In this configuration,  $\frac{dE}{dx}$  and  $E/p$  can be provided by the ECAL, and the time of particle flight (TOF) between ECAL and the scintillating fiber (Sci-Fi) detector can be used for PID. The pulse shape analysis of the ECAL signal will also be investigated.

A prototype Sci-Fi detector with 1 mm-square scintillating fibers and MPPC readouts was successfully tested to obtain the beam profile during the StrECAL test in KEK. However, a smaller fiber such as 250- $\mu\text{m}$  would be preferred to minimize secondary particle production. Recent measurements

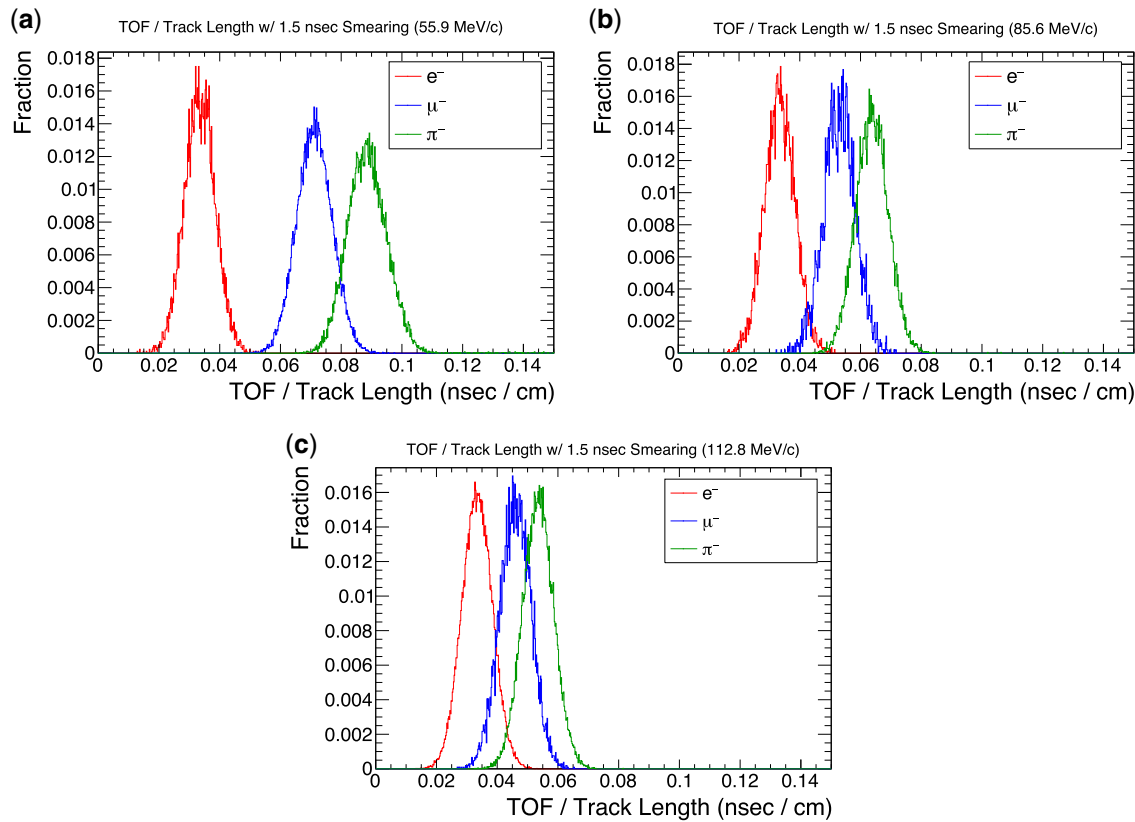


**Fig. 101.** A simulation of TOF performance. The distributions of TOF divided by the track length (therefore, the inverse of velocity) are shown. The vertical scale is arbitrary. Particle momenta of the simulation are (a) 55.9 MeV/c, (b) 85.6 MeV/c, and (c) 112.8 MeV/c. The red, blue, and green lines correspond to  $e^-$ ,  $\mu^-$ , and  $\pi^-$ , respectively.

with 250- $\mu\text{m}$ -square fibers have achieved a satisfactory timing resolution of 500 ps for electrons and 200 ps for muons.

**TOF performance** A dedicated simulation study was performed to evaluate the TOF performance. Figure 101 shows the TOF distributions between the Sci-Fi detector and ECAL of  $e^-$ ,  $\mu^-$ , and  $\pi^-$ , for three different momenta, 55.9, 85.6, and 112.8 MeV/c. A TOF measurement accuracy of 1.5 ns is assumed. It is evident that electrons can be easily distinguished from  $\mu^-$ ,  $\pi^-$  at 55.9 MeV/c, while such discrimination is not complete between  $\mu^-$  and  $\pi^-$ . In the higher-momentum region above 100 MeV/c, even electron discrimination is not possible. Therefore, PID performance is not sufficient with TOF only.

**PID using ECAL signal shape** Another PID method using the different signal shapes of ECAL for different particles is examined. A test on the pulse shape measurements of LYSO crystal was carried out by using intense  $e^\pm/\mu^\pm/\pi^\pm$  beams in PSI. The beam momentum was set to 115 MeV/c, and varied by placing Lucite degraders of varying thickness.

For positive particles ( $e^+$ ,  $\mu^+$ , and  $\pi^+$ ), the decay chain of  $\pi^+ - \mu^+ - e^+$  in the crystal is observed from the waveform measurement, as shown in Fig. 102 (top). This shows that a reasonable PID will be possible by combining the energy deposition information and this decay chain measurement. The decay chain measurement is not possible in the case of negative particles that undergo the nuclear

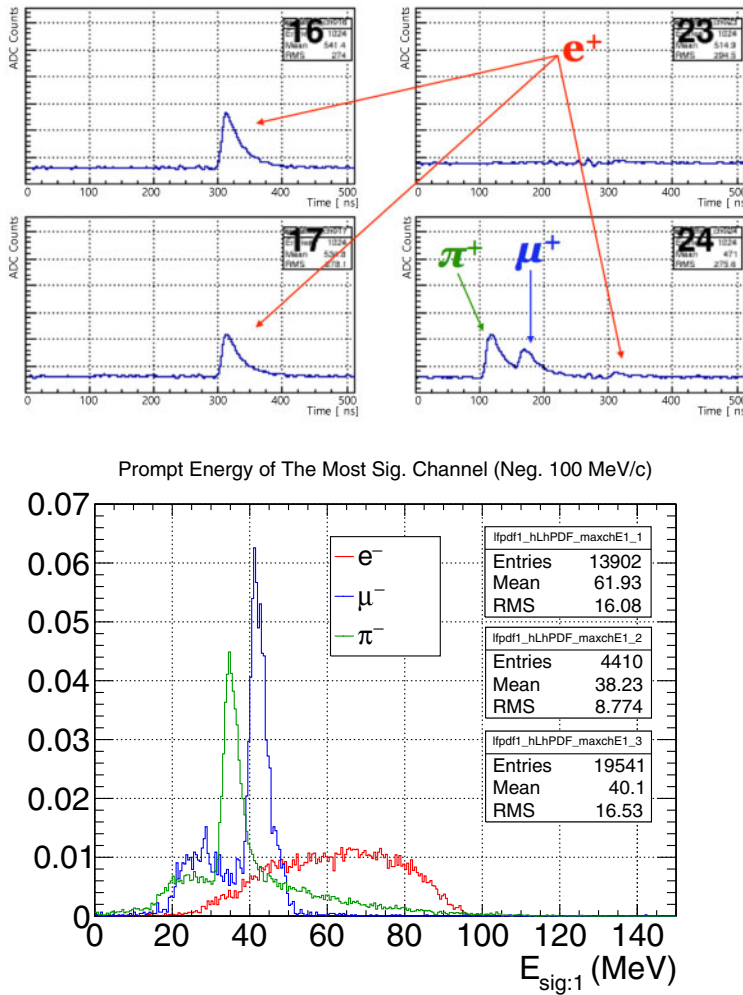


**Fig. 102.** Performance of PID using ECAL signal shape. (Top) Observed decay chain of  $\pi^+ - \mu^+ - e^+$ . (Bottom) Distribution of the prompt energy deposition of negative particles.

capture process. Instead, a weak particle discrimination will be possible by using the fraction of prompt energy deposition to the total energy deposition, which arises from the different nuclear capture processes. Figure 102 (bottom) shows the distribution of prompt energy deposit for three negative particles with  $100 \text{ MeV}/c$ . While a visible difference is observed between  $\mu^-$  and  $\pi^-$ , the difference is not clear since the nuclear capture process is complicated and is not always the same for every event. However, this demonstrates the feasibility of PID using ECAL only.

*PID by combining TOF and ECAL signal shape* In order to improve the PID performance both in low- and high-momentum ranges, a maximum likelihood analysis combining the TOF and ECAL signal shape discriminator has been studied with the simulation data. The results of the PID efficiency estimation are shown in Fig. 103. It is clear that the PID performance can be improved by combining the TOF and ECAL signal shape discriminator. In the case of negative particles, it is clear that a PID efficiency as high as 90% for all momentum ranges can be achieved when the TOF timing resolution is 1.0 ns. The PID efficiency is still above 85% when the TOF timing resolution is 1.5 ns. In the case of positive particles, the PID efficiency is better than negative particles, as the performance of PID by ECAL signal shape is better in positive particle cases. In conclusion, the beam measurement in

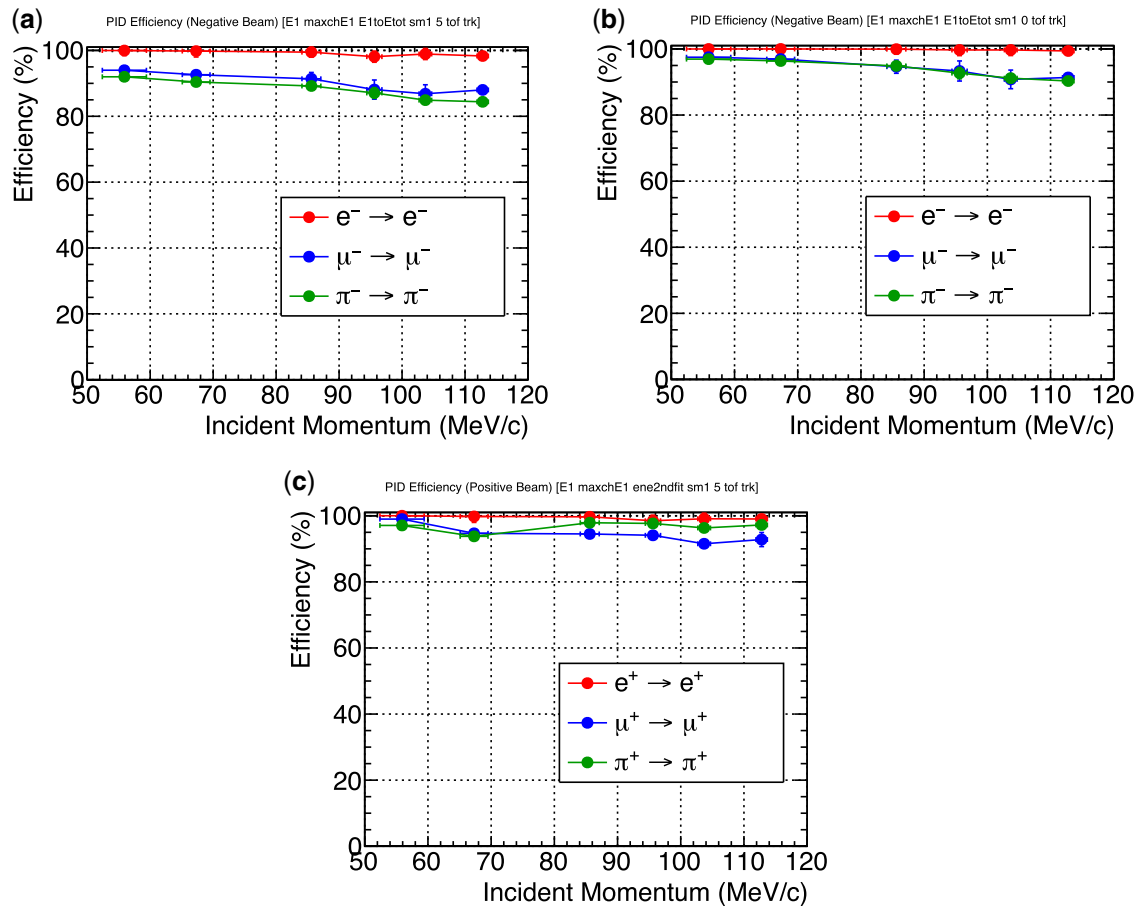


**Fig. 103.** PID efficiencies by combining TOF and ECAL signal shape discriminator. (a) Negative particle cases with expected TOF timing resolution 1.5 ns, (b) negative particle cases with expected TOF timing resolution 1.0 ns, (c) positive particle cases with expected TOF timing resolution 1.5 ns.

the COMET Phase-I experiment will be possible by configuring StrECAL with a TOF detector, and by using a combined analysis of the TOF and ECAL signal shape discriminator.

#### 11.1.2. Rate capability consideration of StrECAL

In the beam measurement program, not only the momentum and profile of the beam, but also the timing structure of the beam will be measured. The rate capability of the StrECAL detector is investigated with ICEDUST in order to understand the feasibility of measuring the timing structure of the beam.

It is clear that the 3.2 kW beam of the COMET Phase-I experiment is too strong for the momentum and profile measurement. One option is to reduce the beam power, which is clearly not ideal. An alternative option is to decrease its sensitivity in the StrECAL central region of the beam. A “beam blocker” and “HV masking” have been investigated.

**Beam blocker** Since the muon-transport line for Phase-I is not long enough and has only 90° bending, the rate of transported beams to the detector section will be very high. As most beam particles are in the central region, a beam blocker in that region of the beam can reduce the rate

**Table 15.** Summary of the beam measurement program.

	Momentum measurement	Timing measurement
Detector	StrECAL + SciFi	ECAL signal shape discriminator
Beam mode	Normal SX	Bunched SX
Detector solenoid	On	Off
Beam suppression	Beam blocker, HV masking	No beam suppression
PID	Full PID	Easy PID
Beam power	1/1000	1/100 (prompt), full power (delayed)

when operating at Phase-I beam power. A 2 cm thick tungsten disk in front of StrECAL is enough to reduce the hit rate to 20%.

*High voltage masking* To reduce the hit rate further without reducing the beam power, a partial turning off of the HV (“HV masking”), which results in a reduction in the sensitivity of the StrECAL detector, can be considered.

In the straw detector configuration, eight channels of the high voltage are controlled at the same time; this is called an HV unit. From the simulation study with ICEDUST, it is found that HV masking (i.e., turning off) of three units (i.e., 24 channels) can reduce the hit rate by around a factor of 100, when the tracking performance degradation is not significant. The hit rate distribution versus momentum did not change with this three-unit HV masking method.

In the case of ECAL, the hit rate does not change by HV masking. The beam blocker reduces the hit rate in the central part of the beam and the straw detector; however, the reduction of hit rate in the ECAL is uniformly distributed over the ECAL. Therefore, a reduction in the beam power may be still required for beam measurements in the COMET Phase-I experiment.

#### 11.1.3. Plan for the beam measurement

In the case of the beam momentum and profile measurement, a beam power reduction by a factor of 1000 is necessary, as the tracking reconstruction is required by StrECAL. This beam power reduction corresponds to  $2 \times 10^9$  protons on target per second, and consequently 10 kHz hit rate in StrECAL. With this hit rate, a measurement of less than an hour will be enough for the beam measurement. When including the positive particle measurements, a few days of data taking will be sufficient for the momentum and profile measurements.

For the beam timing measurement, track reconstruction is not required and hence the detector solenoid and the straw detector can be turned off during this measurement. PID will rely on the ECAL signal shape discriminator only. When the detector solenoid is off, the hit distribution in the ECAL is almost uniformly distributed, and the momentum spectrum above 40 MeV/c is essentially unaffected. Two classes of beam timing measurement will be made, prompt and delayed.

The beam measurement program is summarized in Table 15. The program is estimated to take two to three weeks.

#### 11.2. Background assessment programs

The background processes of  $\mu-e$  conversion in aluminum have not been measured in most cases. The background estimations described in Sect. 10 are based on simulation. The measurement of background sources is one of the most important goals for COMET Phase-I, for understanding

**Table 16.** Examples of potential backgrounds for the search for  $\mu-e$  conversion. The COMET Phase-I experiment will measure most of the background sources that have not been measured in the past with sufficient accuracy.

Intrinsic physics backgrounds	Status	Plan
Muon decays in orbit (DIO)	endpoint not measured	by Phase-I
Radiative muon capture	endpoint not measured	by Phase-I
Neutron emission	not measured	by AlCap
Charged particle emission	measured (AlCap)	by AlCap
Beam-related backgrounds	Status	Plan
Radiative pion capture		
Beam electrons	not measured	by Phase-I
Muon decay in flight	not measured	by Phase-I
Pion decay in flight	not measured	by Phase-I
Neutron-induced backgrounds	not measured	by Phase-I
$\bar{p}$ -induced backgrounds	not known	by Phase-I
Other backgrounds	Status	Plan
Cosmic-ray-induced backgrounds		by cosmic runs
Ambient neutron-induced backgrounds		

the Phase-I data and for preparing the Phase-II experiment. Examples of such measurements are summarized in Table 16.

*Muon decay in orbit* The electron momentum spectrum of muon decay in orbit (DIO) in the high-momentum region near the endpoint has not been measured. In the COMET Phase-I experiment, CyDet will be used to measure the DIO electron spectrum precisely with a momentum resolution of around 200 keV/c.

*Cosmic-ray-induced background* Cosmic rays are potentially a significant source of background. In order to understand the impact of cosmic rays, a dedicated cosmic-ray run will be performed using the CyDet and CTH triggers when there is no primary beam. The duration of this measurement will be similar to or longer than the beam time of the  $\mu-e$  conversion physics run. The cosmic-ray run will be done before the physics run to understand the necessity of additional configuration of the detector and trigger for further suppression of cosmic-ray backgrounds.

*Radiative muon capture* There is no measurement of radiative muon capture (RMC) with the photon energy in the region of the endpoint for aluminum. As the endpoint is only 3.06 MeV lower than the  $\mu-e$  conversion signal, the RMC background measurement requires 1 MeV or better energy resolution. The CyDet with a gold foil photon converter will be able to measure photons of 100 MeV and above with around 200 keV resolution. The partial branching ratio of RMC on  $^{27}_{13}\text{Al}$ , for a photon energy of greater than 100 MeV, is about  $1.6 \times 10^{-9}$ . Assuming a conversion efficiency of about 1.41% with a 100  $\mu\text{m}$  gold foil together with a simulated signal acceptance of 6.7% and an expected muon yield of COMET Phase-I of  $N_\mu = 1.2 \times 10^9/\text{sec}$ , the running time of 10 days would accumulate about 1000 events. The running time to accumulate 1000 events would be about 10 days. A special trigger condition for this measurement must also be devised, which could be produced either from the CDC hits directly or by adding an additional plastic scintillator.

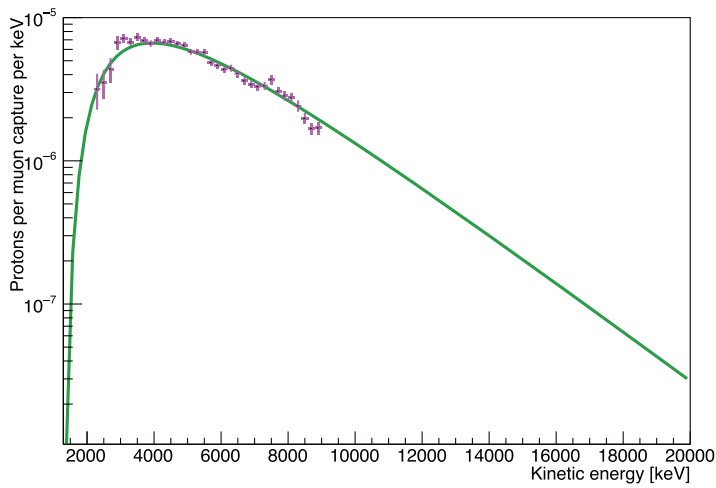


**Fig. 104.** Energy spectrum of protons emitted after nuclear muon capture on aluminum. Data points are from the AlCap measurement in 2013, the solid line shows the fitted function.

*Proton emission after muon capture* The maximum muon beam intensity in the COMET Phase-I experiment will be limited by the hit occupancy of the CDC. Protons, emitted after nuclear muon capture, namely  $\mu^- N \rightarrow N' p \nu_\mu$ , were expected to be one of the major contributors to the CDC hit rate, but measurements from the AlCap experiment have indicated that this is not the case.

The energy spectrum of protons emitted after negative muon capture in an aluminum target has been measured in AlCap. A preliminary analysis shows that the proton emission probability per muon capture in the energy range 4–8 MeV is 0.017. Fitting the measured spectrum and extrapolating the fitted function gives a total emission rate per muon capture of 0.035. The proton spectrum peaks at around 3.7 MeV, then decreases exponentially with a decay constant of 2.5 MeV as shown in Fig. 104. With a Monte Carlo simulation using this distribution the hit rate on a single cell of the CyDet is estimated to be 1.4 kHz, which is low enough for normal operation of the CDC. In the COMET Phase-I experiment, the rate and spectrum of proton emission after muon nuclear capture will be measured with greater statistics than the AlCap results.

## 12. Summary and prospects

Details of the technical design of COMET Phase-I are described. This first stage of the COMET program will provide an opportunity to fully understand the novel superconducting pion production system and muon beam line, with its charge-and-momentum selecting dipole fields that are superimposed on the curved solenoids that form the pion and muon-transport section—a design that is unique to COMET among intense pulsed muon beam facilities.

The research program for Phase-I encompasses both a search for  $\mu-e$  conversion with a sensitivity that is about 100 times better than the current limit, and a dedicated detector setup that will allow us to make comprehensive measurements of the muon beam. Detailed rate and timing studies and other measurements from Phase-I will help us understand the backgrounds to the  $\mu-e$  conversion measurement. These will be crucial as COMET prepares to move to Phase-II, which is to improve the sensitivity by another two orders of magnitude.

The challenges to building and running this high-background rare-decay search experiment are addressed, including: proton and muon beam dynamics; the superconducting magnet systems; high-rate data-acquisition systems; operation in harsh radiation environments; and software and computing systems that can meet the demands of the experiment.

The COMET Collaboration believes that rapid execution of Phase-I, which will consist of data taking in numerous different configurations of the beam line and detector systems, to be followed by the deployment of Phase-II soon after, is the most reliable path to a high-sensitivity search for  $\mu-e$  conversion. The program has the potential to result in a paradigm-shifting discovery, which could lead to a entirely new field opening up of multiple measurements of different charged-lepton flavor-violating processes—a new era of discovery in particle physics.

### Acknowledgements

We thank KEK and J-PARC, Japan for their support of infrastructure and the operation of COMET. This work is supported in part by: the Japan Society for the Promotion of Science (JSPS) KAKENHI Grant Nos. 25000004 and 18H05231; JSPS KAKENHI Grant No. JP17H06135; the Belarusian Republican Foundation for Fundamental Research Grant F18R-006; the National Natural Science Foundation of China (NSFC) under Contract Nos. 11335009 and 11475208; the research program of the Institute of High Energy Physics (IHEP) under Contract No. Y3545111U2; the State Key Laboratory of Particle Detection and Electronics of IHEP, China, under Contract No. H929420BTD; supercomputer funding in Sun Yat-Sen University, China; the National Institute of Nuclear Physics and Particle Physics (IN2P3), France; the Shota Rustaveli National Science Foundation of Georgia (SRNSFG), grant No. DI-18-293; a Deutsche Forschungsgemeinschaft grant STO 876/7-1 of Germany; the Joint Institute for Nuclear Research (JINR), project COMET #1134; the Institute for Basic Science (IBS) of the Republic of Korea under Project No. IBS-R017-D1-2018-a00; the Ministry of Education and Science of the Russian Federation and by the Russian Fund for Basic Research grants: 17-02-01073, 18-52-00004; the Science and Technology Facilities Council, UK; the JSPS London Short Term Predoctoral Fellowship program, a Daiwa Anglo-Japanese Foundation Small Grant; and a Royal Society International Joint Projects Grant. Crucial computing support from all partners is gratefully acknowledged, in particular from CC-IN2P3, France; GridPP, UK; and Yandex Data Factory, Russia, which also contributed expertise on machine learning methods.

### References

- [1] The COMET Collaboration, *An experimental proposal on nuclear and particle physics experiments at the J-PARC 50 GeV proton synchrotron: an experimental search for lepton flavor violating  $\mu^-e^-$  conversion at a sensitivity of  $10^{-16}$  with a slow-extracted bunched proton beam* (2007) (available at: [http://comet.kek.jp/Documents\\_files/Phase-I-Proposal-v1.2.pdf](http://comet.kek.jp/Documents_files/Phase-I-Proposal-v1.2.pdf)).
- [2] The COMET Collaboration, *Conceptual design report for experimental search for lepton flavor violating  $\mu^- \rightarrow e^-$  conversion at a sensitivity of  $10^{-16}$  with a slow-extracted bunched proton beam (COMET)*, KEK Report 2009–10 (submitted to the J-PARC Physics Advisory Committee) (2009) (available at: <https://lib-extopc.kek.jp/preprints/PDF/2009/0924/0924011.pdf>).
- [3] The COMET Collaboration, *Letter of intent for Phase-I of the COMET experiment at J-PARC* (2012) (available at: [http://comet.kek.jp/Documents\\_files/PhaseI-LoI-draft-v1.1.pdf](http://comet.kek.jp/Documents_files/PhaseI-LoI-draft-v1.1.pdf)).
- [4] J. Pasternak, Y. Uchida, A. Kurup, M. Lancaster et al., Accelerator and Particle Physics Research for the Next Generation Muon to Electron Conversion Experiment - the PRISM Task Force, 1st Int. Particle Accelerator Conf. (2010) (available at: <http://accelconf.web.cern.ch/AccelConf/IPAC10/papers/wepe056.pdf>).
- [5] Y. Mori, K. Yoshimura, N. Sasao, Y. Kuno et al., *A letter of intent to the J-PARC 50-GeV proton synchrotron experiment: an experimental search for the  $\mu^- - e^-$  conversion process at an ultimate sensitivity of the order of  $10^{-18}$  with PRISM*, Letters of Intent for Nuclear and Particle Physics Experiments at the J-PARC, No. L25 (2003) (available at: <http://www-ps.kek.jp/jhf-np/LOIlist/LOIlist.html>).
- [6] S. T. Petcov, Sov. J. Nucl. Phys. **25**, 340 (1977); Yad. Fiz. **25**, 1336 (1977) [erratum].
- [7] S. M. Bilenky, S. T. Petcov, and B. Pontecorvo, Phys. Lett. B **67**, 309 (1977).
- [8] W. J. Marciano and A. I. Sanda, Phys. Lett. B **67**, 303 (1977).
- [9] B. W. Lee, S. Pakvasa, R. E. Shrock, and H. Sugawara, Phys. Rev. Lett. **38**, 937 (1977); **38**, 1230 (1977) [erratum].
- [10] T. S. Kosmas and S. G. Kovalenko, Phys. Atom. Nucl. **63**, 1158 (2000) [[arXiv:hep-ph/0002070](https://arxiv.org/abs/hep-ph/0002070)] [[Search INSPIRE](#)].

- [11] W. J. Marciano, T. Mori, and J. M. Roney, Ann. Rev. Nucl. Part. Sci. **58**, 315 (2008).
- [12] A. Czarnecki, AIP Conf. Proc., **415**, 252 (1997) [[arXiv:hep-ph/9710425](https://arxiv.org/abs/hep-ph/9710425)] [Search INSPIRE].
- [13] A. Czarnecki, W. J. Marciano, and K. Melnikov, AIP Conf. Proc., **435**, 409 (1998) [[arXiv:hep-ph/9801218](https://arxiv.org/abs/hep-ph/9801218)] [Search INSPIRE].
- [14] V. Cirigliano, R. Kitano, Y. Okada, and P. Tuzon, Phys. Rev. D **80**, 013002 (2009) [[arXiv:0904.0957](https://arxiv.org/abs/0904.0957) [hep-ph]] [Search INSPIRE].
- [15] A. Crivellin, S. Davidson, G. M. Pruna, and A. Signer, J. High Energy Phys. **1705**, 117 (2017) [[arXiv:1702.03020](https://arxiv.org/abs/1702.03020) [hep-ph]] [Search INSPIRE].
- [16] R. Kitano, M. Koike, and Y. Okada, Phys. Rev. D **66**, 096002 (2002); **76**, 059902 (2007) [erratum] [[arXiv:hep-ph/0203110](https://arxiv.org/abs/hep-ph/0203110)] [Search INSPIRE].
- [17] V. Cirigliano, S. Davidson, and Y. Kuno, Phys. Lett. B **771**, 242 (2017) [[arXiv:1703.02057](https://arxiv.org/abs/1703.02057) [hep-ph]] [Search INSPIRE].
- [18] S. Davidson, Y. Kuno, and A. Saporta, Eur. Phys. J. C **78**, 109 (2018) [[arXiv:1710.06787](https://arxiv.org/abs/1710.06787) [hep-ph]] [Search INSPIRE].
- [19] B. Murakami, Phys. Rev. D **65**, 055003 (2002) [[arXiv:hep-ph/0110095](https://arxiv.org/abs/hep-ph/0110095)] [Search INSPIRE].
- [20] The ATLAS Collaboration, *Search for beyond the Standard Model phenomena in  $e\mu$  final states in  $pp$  collisions at  $\sqrt{s} = 13$  TeV with the ATLAS detector*, ATLAS internal report No. ATLAS-CONF-2015-072 (2015).
- [21] R. Foot, H. Lew, X.-G. He, and G. C. Joshi, Z. Phys. C **44**, 441 (1989).
- [22] E. Ma, Phys. Rev. Lett. **81**, 1171 (1998) [[arXiv:hep-ph/9805219](https://arxiv.org/abs/hep-ph/9805219)] [Search INSPIRE].
- [23] A. Abada, C. Biggio, F. Bonnet, M. B. Gavela, and T. Hambye, Phys. Rev. D **78**, 033007 (2008) [[arXiv:0803.0481](https://arxiv.org/abs/0803.0481) [hep-ph]] [Search INSPIRE].
- [24] The CMS Collaboration, *Search for high-mass resonances and quantum black holes in the  $e\mu$  final state in proton-proton collisions at  $\sqrt{s} = 13$  TeV*, CMS internal report No. CMS-PAS-EXO-16-001 (2016).
- [25] J. Sato and M. Yamanaka, Phys. Rev. D **91**, 055018 (2015) [[arXiv:1409.1697](https://arxiv.org/abs/1409.1697) [hep-ph]] [Search INSPIRE].
- [26] I. Doršner, S. Fajfer, A. Greljo, J. F. Kamenik, and N. Košnik, Phys. Rept. **641**, 1 (2016) [[arXiv:1603.04993](https://arxiv.org/abs/1603.04993) [hep-ph]] [Search INSPIRE].
- [27] J. Hisano and K. Tobe, Phys. Lett. B **510**, 197 (2001) [[arXiv:hep-ph/0102315](https://arxiv.org/abs/hep-ph/0102315)] [Search INSPIRE].
- [28] E. Arganda, M. J. Herrero, and A. M. Teixeira, J. High Energy Phys. **0710**, 104 (2007) [[arXiv:0707.2955](https://arxiv.org/abs/0707.2955) [hep-ph]] [Search INSPIRE].
- [29] A. Abada, M. E. Krauss, W. Porod, F. Staub, A. Vicente, and C. Weiland, J. High Energy Phys. **1411**, 048 (2014) [[arXiv:1408.0138](https://arxiv.org/abs/1408.0138) [hep-ph]] [Search INSPIRE].
- [30] L. S. Littenberg and R. Shrock, Phys. Lett. B **491**, 285 (2000) [[arXiv:hep-ph/0005285](https://arxiv.org/abs/hep-ph/0005285)] [Search INSPIRE].
- [31] A. N. Kamal and J. N. Ng, Phys. Rev. D **20**, 2269 (1979).
- [32] A. Zee, Phys. Lett. B **93**, 389 (1980).
- [33] J. D. Vergados, Phys. Rev. D **23**, 703 (1981).
- [34] J. D. Vergados and M. Ericson, Nucl. Phys. B **195**, 262 (1982).
- [35] G. K. Leontaris and J. D. Vergados, Nucl. Phys. B **224**, 137 (1983).
- [36] T. S. Kosmas, G. K. Leontaris, and J. D. Vergados, Prog. Part. Nucl. Phys. **33**, 397 (1994).
- [37] J. H. Missimer, R. N. Mohapatra, and N. C. Mukhopadhyay, Phys. Rev. D **50**, 2067 (1994).
- [38] K. S. Babu and R. N. Mohapatra, Phys. Rev. Lett. **75**, 2276 (1995).
- [39] P. Domin, S. Kovalenko, A. Faessler, and F. Šimkovic, Phys. Rev. C **70**, 065501 (2004).
- [40] B. Yeo, Y. Kuno, M. Lee, and K. Zuber, Phys. Rev. D **96**, 075027 (2017).
- [41] T. Geib and A. Merle, Phys. Rev. D **95**, 055009 (2017).
- [42] T. Geib, A. Merle, and K. Zuber, Phys. Lett. B **764**, 157 (2017).
- [43] J. M. Berryman, A. de Gouvêa, K. J. Kelly, and A. Kobach, Phys. Rev. D **95**, 115010 (2017).
- [44] M. Koike, Y. Kuno, J. Sato, and M. Yamanaka, Phys. Rev. Lett. **105**, 121601 (2010) [[arXiv:1003.1578](https://arxiv.org/abs/1003.1578) [hep-ph]] [Search INSPIRE].
- [45] A. Abada, V. De Romeri, and A. M. Teixeira, J. High Energy Phys. **1602**, 083 (2016) [[arXiv:1510.06657](https://arxiv.org/abs/1510.06657) [hep-ph]] [Search INSPIRE].
- [46] W. Bertl et al., Eur. Phys. J. C **47**, 337 (2006).
- [47] B. Krikler, Sensitivity and background estimates for Phase-II of the COMET experiment, *Ph.D. Thesis*, Imperial College London (2016).
- [48] D. Tomono et al., Proc. 2017 Int. Workshop on Neutrinos from Accelerators (NuFact17), p. 111 (2018).

- [49] A. Czarnecki, X. G. i Tormo, and W. J. Marciano, Phys. Rev. D **84**, 013006 (2011).
- [50] A. Czarnecki, M. Dowling, X. G. i Tormo, W. J. Marciano, and R. Szafron, Phys. Rev. D **90**, 093002 (2014) [[arXiv:1406.3575](https://arxiv.org/abs/1406.3575) [hep-ph]] [Search INSPIRE].
- [51] R. Szafron and A. Czarnecki, Phys. Rev. D **92**, 053004 (2015) [[arXiv:1506.00975](https://arxiv.org/abs/1506.00975) [hep-ph]] [Search INSPIRE].
- [52] R. Szafron and A. Czarnecki, Phys. Lett. B **753**, 61 (2016) [[arXiv:1505.05237](https://arxiv.org/abs/1505.05237) [hep-ph]] [Search INSPIRE].
- [53] T. Sato et al., J. Nucl. Sci. Technol. **50**, 913 (2013).
- [54] M. Cerv et al., JINST **10**, C06016 (2015).
- [55] S. Agostinelli et al., Nucl. Instrum. Meth. A **506**, 250 (2003).
- [56] N. V. Mokhov and S. I. Striganov, AIP Conf. Proc. **896**, 50 (2007).
- [57] H. Sakamoto, Simulation Studies for the CDC for COMET Phase-I, COMET internal note No. 34 (2013).
- [58] Y. Shimbara et al., J. Phys. Soc. Jpn. **84**, 034301 (2015).
- [59] M. Adinolfi et al., Nucl. Instrum. Meth. A **488**, 51 (2002).
- [60] T. Uchida, M. Ikeno, Y. Iwasaki, M. Saito, S. Shimazaki, M. Tanaka, N. Taniguchi, and S. Uno, 2011 IEEE Nuclear Science Symp. Conf. Record, p. 694 (2011).
- [61] S. Shimazaki, T. Taniguchi, T. Uchida, M. Ikeno, N. Taniguchi, and M. M. Tanaka, Nucl. Instrum. Meth. A **735**, 193 (2014).
- [62] Y. Nakazawa, Y. Fujii, E. Hamada, M. Lee, Y. Miyazaki, A. Sato, K. Ueno, H. Yoshida, and J. Zhang, Nucl. Instrum. Meth. A **936**, 351 (2019).
- [63] R. P. Litchfield, PoS **NUFACT2014**, 095 (2015) [[arXiv:1501.04880](https://arxiv.org/abs/1501.04880) [physics.ins-det]] [Search INSPIRE].
- [64] M. Moritsu et al., Proc. 39th Int. Conf. High Energy Physics (ICHEP2018), Vol. 340, p. 538 (2019).
- [65] ELGEN Technology, *EJ-228 and EJ-230 plastic scintillators*, Technical report, Eljen Technology, Sweetwater, TX, USA (2016).
- [66] Hamamatsu Photonics K.K., *H8409-70 photomultiplier tube assembly*, Technical report, Hamamatsu Photonics K.K., Hamamatsu, Shizuoka, Japan (2019) (available at: <http://www.hamamatsu.com/us/en/product/alpha/P/3002/H8409-70/index.html>, date last accessed December 24, 2019).
- [67] E. Gillies, Track Finding with the CyDet at COMET Experiment Using Boosted Decision Trees, Presentation at 4th International Workshop Connecting The Dots 2018 (CTD2018), Seattle, Washington, USA (2018).
- [68] E. Gillies, COMET Phase-I track reconstruction using machine learning and computer vision, *Ph.D. Thesis*, Imperial College London (2019).
- [69] F. Pedregosa et al., J. Mach. Learn. Res. **12**, 2825 (2011).
- [70] S. Movchan, Nucl. Instrum. Meth. A **604**, 307 (2009).
- [71] G. Xu and Ed. V. Hungerford, IEEE Trans. Nucl. Sci. **53**, 549 (2006).
- [72] I. B. Smirnov, Nucl. Instrum. Meth. A **554**, 474 (2005).
- [73] S. F. Biagi, Nucl. Instrum. Meth. A **421**, 234 (1999).
- [74] R. Veenhof, *Garfield, a drift chamber simulation program*, International Conference on Programming and Mathematical Methods for Solving Physical Problems, 14–19 June 1993. Dubna, Russia.
- [75] H. Schindler and R. Veenhof, *Garfield++: simulation of tracking detector*, Technical report, CERN, Geneva, Switzerland (2018).
- [76] S. Ritt, Nucl. Instrum. Meth. A **518**, 470 (2004).
- [77] E. Sakai, IEEE Trans. Nucl. Sci. **34**, 418 (1987).
- [78] H. Ishibashi, K. Kurashige, Y. Kurata, K. Susa, M. Kobayashi, M. Tanaka, K. Hara, and M. Ishii, IEEE Trans. Nucl. Sci. **45**, 518 (1998).
- [79] S. Nakayama et al., Nucl. Instrum. Meth. A **404**, 34 (1998).
- [80] M. Tanaka, K. Hara, S. Kim, K. Kondo, H. Takano, M. Kobayashi, H. Ishibashi, K. Kurashige, K. Susa, and M. Ishii, Nucl. Instrum. Meth. A **404**, 283 (1998).
- [81] Saint-Gobain Crystals, *Crystal scintillation Material*, Technical report, Saint-Gobain Crystals, France (2019) (available at: <https://www.crystals.saint-gobain.com/products/crystal-scintillation-materials>, date last accessed December 24, 2019).
- [82] A. A. Annenkov, M. V. Korzhik, and P. Lecoq, Nucl. Instrum. Meth. A **490**, 30 (2002).

- [83] Hamamatsu Photonics K.K., *S8664-1010 short wavelength type APD*, Technical report, Hamamatsu Photonics K.K., Hamamatsu, Shizuoka, Japan (2019) (available at: <https://www.hamamatsu.com/jp/en/product/type/S8664-1010/index.html>, date last accessed December 24, 2019).
- [84] M. Angelone, M. Pillon, R. Faccini, D. Pinci, W. Baldini, R. Calabrese, G. Cibinetto, A. Cotta Ramusino, R. Malaguti, and M. Pozzati, Nucl. Instrum. Meth. A **623**, 921 (2010).
- [85] G. Baulieu et al., J. Instrum. **10**, P10039 (2015).
- [86] F. Ambrosino et al., J. Geophysical Res. Solid Earth **120**, 7290 (2015).
- [87] J. Adam et al., *Technical design report for the muon forward tracker*, Technical Report CERN-LHCC-2015-001. ALICE-TDR-018, ALICE collaboration, Geneva, Switzerland (2015).
- [88] M. Pesaresi, M. Barros Marin, G. Hall, M. Hansen, G. Iles, A. Rose, F. Vasey, and P. Vichoudis, J. Instrum. **10**, C03036 (2015).
- [89] S. Ritt and P. A. Amaudruz, 1999 IEEE Conf. Real-Time Computer Applications in Nuclear Particle and Plasma Physics, p. 116 (1999).
- [90] K. Abe et al., Nucl. Instrum. Meth. A **659**, 106 (2011) [[arXiv:1106.1238](https://arxiv.org/abs/1106.1238) [physics.ins-det]] [Search INSPIRE].
- [91] K. Niita, T. Sato, H. Iwase, H. Nose, H. Nakashima, and L. Sihver, Radiat. Meas. **41**, 1080 (2006).
- [92] G. Battistoni, F. Cerutti, A. Fassò, A. Ferrari, S. Muraro, J. Ranft, S. Roesler, and P. R. Sala, AIP Conf. Proc. **896**, 31 (2007).
- [93] A. Ferrari, P. R. Sala, A. Fassò, and J. Ranft, CERN-2005-010, SLAC-R-773, INFN-TC-05-11 (2005).
- [94] A. Kurup, I. Puri, Y. Uchida, Y. Yap, R. Appleby, S. Tygier, R. D'Arcy, A. Edmonds, M. Lancaster, and M. Wing, Proc. 4th Int. Particle Accelerator Conference (IPAC 2013), p. 2684 (2013).
- [95] C. Höppner, S. Neubert, B. Ketzer, and S. Paul, Nucl. Instrum. Meth. A **620**, 518 (2010) [[arXiv:0911.1008](https://arxiv.org/abs/0911.1008) [hep-ex]] [Search INSPIRE].
- [96] E. Oset, H. C. Chiang, T. S. Kosmas, A. Faessler, and J. D. Vergados, 13th Int. Conf. Particles and Nuclei (PANIC 93), p. 271 (1993).
- [97] W.-Y. P. Hwang, Phys. Rev. C **22**, 233 (1980).
- [98] D. F. Measday, Phys. Rept. **354**, 243 (2001).
- [99] J. E. Amaro, A. M. Lallena, and J. Nieves, Nucl. Phys. A **623**, 529 (1997).